THE DEVELOPMENT OF AN ACOUSTIC LEVITATION TEST FACILITY FOR CLOUD PHYSICS RESEARCH

by

Victor D. Lupi

S.B., Massachusetts Institute of Technology (1988)

SUBMITTED TO THE DEPARTMENT OF AERONAUTICS AND ASTRONAUTICS IN PARTIAL FULFILLMENT OF THE REQUIREMENTS FOR THE DEGREE OF

MASTER OF SCIENCE IN AERONAUTICS AND ASTRONAUTICS

at the

MASSACHUSETTS INSTITUTE OF TECHNOLOGY

(December 1989)

Signature of Author _____
Department of Aeronautics and Astronautics
December 22, 1989

Certified by _____
Associate Professor R. John Hansman
Thesis Supervisor, Department of Aeronautics and Astronautics

Accepted by _____
Professor Harold Y. Wachman
Chairman, Department Graduate Committee

THE DEVELOPMENT OF AN ACOUSTIC LEVITATION TEST FACILITY FOR CLOUD PHYSICS RESEARCH

by

Victor D. Lupi

Submitted to the Department of Aeronautics and Astronautics on
December 22, 1989 in partial fulfillment of the requirements for the degree of
Master of Science in Aeronautics and Astronautics.

Abstract

An Acoustic Levitation Test Facility appropriate to cloud physics laboratory experiments has been developed. The facility utilizes acoustic standing waves to accurately control the location of single or multiple hydrometeors (water droplets or ice crystals) without direct physical contact. This unique capability allows the facilities to complement existing experimental methods, such as free fall chambers and vertical wind tunnels, where the transient nature of the testing makes carefully controlled experiments difficult. In addition, the small size of the acoustic levitator allows easy access of diagnostics to the test region.

Two separate levitation facilities have been built. In the Vertical Facility, a vertically oriented acoustic levitator utilizes a strong acoustic field to support objects against the force of gravity. The surrounding medium in which the suspended object is held is essentially motionless. In the Ventilated Facility, a small vertical wind tunnel provides the levitating force on the suspended object. This force, arising from aerodynamic drag on the object, opposes the gravitational force on it. In this facility, a horizontally oriented acoustic field is used to stabilize the suspended object within the flow field of the wind tunnel. The motion of the surrounding medium is approximately that of the terminal velocity of the suspended sample.

The theory of acoustic levitation is presented in detail. Predictions are made concerning the performance of the levitation device for solid and liquid samples. For solid spheres, the levitating force diminishes as the diameter approaches the acoustic wavelength. For liquid samples, the deformation of the droplet under the acoustic forces is considered. The predictions are compared with experimental results to validate the theory. Solid samples as large as 9 mm in diameter and liquid samples as large as 4 mm in diameter were levitated in the Vertical Facility.

The effects of the acoustic field on molecular diffusion phenomena was addressed. The evaporation rates of droplets suspended in the acoustic field were compared with the evaporation rates of droplets suspended from a fine glass thread. It was determined that the acoustic field does not significantly affect water vapor diffusion.

The ability to study phase change phenomena in both facilities was demonstrated. Droplets were frozen while levitated in the Vertical Facility. The frozen droplet remained stable in the acoustic field. In the Ventilated Facility, the freezing of droplets in free fall was simulated. The frozen droplets remained stable in the test section until shape asymmetry effects, caused primarily by nonuniform ice accretion, became significant.

Thesis Supervisor: Professor R. John Hansman
Title: Associate Professor of Aeronautics and Astronautics

Acknowledgements

First and foremost, I would like to thank Prof. R.J. Hansman for his seemingly limitless patience and perseverance, and for his advice and inspiration during the many times it was needed. I would also like to thank Paul Bauer and Al Shaw for their technical expertise and willingness to help tackle the practical issues associated with this thesis. In addition, I would like to express my appreciation to my parents, Nino and Lydia, who have continually supported my efforts. Thanks, also, to Debi Jones, for her knowledge of word processing systems and attention to detail. Finally, thanks to the students and dreamers of the Aeronautical Systems Lab that I have come to know over the past two years. This work was supported by the National Science Foundation.

Table of Contents

Nomenclature

a	radius of a spherical object (m)
a	radius of transmitting plate (m)
A	amplitude of velocity potential of acoustic field (m^2/sec)
A_n, A_n'	arbitrary constants associated with solution of wave equation (m^2/sec)
c	speed of wave propagation in an acoustic medium (m/sec)
c_n	coefficients of the harmonic expansion of the deformed droplet shape (-)
d	separation distance between driver and reflector (m)
d_1, d_2	shape parameters of resonating structure (m)
D_v	diffusivity of air (m^2/sec)
$\underline{E}$	modulus of elasticity of resonating structure (Nt/m^2)
$\underline{E}$	time-averaged acoustic energy density (J/m^3)
$\underline{E}_{min}$	minimum acoustic energy density required for levitation (J/m^3)
E	normalized acoustic energy density (-)
f	operating frequency of the acoustic levitator (Hz)
f_n	spherical wave function (-)
F_n, G_n	arbitrary constants associated with solution of wave equation (-)
g	acceleration due to gravity (m/sec^2)
h	distance from nodal plane to center of spherical object (m)
h	thickness of transmitting plate (m)
i	index
j	$\sqrt{-1}$ (-)
j	index (-)
J	curvature of droplet expressed in terms of deformation harmonics (-)
k	acoustic wave number (m^{-1})
k	index (-)
L	length of resonating structure (m)
m	index (-)
n	number of nodal planes in acoustic standing wave (-)
n	index (-)
N_{BO}	Bond number (-)
N_{AC}	nondimensional acoustic parameter (-)
p	pressure in an acoustic medium (Nt/m^2)
p_0	ambient atmospheric pressure in the absence of an acoustic field (Nt/m^2)
$\underline{p_i}$	internal pressure within a water droplet (Nt/m^2)
$\underline{P}$	time-averaged acoustic force on an object in acoustic field (Nt)
P_n	Legendre polynomial (-)
q	magnitude of the velocity in an acoustic medium (m/sec)
q_n	coefficients of harmonic expansion of pressure distribution around droplet (-)
r_0	radius at top of deformed droplet (m)
R	gas constant for air (J/kg-K)
R_1,R_2	principal radii of curvature of deformed droplet (m)
R_n, S_n	arbitrary constants associated with solution of wave equation (-)
s_∞	ambient saturation ratio (-)
S_n	spherical surface harmonic (-)
t	time (sec)
T	nondimensionalized acoustic force on an object (-)
T	ambient temperature (K)
u	longitudinal displacement associated with axial vibrations of a rod (m)
U	nondimensionalized pressure distribution over an object (-)
v_r, v_ϕ, v_θ	components of velocity in spherical coordinates (m/sec)

V	volume of a droplet (m^3)
V_1, V_2	displacement amplitudes at either end of resonating structure (m)
x	dummy variable
z	vertical coordinate of center of a droplet in a planar acoustic standing wave (m)
z_{eq}	equilibrium location of droplet in acoustic field (m)
α	nondimensionalized radius of a sphere (-)
γ	specific heat ratio for air (-)
δp	pressure deviation from ambient due to acoustic field (Nt/m^2)
δz	displacement of an object within acoustic field (m)
ζ	perturbation of an object from equilibrium within an acoustic standing wave (m)
λ	acoustic wavelength (m)
λ_{ij}	modal eigenvalue of axisymmetric vibration of transmitting plate (-)
μ	spherical coordinate (-)
ν	Poisson's ratio of transmitting plate (-)
ρ	density of resonating structure (kg/m^3)
ρ	density of transmitting plate (kg/m^3)
ρ_0	density of air (kg/m^3)
ρ_1	density of object suspended in acoustic field (kg/m^3)
$\rho_{sat,\infty}$	ambient saturation vapor density (kg/m^3)
$\rho_{sat,a}$	saturation vapor density at surface of droplet (kg/m^3)
σ	surface tension of a droplet (J/m^2)
ϕ_n	spherical wave function (-)
Φ	velocity potential of acoustic field (m^2/sec)
Φ_i	velocity potential of incident wave (m^2/sec)
ψ_n	spherical wave function (-)
ω	operating frequency of driver (rad/sec)
ω_1	fundamental modal frequency of shape oscillation of a droplet (rad/sec)
ω_{osc}	frequency of oscillation in position of droplet in acoustic field (rad/sec)
ω_n	modal frequencies of axial vibration of resonator (rad/sec)
ω_{ij}	modal frequencies of axisymmetric vibration of transmitting plate (rad/sec)
$\hat{r}, \hat{\phi}, \hat{\theta}$	unit vectors in spherical coordinates (-)
$\mathbf{v}$	local velocity vector of acoustic medium (m/sec)

Chapter 1
Introduction

1.1 Background

The study of cloud physics is essential to many areas of research. In the field of meteorology, hydrometeor microphysics and droplet dynamics play an important role. The formation of clouds, the initiation of precipitation, the formation of ice, and the electrification of the atmosphere are all based on microphysical phenomena. Aviation technology is also driven by an understanding of these phenomena. For example, understanding and preventing the formation on ice on aerodynamic surfaces requires knowledge of the physical conditions that initiate the icing process. Clearly, the ability to simulate various conditions in the laboratory would serve to advance this technology. The study of the interaction of radar signals with the atmosphere is also a rich topic. In particular, much interest lies in the change in radar attenuation and scattering by the atmosphere when the ambient water vapor undergoes a phase change. Many other topics that rely on knowledge of cloud microphysics exist. Studying these phenomena in the laboratory is difficult, however, as many of these processes occur over long time intervals and have appreciable effects only over large volumes of the atmosphere. For example, free fall chambers are limited by their vertical dimension. The observation time is fixed by the time it takes for the test sample to fall through the test section, making it impossible to study long term effects on hydrometeors. Vertical wind tunnels attempt to solve this problem, with limited success. This is primarily due to the lack of in-stream and lateral stability of the suspended sample in the test section. The lack of these forces cause the samples to either hit the walls of the test section or be carried downstream by the flow. It is therefore desirable to augment the existing set of laboratory apparatus with a facility better capable of maintaining the stability of the hydrometeor while accurately simulating the ambient environment.

To this end, a set of acoustic levitation test facilities appropriate to cloud physics laboratory experiments have been developed. The facilities utilize acoustic standing waves to accurately control the location of single or multiple hydrometeors (water droplets or ice crystals) without direct physical contact. This unique capability allows the facilities to complement the existing experimental methods mentioned above, where the transient nature of the testing makes carefully controlled experiments difficult. In addition, the small size of the acoustic levitator allows easy access of diagnostics to the test region.

1.2 Unique Features of the Acoustic Levitation Test Facility

The concept of levitating small particles by acoustic radiation pressure was proposed as early as 1934 by King [1]. However, it was not until the 1970's that acoustic drivers were sufficiently powerful to allow practical application of acoustic levitators. Currently, levitators are primarily used for containerless materials processing and space shuttle experiments [2][3]. In a typical levitator, shown schematically in Fig. 1-1, an acoustic standing wave is generated between a transmitter and a reflector separated by an integral number of half wavelengths. The particle is supported against gravity by the pressure forces and tends towards a stable equilibrium position in the vicinity of the acoustic nodal planes. A curved reflector surface focuses the acoustic field, creating secondary pressure forces which position the particle to a point within the nodal plane that lies along the axis of the device. Thus, both vertical and horizontal stability is achieved with a single device.

Acoustic levitation holds several unique advantages over conventional experimental techniques (e.g., vertical wind tunnels, free fall testing, mechanical suspension or *in situ* measurement). There are, however, limitations of the acoustic technique as a cloud physics research tool, which are discussed in detail in Chapter 2.

The principal advantage of the acoustic levitation technique is the ability to support particles in a precise manner for indefinite periods of time. The stability in position control for a typical vertical levitator is on the order of one droplet diameter or less. This is in marked

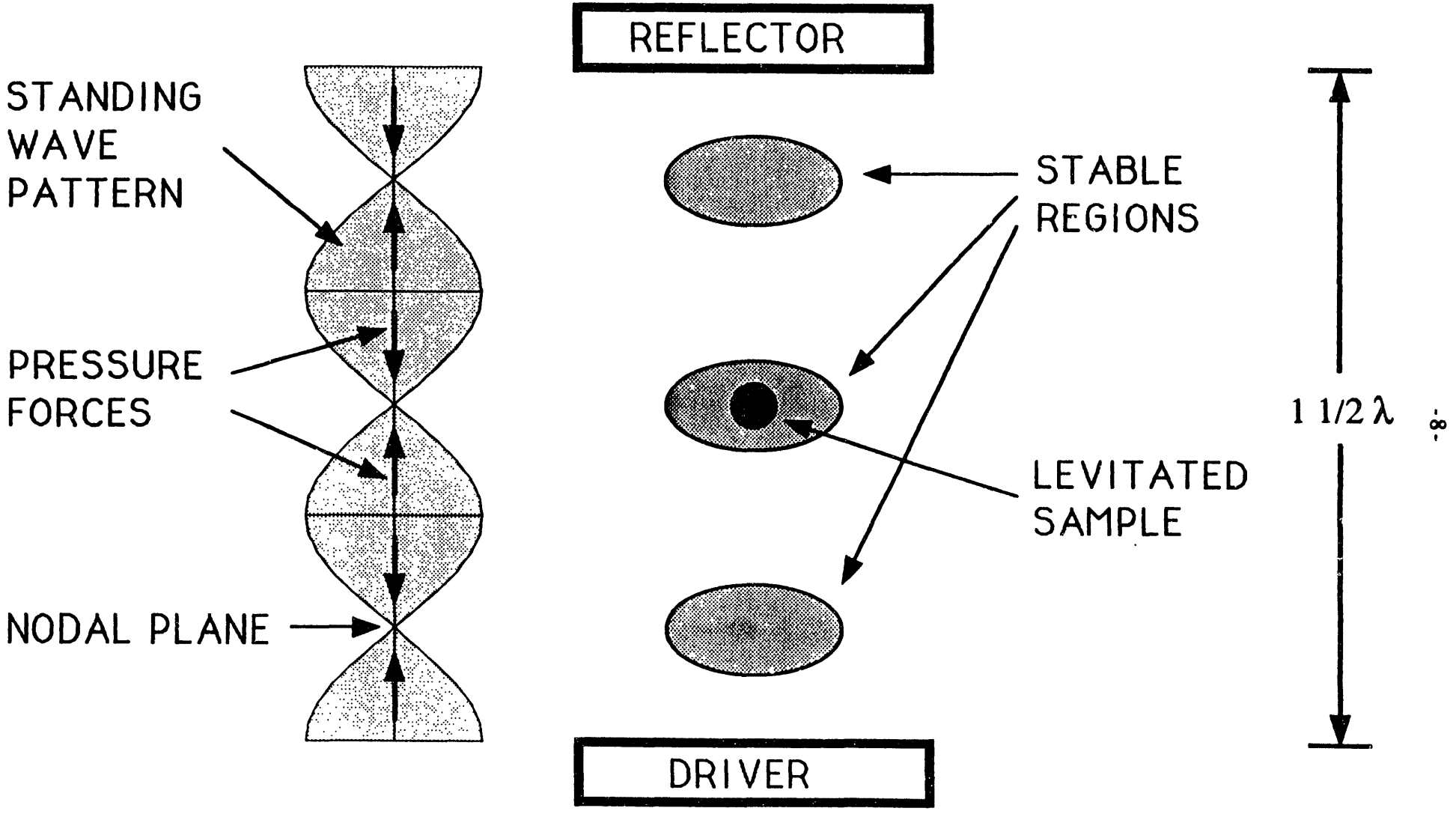

Figure 1-1: Principle of acoustic levitation. The driver/reflector seperation, 1.5 wavelengths in this case, can be any integral multiple of half-wavelengths.

contrast to vertical wind tunnels, where the small scale of the droplet, compared with the mean and turbulent flow scales, makes precise positioning difficult. The steady and repeatable nature of the support allows investigation of microphysical behavior such as phase change or hydrometeor evolution which may occur on time scales of minutes. Experiments of this type are extremely difficult in vertical wind tunnels and impossible in free fall testing.

The small size of the acoustic chamber (typically a few centimeters in both diameter and height), coupled with the stable hydrometeor support, provides advantages both in terms of diagnostic capability and environmental control. For example, video or still cameras can be located within a few centimeters of the levitation region, allowing high resolution photography of the hydrometeor. Other diagnostics such as microwave or electrostatic probes also benefit from close proximity to the sample.

The small volume of the test chamber in the Vertical Facility allows relatively rapid variations of the environment around the hydrometeor. It is possible, therefore, to observe the effect of varying environmental parameters such as temperature, humidity, aerosol content and trace gases on hydrometeor evolution, in both quasi-static and dynamic environments.

1.3 Motivation for Developing Two Facilities

Depending on the particular experiment conducted, it may or may not be necessary to simulate the flow field around the hydrometeor in addition to simulating ambient temperature and humidity conditions. Consequently, two separate levitation facilities have been developed. In one, a vertically oriented acoustic levitator utilizes a strong acoustic field to support objects against the force of gravity. The configuration of this facility is depicted in Fig. 1-2 (a). The surrounding medium in which the suspended object is held is essentially motionless. In the second facility, shown schematically in Fig. 1-2 (b), a small vertical wind tunnel provides the levitating force on the suspended object. This force, arising from aerodynamic drag on the object, opposes the gravitational force on it. In this facility, a horizontally oriented acoustic field is used to stabilize the suspended object within the flow field of the wind tunnel. The

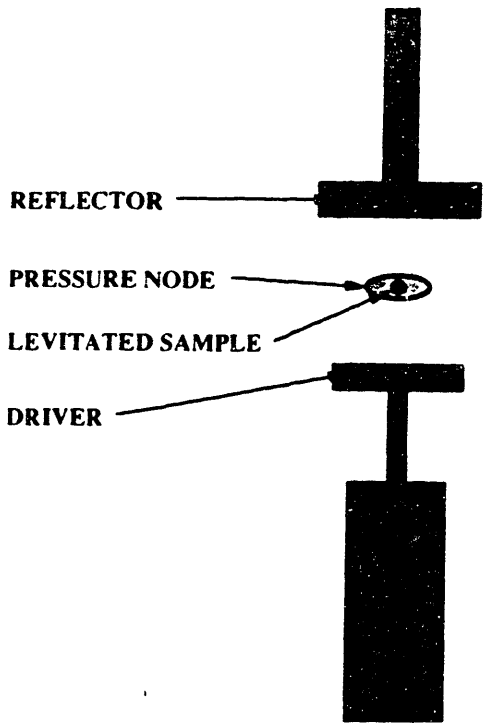

(a) VERTICAL FACILITY

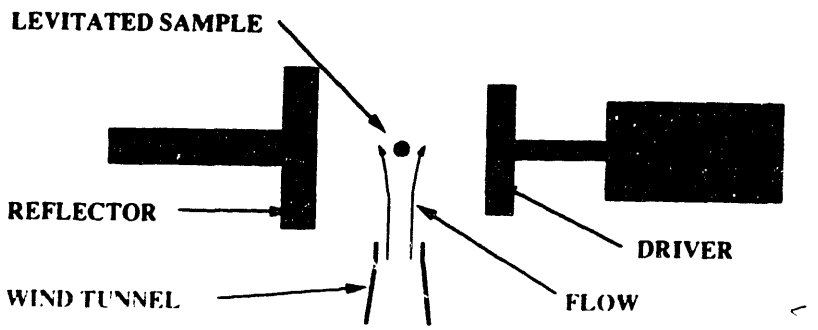

(b) VENTILATED FACILITY

Figure 1-2: Principle of operation of the two levitation facilities: (a) Vertical Facility, (b) Ventilated Facility

motion of the surrounding medium is approximately that of the terminal velocity of the suspended sample.

Carefully controlled collisions between various particles are possible in the ventilated test facility. The primary advantage of utilizing acoustic radiation in this facility is that precise control of wind tunnel flow speed and turbulence levels is not required. The acoustic field provides positional stabilization, and the suspended hydrometeor is therefore less sensitive to flow perturbations. In addition, the ventilated test facility is capable of accurately reproducing the flow field around free falling hydrometeors, with negligible secondary effects resulting from the acoustic field present.

1.4 Outline of the Thesis

The theory of acoustic levitation is presented in Chapter 2. The effects that give rise to the levitation phenomenon are described in detail. Based on mathematical models, predictions are made concerning the behavior of solid and liquid samples in the acoustic field. These effects include stability of samples held in the acoustic field and the deformation of liquid droplets. In Chapter 3, the major design issues concerning the development of the acoustic levitation hardware are discussed. Certain criteria are cited that ensure proper operation of the apparatus. A detailed description of the baseline acoustic levitator is then presented, along with the relevant operating parameters of the device. Chapter 4 describes in detail the vertical and ventilated facilities. Critical design issues concerning the implementation of acoustic levitation in each facility are studied. The calibration and operation of both facilities is discussed. A series of validation experiments are conducted in Chapter 5. The limitations of the facility are compared with the theoretical predictions. These experiments include studies of the levitation limits on solid and liquid hydrometeors, the effect of the acoustic field on molecular diffusion processes, and the effect of shape distortions of water droplets arising from the acoustic field on terminal velocity in free fall. Conclusions and recommendations are presented in Chapter 6.

Chapter 2
Theory of Acoustic Levitation

2.1 Introduction

Qualitatively, the net force on an object subjected to an acoustic field arises from the nonlinear relationship between the instantaneous pressure and velocity in an acoustic medium. Under certain conditions, this nonlinearity can produce significant pressure gradients over the surface of an object, resulting in an appreciable net force on it. As a result, sufficiently strong acoustic fields can suspend objects against the force of gravity, making it possible to study the objects in a contact-free environment.

In this chapter, numerical and approximate analytical expressions are derived for the net force on a rigid sphere in an acoustic standing wave. Stable locations within the acoustic field are then determined for both gravity-free and 1-g environments. The effect of the acoustic field on liquid samples is also important, as many cloud physics experiments involve liquid water. As a result, a mathematical model is developed and used to predict effects such as droplet deformation, oscillation, and shatter.

2.2 Levitation of Solid Objects

In order to study the effects of a planar acoustic field on an object of arbitrary shape, it is useful to first analyze the simple case of a rigid sphere placed in such a field. By making several reasonable approximations (discussed in the sequel), an analytical solution to this problem is available. The net acoustic force on a rigid sphere is then readily calculated. This result can then be extended to oblate or prolate spheroids without significant loss in numerical accuracy, provided that these spheroids do not deviate significantly from spherical. These small deformations are characteristic of naturally occurring hydrometeors, such as raindrops and graupel particles. For these cases, the net acoustic force can be approximated as the force on an equivalent sphere (defined such that the volume of the sphere equals the volume of the

spheroid). For more complex geometries, the results from the simple spherical analysis can be used to predict only general trends, such as the maximum allowable object dimensions for which acoustic levitation is possible.

In light of these arguments, only the simple case of a rigid sphere in a planar acoustic field is studied here. More complex models, which consider more arbitrary geometries do not enhance the understanding of the physics of acoustic levitation significantly, and are not developed here.

2.2.1 Net Acoustic Force on Rigid Spheres in a Planar Standing Wave

In order to develop expressions for the effect of an acoustic field on a spherical object placed within it, it is necessary to solve the wave equation in three dimensions with appropriate boundary conditions. The development presented here is based on theoretical work done by Louis King in 1934 [1]. In his paper, King developed approximate acoustic force expressions for both travelling and standing waves. King showed that the forces arising from travelling waves are significantly smaller than those arising from planar standing waves. As a result, only standing waves are considered here. The theory developed by King specializes to the case where the radius of the spherical object is significantly smaller than the acoustic wavelength. This makes it possible to derive an approximate analytical expression for the acoustic force. The theory presented here applies to spheres of arbitrary size, and involves a numerical computation of the net acoustic force rather than an approximate analytical expression.

In the subsequent development, an approximate expression for the local pressure variation (δp) in terms of the velocity potential (Φ) is derived. The velocity potential is then expressed as the superposition of the incidental planar standing wave and the divergent scattered wave. Upon application of the boundary conditions at the surface of the spherical obstacle, the wave equation is solved exactly. The pressure variation along the surface of the object, averaged over one period of the standing wave, is then determined. Upon integrating this variation over the surface of the sphere, the net force due to the acoustic field is found. An

approximate analytical expression for this force is developed for small spheres to check for consistency with the King theory, and a numerical method is used to determine the force on larger objects.

2.2.1.1 Problem Description and Boundary Conditions

Given the geometry of the problem to be solved, as shown in Fig. 2-1, it is clear that a spherical coordinate system (r,ϕ,θ) is appropriate. The origin of this system lies at the center of the spherical object, with the line $\theta=0$ normal to the planar standing wave. This line corresponds with the z-axis of the related Cartesian system. We will assume that the object lies a distance h above a velocity nodal plane. Alternatively, we may say that a velocity nodal plane exists at $z = -h$.

We now define the velocity of the acoustic medium at any point by

$$\mathbf{v} = v_r \hat{\mathbf{r}} + v_\phi \hat{\boldsymbol{\phi}} + v_\theta \hat{\boldsymbol{\theta}} \tag{2.1}$$

Clearly, from the symmetry of the problem, $v_\phi = 0$ everywhere. For our purposes, the acoustic medium can be modeled as a compressible, irrotational fluid. This guarantees the existence of a velocity potential, Φ, which relates to the velocity of the fluid as follows:

$$v_r = -\frac{\partial \Phi}{\partial r}, \quad v_\theta = \frac{1}{r}\frac{\partial \Phi}{\partial \theta} \tag{2.2}$$

If we denote $q^2 = v_r^2 + v_\phi^2 + v_\theta^2$, we see that

$$q^2 = \left(\frac{\partial \Phi}{\partial r}\right)^2 + \frac{1}{r^2}\left(\frac{\partial \Phi}{\partial \theta}\right) \tag{2.3}$$

Because the fluid must remain in contact with the spherical obstacle, we have the boundary condition

$$v_r\big|_{r=a} = -\frac{\partial \Phi}{\partial r}\Big|_{r=a} = 0, \quad q^2\big|_{r=a} = \frac{1}{a^2}\left[\frac{\partial \Phi}{\partial \theta}\Big|_{r=a}\right]^2 \tag{2.4}$$

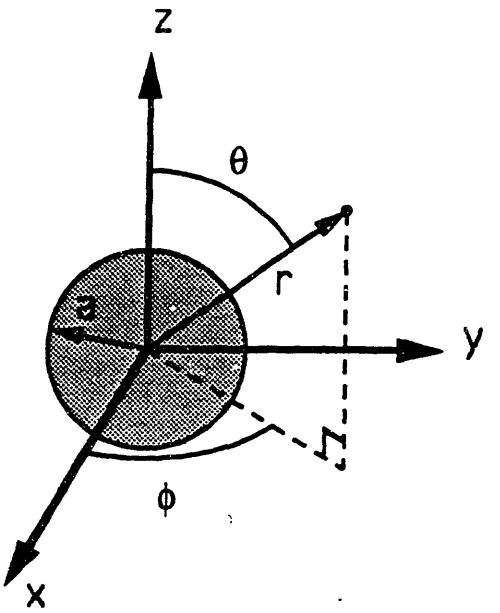

(a)

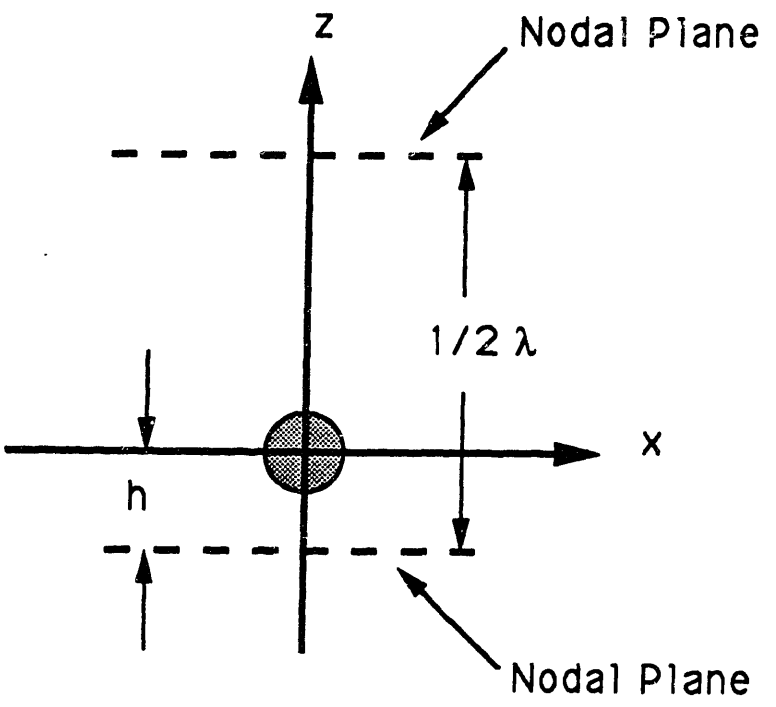

(b)

Figure 2-1: Geometry of the acoustic levitation problem: (a) spherical coordinate system, (b) position of the sphere with respect to the nodal plane of standing wave.

where a is the radius of the sphere. Making the substitution $\mu = \cos\theta$, we obtain

$$q^2|_{r=a} = -\frac{1}{a^2}\left[\left(\frac{\partial\Phi}{\partial\mu}\frac{\partial\mu}{\partial\theta}\right|_{r=a}\right]^2 = \frac{1}{a^2}\sin^2\theta\left[\frac{\partial\Phi}{\partial\mu}|_{r=a}\right]^2 \tag{2.5}$$

which leads to

$$q^2|_{r=a} = \frac{1}{a^2}(1-\mu^2)\left[\frac{\partial\Phi}{\partial\mu}|_{r=a}\right]^2 \tag{2.6}$$

We must now express the pressure deviation, δp, in terms of q and Φ. We make the assumption that the acoustic medium is barotropic (i.e., p is a function of ρ only). For this case,

$$\delta p \cong \rho_0\dot{\Phi} - \frac{1}{2}\rho_0 q^2 + \frac{1}{2}\frac{\rho_0}{c^2}\dot{\Phi}^2 \tag{2.7}$$

The details of the derivation of this expression are presented elsewhere [1]. It should be noted that Eq. (2.7) is correct to terms of the order q^2/c^2. Even at large acoustic energies (140dB, for example) the ratio q/c remains small, so that the expression for the pressure variation, given by Eq. (2.7), is a reasonable approximation[1].

Throughout this development, it is assumed that the center of the sphere is fixed in inertial space. This results in the simple expression for the boundary condition given by Eq. (2.4), since it is assumed that the radial velocity of the fluid at the sphere's surface is the same in an inertial frame as it is relative to the motion of the sphere. The first term in Eq. (2.7) does not contribute to the net acoustic force when time-averaged over one period of the standing wave. However, at any particular instant, this term dominates over the other two. Because the acoustic field varies sinusoidally in time, the force arising from the first term in Eq. (2.7) exhibits the same temporal variation. As a result, within one period of the acoustic field, the

---

[1]This can be verified by expressing q/c in terms of the relative pressure ratio, $\delta p/p_0$. It can be shown [4] that the approximate relationship is $q/c \cong (1/\gamma)(\delta p/p)$, where $\gamma = 1.4$ is the gas constant for air. At an intensity level of 140 dB, the approximate value of δp is 200 Nt/m^2, while p_0 at sea level is approximately 10^5 Nt/m^2. This yields $(q/c)^2 \cong 2 \times 10^{-6}$. Neglecting the higher order terms is therefore justified.

object translates in a direction perpendicular to the nodal plane (i.e., along the z-axis) in a sinusoidal manner. Consequently, over time scales shorter than the period of the acoustic field, the center of the spherical object is not quite inertial. Nevertheless, it can be shown that, for a sufficiently dense object, this translational motion is insignificant. Denoting ζ as the displacement of the spherical object along the z-axis and taking into account only the first term in Eq. (2.7), the equation of motion of the object over short time scales can be approximated as follows:

$$\frac{4}{3}\pi a^3 \rho_1 \ddot{\zeta} = -\int_0^{2\pi}\int_0^{\pi} \delta p \cos\theta \, a^2 \sin\theta \, d\theta \, d\phi = -2\pi a^2 \int_0^{\pi} \rho_0 \dot{\Phi} \cos\theta \sin\theta \, d\theta \qquad (2.8)$$

where ρ_1 represents the density of the spherical object. This equation can be solved for $\ddot{\zeta}$, yielding,

$$\ddot{\zeta} = \left(\frac{3}{2a}\right)\left(\frac{\rho_0}{\rho_1}\right)\int_{-1}^{1} \dot{\Phi} \, \mu \, d\mu \qquad (2.9)$$

The sinusoidal time dependance of this motion becomes apparent by noting that the velocity potential itself varies sinusoidally, with frequency corresponding to that of the acoustic standing wave. The important factor in Eq. (2.9) is the ratio ρ_0/ρ_1, which relates the magnitude of the acoustic force to the mass inertia of the object. For objects of interest (water droplets, ice crystals, etc.), this ratio is small, indicating that the motion of the object subject to the sinusoidally varying pressure force is negligible over times scales longer than the period of the acoustic field. An analysis which takes into account this motion has been performed by King [1], with the conclusion that, for small ρ_0/ρ_1, the motion is indeed negligible.

The second and third terms in Eq. (2.7) contribute less acoustic force over short time intervals. However, because the first term integrates to zero on the average, it is the effects of these two terms that give rise to a steady-state acoustic force on the object, and, hence, the

capability for acoustic levitation. Taking the time average of the pressure variation over one period of the standing wave, we have, on making use of Eq. (2.6) and Eq. (2.7),

$$\delta p\,|_{r=a} = \rho_o \dot{\Phi}|_{r=a} - \frac{\rho_o}{2a^2}(1-\mu^2)\left[\frac{\partial \Phi}{\partial \mu}|_{r=a}\right]^2 + \frac{\rho_o}{2c^2}\left[\dot{\Phi}|_{r=a}\right]^2 \qquad (2.10)$$

Because of the sinusoidal nature of the velocity potential, the first term in this equation does not contribute to the time averaged pressure variation, indicating that the net acoustic force arises from second order effects.

2.2.1.2 General Solution of Wave Equation

The wave equation to be solved for this problem is given by:

$$\frac{1}{c^2}\frac{\partial^2 \Phi}{\partial t^2} = \nabla^2 \Phi \qquad (2.11)$$

which is the familiar wave equation in three dimensions. This equation is based on several underlying assumptions. The first is that the flow is irrotational. The second is that the speed of sound, c, in the medium is a constant, given by $c^2 = dp/d\rho$. For sufficiently small fluid velocity ($q << c$), it can be shown that both approximations are reasonable [5].

The general solution of this wave equation for this problem must now be determined. For the particular case of a spherical object within a planar standing wave, it is obtained by superposing the respective potentials of the incident and scattered waves. This yields a solution of the form:

$$\Phi = \sum_{n=0}^{\infty} \left\{ A_n \psi_n(kr) + A'_n f_n(kr) \right\} (kr)^n S_n \qquad (2.12)$$

where $k = \omega/c$, $\omega = 2\pi f$ and S_n is a surface harmonic of order n. The coefficients A_n and A'_n depend on the boundary conditions of the particular problem to be solved. The obvious restriction that the surface harmonics be finite in all directions restricts the set of possible

surface harmonics to the Legendre polynomials $P_n(\mu)$. The terms $\psi_n(kr)$ and $f_n(kr)$ are spherical wave functions appropriate to the expressions for the incident and diverging waves, respectively. It can be shown [5] that, for a diverging wave, the wave function can be expressed as:

$$f_n(x) = \phi_n(x) - j\psi_n(x) \tag{2.13}$$

where $\phi_n(x)$ is also a spherical wave function. The series expansions of these functions can be found from their corresponding recursion formulas. They are as follows:

$$\psi_n(x) = \frac{1}{1.3\ldots(2n+1)}\left\{1 - \frac{x^2}{2(2n+3)} + \frac{x^4}{2.4.(2n+3)(2n+5)} - \ldots\right\} \tag{2.14}$$

$$\phi_n(x) = \frac{1.3\ldots(2n-1)}{x^{2n+1}}\left\{1 - \frac{x^2}{2(1-2n)} + \frac{x^4}{2.4.(1-2n)(3-2n)} - \ldots\right\} \tag{2.15}$$

Considerable use is made of the following relations satisfied by $\psi_n(x)$ and $\phi_n(x)$:

$$\frac{d\psi_n(x)}{dx} = -x\psi_{n+1}(x), \qquad \frac{d\phi_n(x)}{dx} = -x\phi_{n+1}(x)$$

$$\phi_n(x)\,\psi_{n+1}(x) - \psi_n(x)\,\phi_{n+1}(x) = 1/x^{2n+1}$$

$$\phi_{n+1}(x)\,\psi_{n-1}(x) - \psi_{n+1}(x)\,\phi_{n-1}(x) = (2n+1)/x^{2n+3} \tag{2.16}$$

The velocity potential then becomes:

$$\Phi = \sum_{n=0}^{\infty} A_n \left\{\left(1 - j\,\frac{A_n'}{A_n}\right)\psi_n(kr) + \frac{A_n'}{A_n}\phi_n(kr)\right\}(kr)^n\,P_n(\mu) \tag{2.17}$$

The coefficients A_n are prescribed by the incident standing wave, while the ratios A_n'/A_n relate to the boundary conditions.

In order to facilitate the determination of the remaining coefficients, it is useful to make the substitution:

$$\frac{A_n'}{A_n} = \frac{1}{F_n/G_n - j} \tag{2.18}$$

The ratios F_n/G_n then become the unknown constants. Both F_n and G_n depend only on the nondimensional parameter, α, defined by $\alpha = ka$, where a is the radius of the spherical object and k is the acoustic wave number. The appropriate form of the velocity potential then becomes:

$$\Phi = \sum_{n=0}^{\infty} A_n \frac{\left\{F_n \psi_n(kr) - G_n \phi_n(kr)\right\}}{F_n - jG_n} (kr)^n P_n(\mu) \tag{2.19}$$

2.2.1.3 Application of the Boundary Conditions

The boundary condition at the surface of the sphere is that the component of the velocity in the radial direction is zero. This follows from the fact that the fluid must remain in contact with the surface of the sphere. Making use of Eq. (2.4), we find:

$$\frac{\partial \Phi}{\partial r}\Big|_{r=a} = \sum_{n=0}^{\infty} A_n \left[\frac{\left\{F_n \psi_n(\alpha) - G_n \phi_n(\alpha)\right\}}{F_n - jG_n} n k^n r^{n-1} \right.$$

$$\left. + \frac{\left\{k^2 r G_n \phi_{n+1}(\alpha) - k^2 r F_n \psi_{n+1}(\alpha)\right\}}{F_n - jG_n} k^n r^n \right] P_n(\mu) = 0 \tag{2.20}$$

which reduces to:

$$(n\psi_n - \alpha^2 \psi_{n+1}) F_n = (n\phi_n - \alpha^2 \phi_{n+1}) G_n \tag{2.21}$$

This relation leads to the following choices for F_n and G_n:

$$F_n = \alpha^2 \phi_{n+1}(a) - n\phi_n(a), \quad G_n = \alpha^2 \psi_{n+1}(a) - n\psi_n(a) \tag{2.22}$$

These choices are not unique, as only the ratio F_n/G_n is used in the expression for the velocity potential. At the surface of the object, we have $kr = ka = \alpha$. Making use of the wave function properties (2.16), we get:

$$\Phi \Big|_{r=a} = \sum_{n=0}^{\infty} \frac{A_n}{\alpha^{n+1}} \frac{P_n(\mu)}{F_n - jG_n} \tag{2.23}$$

At this point, only the coefficients A_n need be identified. These relate to the incident acoustic field. The velocity potential for the incident standing wave can be represented in Cartesian coordinates as:

$$\Phi_i = Ae^{j\omega t} \cos\{k(z+h)\} \tag{2.24}$$

or,

$$\Phi_i = \frac{1}{2} Ae^{j\omega t} \left(e^{jkh}e^{jkz} + e^{-jkh}e^{-jkz}\right) \tag{2.25}$$

It will be necessary to express this potential in spherical coordinates. To do this, we make use of the identity:

$$e^{jkz} = \sum_{n=0}^{\infty} (2n+1)\, \psi_n(kr)\, (jkr)^n\, P_n(\mu) \tag{2.26}$$

The incident potential then takes the desired form:

$$\Phi_i = \sum_{n=0}^{\infty} A_n\, \psi_n(kr)\, (kr)^n\, P_n(\mu) \tag{2.27}$$

where:

$$A_n = Ae^{j\omega t} (2n+1) \cos\left(kh + \frac{1}{2} n\pi\right) \tag{2.28}$$

The total potential at the surface of the spherical object then becomes:

$$\Phi\,|_{r=a} = Ae^{j\omega t}\sum_{n=0}^{\infty}\frac{2n+1}{\alpha^{n+1}}\cos\left(kh+\tfrac{1}{2}n\pi\right)\frac{P_n(\mu)}{F_n - jG_n} \tag{2.29}$$

Making the substitutions:

$$R_n(\alpha) = \frac{2n+1}{\alpha^{n+1}}\frac{F_n(\alpha)}{F_n^2(\alpha)+G_n^2(\alpha)}\cos\left(kh+\tfrac{1}{2}n\pi\right)$$

$$S_n(\alpha) = \frac{2n+1}{\alpha^{n+1}}\frac{G_n(\alpha)}{F_n^2(\alpha)+G_n^2(\alpha)}\cos\left(kh+\tfrac{1}{2}n\pi\right) \tag{2.30}$$

results in an even simpler form:

$$\Phi\,|_{r=a} = A\{\cos(\omega t)+j\sin(\omega t)\}\sum_{n=0}^{\infty}\{R_n(\alpha) - j\,S_n(\alpha)\}\,P_n(\mu) \tag{2.31}$$

Henceforward, the dependence of R_n and S_n on α and the dependence of P_n on μ will be assumed. Taking the real part of this expression, we get:

$$\Phi\,|_{r=a} = A\left\{\cos(\omega t)\sum_{n=0}^{\infty}R_nP_n + \sin(\omega t)\sum_{n=0}^{\infty}S_nP_n\right\} \tag{2.32}$$

2.2.1.4 Determination of Pressure Variation Over Surface of Sphere

We must now manipulate Eq. (2.32) into several forms, which can be substituted into Eq. (2.10) to obtain a formula for the pressure variation over the surface of the spherical object. From (2.32), we obtain

$$\dot{\Phi}\,|_{r=a} = A\omega\left\{-\sin(\omega t)\sum_{n=0}^{\infty}R_nP_n + \cos(\omega t)\sum_{n=0}^{\infty}S_nP_n\right\}$$

$$\left[\dot{\Phi}|_{r=a}\right]^2 = A^2\omega^2\sin^2(\omega t)\left[\sum_{n=0}^{\infty} R_n P_n\right]^2 + \cos^2(\omega t)\left[\sum_{n=0}^{\infty} S_n P_n\right]^2$$

$$-2\sin(\omega t)\cos(\omega t)\left[\sum_{n=0}^{\infty} R_n P_n\right]\left[\sum_{n=0}^{\infty} S_n P_n\right]$$

$$\left[\frac{\partial\Phi}{\partial\mu}|_{r=a}\right]^2 = A^2\cos^2(\omega t)\left[\sum_{n=0}^{\infty} R_n P_n'\right]^2 + \sin^2(\omega t)\left[\sum_{n=0}^{\infty} S_n P_n'\right]^2$$

$$+2\cos(\omega t)\sin(\omega t)\left[\sum_{n=0}^{\infty} R_n P_n'\right]\left[\sum_{n=0}^{\infty} S_n P_n'\right] \qquad (2.33)$$

These expressions, time-averaged over one period of the standing wave, become:

$$\overline{\dot{\Phi}|_{r=a}} = 0$$

$$\overline{\left[\dot{\Phi}|_{r=a}\right]^2} = \frac{1}{2}A^2\omega^2\left\{\left[\sum_{n=0}^{\infty} R_n P_n\right]^2 + \left[\sum_{n=0}^{\infty} S_n P_n\right]^2\right\}$$

$$\overline{\left[\frac{\partial\Phi}{\partial\mu}|_{r=a}\right]^2} = \frac{1}{2}A^2\left\{\left[\sum_{n=0}^{\infty} R_n P_n'\right]^2 + \left[\sum_{n=0}^{\infty} S_n P_n'\right]^2\right\} \qquad (2.34)$$

Upon substitution of Eq. (2.34) into Eq. (2.10), we have, for the time-averaged surface pressure variation,

$$\overline{\delta p} = \frac{\rho_0 A^2}{4a^2}\cdot U(\alpha,\mu) \qquad (2.35)$$

where

$$U(\alpha,\mu) = \alpha\left\{\left[\sum_{n=0}^{\infty} R_n P_n\right]^2 + \left[\sum_{n=0}^{\infty} S_n P_n\right]^2\right\} - (1-\mu^2)\left\{\left[\sum_{n=0}^{\infty} R_n P_n'\right]^2 + \left[\sum_{n=0}^{\infty} S_n P_n'\right]^2\right\} \qquad (2.36)$$

This expression is used in the sequel to predict the deformation of a liquid sample in the acoustic field due to a pressure gradient over its surface. It is also possible to numerically integrate this expression over the surface of the object to obtain the net force on it. However, an analytical approach, which exploits some orthogonality properties of the Legendre Polynomials, produces a more useful result.

2.2.1.5 Net Effect of Acoustic Pressure Distribution on Sphere

We seek an expression for the net force on the object along the z-axis, time-averaged over one period of the standing wave, defined as $\overline{P}$. This is obtained by integrating the component of the time-averaged pressure variation (δp) in the direction of the z-axis over the entire surface of the sphere. Hence:

$$\overline{P} = -\int_0^{2\pi}\int_0^{\pi} (\overline{\delta p}\cos\theta)\, a^2 \sin\theta \, d\theta \, d\phi \tag{2.37}$$

or

$$\overline{P} = -2\pi a^2 \int_{-1}^{1} \overline{\delta p}\, \mu \, d\mu \tag{2.38}$$

where the overbar ($\overline{\ }$) denotes integration with respect to time over one period of the standing wave. From Eq. (2.35), we obtain,

$$\overline{P} = -\frac{1}{2}\pi\rho_0 A^2 \int_{-1}^{1} U(\alpha,\mu)\, \mu \, d\mu \tag{2.39}$$

At this point, use is made of the following properties of Legendre polynomials:

$$\int_{-1}^{1} \mu\, P_n(\mu)\, P_m(\mu)\, d\mu = \begin{cases} \dfrac{2(n+1)}{(2n+1)(2n+3)} & m = n+1 \\ 0 & m > n+1 \end{cases} \tag{2.40}$$

$$\int_{-1}^{1} (1-\mu^2)\, \mu\, P'_n(\mu)\, P'_m(\mu)\, d\mu = \begin{cases} \dfrac{2n(n+1)(n+2)}{(2n+1)(2n+3)} & m = n \\ 0 & m > n \end{cases} \tag{2.41}$$

As a result, the expression for the net acoustic force takes the form,

$$\overline{P} = -2\pi\rho_0 A^2 \sum_{n=0}^{\infty} \frac{n+1}{(2n+1)(2n+3)} \left\{ R_n R_{n+1} + S_n S_{n+1} \right\} \left\{ \alpha^2 - n(n+2) \right\} \tag{2.42}$$

Making use of the definitions of $R_n(\alpha)$ and $S_n(\alpha)$, we obtain, after some manipulation,

$$R_n R_{n+1} + S_n S_{n+1} = (-1)^{n+1} \frac{(2n+1)(2n+3)}{2\alpha^{2n+3}} \frac{F_{n+1}F_n + G_{n+1}G_n}{\left[F_n^2 G_n^2\right]\left[F_{n+1}^2 G_{n+1}^2\right]} \sin(2kh) \tag{2.43}$$

Finally, combining Equations (2.42) and (2.43), we obtain,

$$\overline{P} = -\pi\rho_0 A^2 \sin(2kh)\, T(\alpha) \tag{2.44}$$

where,

$$T(\alpha) = \sum_{n=0}^{\infty} (-1)^n \left(\frac{n+1}{\alpha^{2n+3}}\right) \frac{F_{n+1}F_n + G_{n+1}G_n}{\left[F_n^2 G_n^2\right]\left[F_{n+1}^2 G_{n+1}^2\right]} \left\{ \alpha^2 - n(n+2) \right\} \tag{2.45}$$

The function $T(\alpha)$ can be regarded as a normalized acoustic force. This function represents the dependance of the acoustic force on the size of the suspended sphere for a given acoustic field strength. It is interesting to note that the net force varies sinusoidally with h, the distance between the center of the object and the nodal plane of the standing wave. We see that there are two points within each wavelength for which the force is maximized, corresponding to $kh = \pi/4$ and $kh = 3\pi/4$. This expression for the net acoustic force may be calculated to an arbitrary

number of terms to obtain an explicit value for the force on a spherical object placed within the acoustic field.

At this point, it is appropriate to compare the results obtained by King [1] with the theory developed here. For small objects ($\alpha<<1$), an approximate expression for the net acoustic force is readily obtained. We have, for small α,

$$F_0 \cong \frac{1}{\alpha},\ F_1 \cong \frac{2}{\alpha^3},\ F_2 \cong \frac{9}{\alpha^5}, \text{ etc.}, \qquad G_n G_{n+1} \ll F_n F_{n+1} \tag{2.46}$$

which leads to

$$T(\alpha) \cong \frac{5}{6}\alpha^3, \quad \alpha << 1. \tag{2.47}$$

and

$$\overline{P} \cong -\frac{5}{6}\pi\rho_0 A^2 \alpha^3 \sin(2kh), \quad \alpha << 1 \tag{2.48}$$

This result is consistent with results from King's work on acoustic levitation. It is interesting to note that the acoustic force on small spherical objects varies as the cube of the object's radius. Since the mass also varies as the cube of the radius, objects of all sizes (all having the same density) will be accelerated uniformly in the presence of the acoustic field. Furthermore, this indicates that the ability to suspend small objects against gravity depends only on the energy of the acoustic field in relation to the density of the object, irrespective of the size of the object. Note that this effect is valid only for a sphere with diameter considerably shorter than the acoustic wavelength, corresponding to the case where $\alpha << 1$.

It is useful to express Eq. (2.44) in terms of the time averaged energy density of the acoustic field, defined as $\overline{E}$. By making the substitution $\overline{E} = \frac{1}{2}\rho_0 k^2 A^2$, which relates the energy density of a standing wave to its amplitude, we obtain

$$\overline{P} = 2\pi \frac{\overline{E}}{k^2} T(\alpha) \sin(2kh) \tag{2.49}$$

2.2.1.6 Levitation Limit for Large Spheres

For larger objects, the net acoustic force is approximated using Eq. (2.45). In Fig. 2-2, the nondimensional acoustic force, $T(\alpha)$, is plotted against α so that the approximation for small objects can be compared with the more accurate numerical result. It is apparent that the approximation is valid for $\alpha < 0.5$. Beyond this point, the net acoustic force falls off rapidly with increasing sample size. It is clear that, as α approaches 2, the net acoustic force vanishes. This point represents the fundamental theoretical limit to acoustic levitation, as the acoustic energy required for suspension against gravity approaches infinity. This rapid reduction in levitating force is related to the fraction of the acoustic wavelength spanned by the spherical object. As the parameter α becomes larger, the upper and lower surfaces of the object enter regions of the acoustic field where the local pressure deviation diminishes the net acoustic force. For sufficiently large α, this effect eventually cancels the net upward force arising from the pressure deviation near the equator of the object.

In order to support this claim, the pressure distributions over the surfaces of spheres of several sizes were computed numerically. The model assumes each sphere to be located at the point of maximum net acoustic force ($kz_{eq}=\pi/4$). For each trial, the acoustic energy was selected to provide a net force equal to the weight of the sphere. The results are displayed in Fig. 2-3. In this figure, the normalized pressure deviation from ambient is plotted in inverse polar coordinates as a function of the location along the surface of the sphere. The plots help to visualize the pressure distribution, and provide insight into the relative magnitude of the distribution over the sphere. In the absence of any pressure deviation, the plot reduces to a unit circle. In regions of increased pressure, the radial coordinate is less than unity, indicating that the net acoustic force in these regions is directed inward (i.e., toward the center of the sphere). Conversely, in regions of diminished pressure, the radial coordinate is greater than unity, indicating that the net force is directed outward (i.e., radially from the sphere). Using this convention provides a direct visual correspondance between the distribution of the pressure

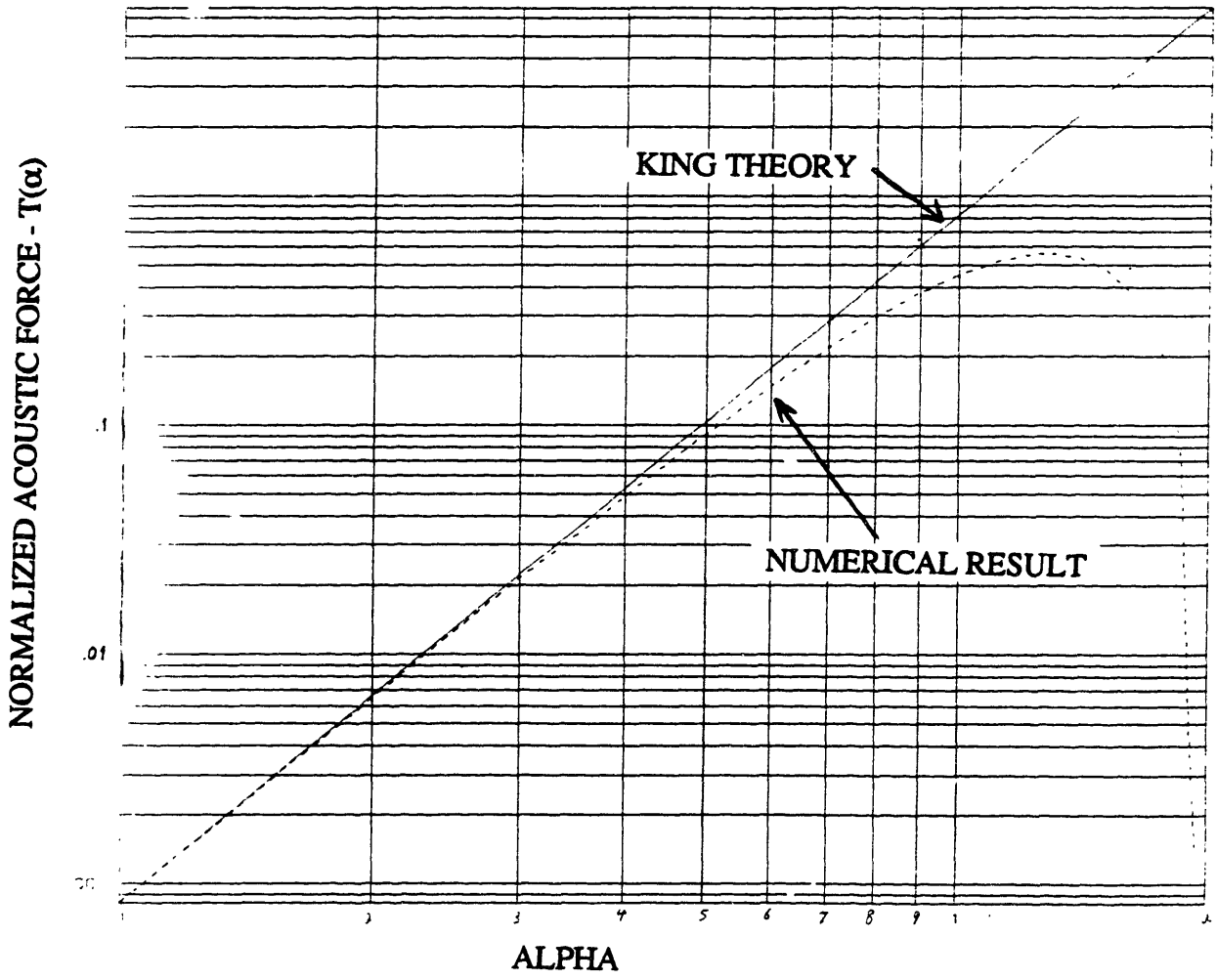

Figure 2-2: Normalized acoustic force on a sphere as a function of α. The solid line represents the approximation for small α, while the dashed line represents the more precise numerical solution. Note the rapid falloff in acoustic levitating capability for $\alpha > 1$.

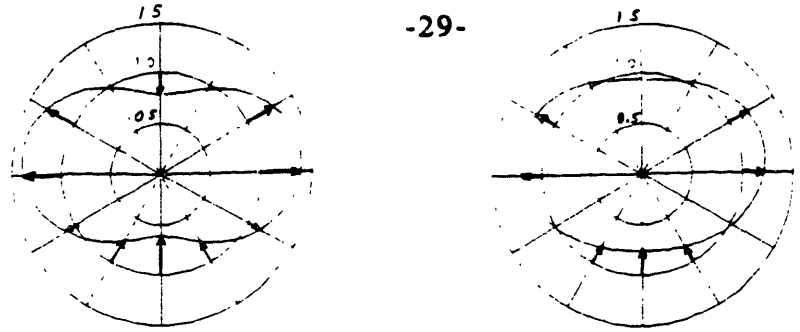

(a) $\alpha = 0.1$

(b) $\alpha = 0.2$

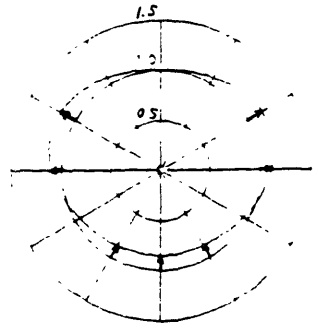

(c) $\alpha = 0.5$

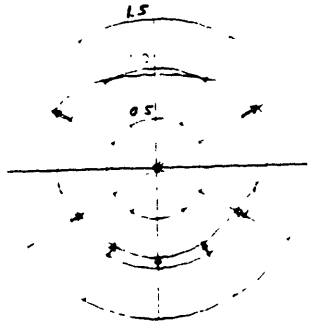

(d) $\alpha = 1.0$

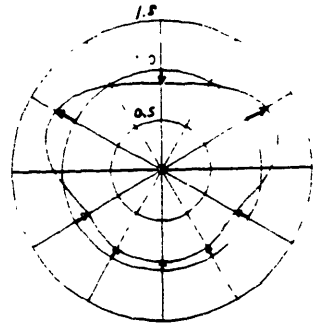

(e) $\alpha = 1.2$

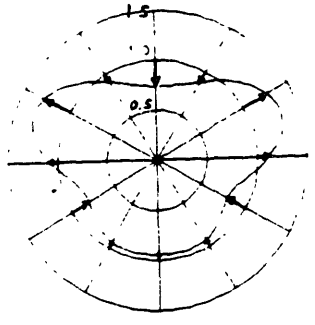

(f) $\alpha = 1.4$

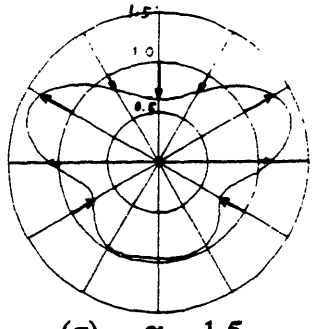

(g) $\alpha = 1.5$

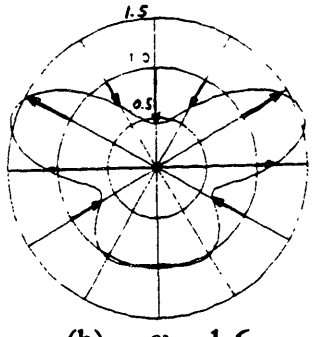

(h) $\alpha = 1.6$

Figure 2-3: Visualization of the distribution of pressure forces over surface of spheres of different sizes. Plots (a) through (h) correspond to $\alpha = 0.1, 0.2, 0.5, 1.0, 1.2, 1.4, 1.5, 1.6$, respectively. In all cases, $E = 1$. For each polar plot, the radial coordinate corresponds to the normalized magnitude of the local pressure force. Points on the unit circle correspond to a local surface pressure pressure equal to the ambient value. Over regions of increased pressure, the radial coordinate is less than unity, indicating a net inward force on the sphere. Over regions of decreased pressure, the radial coordinate is greater than unity, indicating a net outward force. The relationship between the pressure and the radial coordinate is linear.

forces and the resulting effect on deformable samples placed in the acoustic field, such as water droplets (See Section 2.3). For small spheres ($\alpha<1$), the pressure distribution is rather well-behaved, with the net upward force arising from both increased pressure below and reduced pressure above the sphere. However, for larger values of α, a region of increased pressure develops above the sphere, which eventually cancels the upward force from below. This explains the sharp decrease in levitating capability for larger objects.

2.2.2 Stability of Spheres in Acoustic Levitation Environment

We must now determine the equilibrium position of a sample suspended in the acoustic field. To do this, it is useful to fix the coordinate system to the nodal plane below the sample. The coordinate z is then redefined as the time-varying distance of the center of the sample from the nodal plane of the standing wave. The equation of motion for the sample can then be expressed in terms of z. It should be noted that, for the case of a pure standing wave, neutral stability exists in all directions parallel to the nodal planes.

2.2.2.1 Gravity-Free Environment

In the absence of gravity, the only force acting on the suspended object is that of the acoustic field. Force equilibrium requires that:

$$z_{eq} = \frac{n\pi}{2k} \tag{2.50}$$

where n is an integer. The stability of each equilibrium location can be assessed by analyzing small perturbations from this equilibrium condition. Denoting the deviation of the sample from its equilibrium location by δz, we obtain

$$\overline{\delta P} = 2\pi \frac{\overline{E}}{k^2} T(\alpha) \sin\{[2k(z_{eq}+\delta z]\} \tag{2.51}$$

Linearizing about the equilibrium position, we obtain

$$\overline{\delta P} = 4\pi (-1)^n T(\alpha)\, \delta z = \frac{4}{3}\pi a^3 \rho_1 \ddot{\delta z} \tag{2.52}$$

The resulting equation of motion then becomes

$$\ddot{\delta z} + (-1)^{n+1} \frac{3T(\alpha)}{\alpha^3} \frac{\overline{E} k^2}{\rho_1} \delta z = 0 \tag{2.53}$$

It is apparent that the motion is stable only when n is odd. Thus stable nodes exist at z_{eq}= $\pi/2k$, $3\pi/2k$, etc. These correspond to the pressure nodes (or velocity antinodes) of the acoustic standing wave.

In the presence of disturbances, the sample will oscillate about its equilibrium position in a direction normal to nodal plane. The frequency of this oscillation is given by:

$$\omega_{osc} = \sqrt{\frac{3T(\alpha)}{\alpha^3} \frac{\overline{E} k^2}{\rho_1}} \tag{2.54}$$

For small samples, we may use the expression given for $T(\alpha)$ in Eq. (2.45). Thus,

$$\omega_{osc} \cong \sqrt{\frac{5}{2} \frac{\overline{E} k^2}{\rho_1}} \tag{2.55}$$

2.2.2.2 Levitation Against Gravity

With gravity directed normal to the standing wave, the equilibrium location is below that which exists without gravity. Equating forces, we have:

$$\frac{4}{3}\pi a^3 \rho_1 g = 2\pi \frac{\overline{E}}{k^2} \sin(2kz_{eq})\, T(\alpha) \tag{2.56}$$

which leads to two possible equilibrium positions:

$$2kz_{eq} = \begin{cases} \sin^{-1}\left[\frac{2}{3}\left(\frac{\rho_1}{\rho_0}\right)\left(\frac{\alpha^3}{T(\alpha)}\right)\left(\frac{\rho_0 g}{\overline{E}\,k}\right)\right] & \text{(lower equilibrium)} \\ \pi - \sin^{-1}\left[\frac{2}{3}\left(\frac{\rho_1}{\rho_0}\right)\left(\frac{\alpha^3}{T(\alpha)}\right)\left(\frac{\rho_0 g}{\overline{E}\,k}\right)\right] & \text{(upper equilibrium)} \end{cases} \tag{2.57}$$

As shown in Fig. 2-4, the lower equilibrium location is unstable. If the object is perturbed from this location in the downward direction, it moves into a region of reduced levitating force. As a result, the net force on the object is downward, causing it to be accelerated in that direction. The acoustic force is therefore further diminished. The reverse is true for perturbations in the upward direction. Hence, the lower equilibrium position is unstable. Conversely, the upper location given by Eq. (2.57) is stable. Here, small perturbations result in acoustic restoring forces which return the object towards equilibrium. From Eq. (2.56), it follows that the minimum acoustic energy required for levitation against gravity is given by

$$\overline{E}_{min} = \frac{2}{3}\left(\frac{\rho_0 g}{k}\right)\left(\frac{\alpha^3}{T(\alpha)}\right)\left(\frac{\rho_1}{\rho_0}\right) \tag{2.58}$$

For small objects, it is again possible to approximate $T(\alpha)$ by Eq. (2.52). This yields, for small samples,

$$\overline{E}_{min} \cong \frac{4}{5}\left(\frac{\rho_0 g}{k}\right)\left(\frac{\rho_1}{\rho_0}\right) \tag{2.59}$$

As expected, the minimum required acoustic energy depends only on the wavelength of the acoustic field and the densities of the sample and surrounding medium.

A useful nondimensional parameter associated with levitation against gravity is the ratio of the acoustic energy density present to the minimum value required for levitation. Thus, defining this factor as $\tilde{E} = \overline{E} / \overline{E}_{min}$, the equilibrium condition becomes

$$2kz_{eq} = \pi - \sin^{-1}\left(\frac{1}{\tilde{E}}\right) \tag{2.60}$$

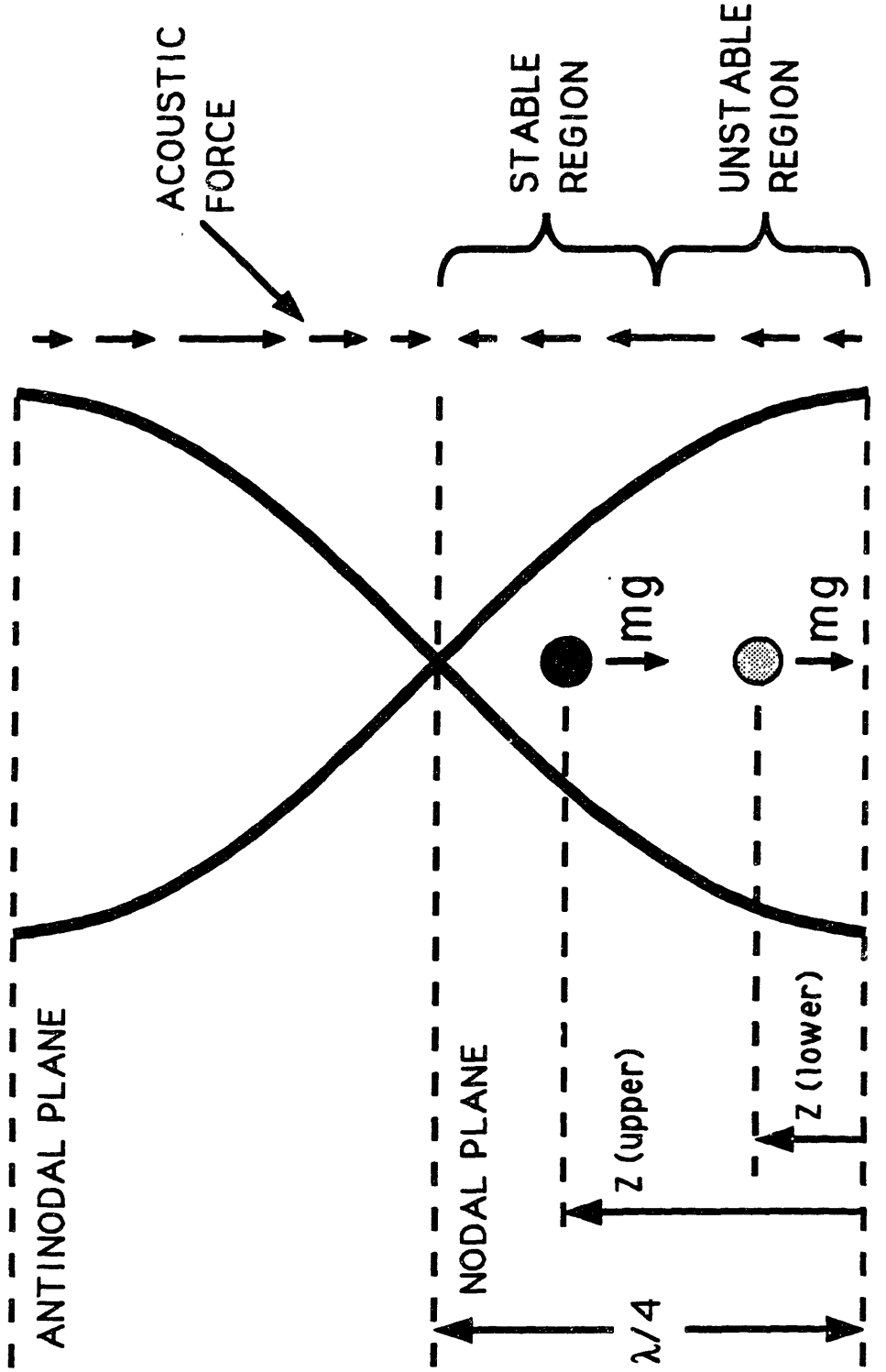

Figure 2-4: Vertical stability of a sphere in an acoustic field in the presence of gravity. Equilibrium is achieved when the acoustic force on the sphere just cancels the gravitational force on it. In the stable region (corresponding to the upper equilibrium location), the gradient of the acoustic force field is such that a sphere perturbed from this equilibrium is subjected to a net force which drives it back to the equilibrium location. In the unstable region (corresponding to the lower equilibrium location), the reverse is true.

The use of this parameter simplifies the equation of motion of the sample for small oscillations about equilibrium. For small perturbations from equilibrium, we have, from Eq. (2.56) and Eq. (2.60),

$$\frac{4}{3}\pi a^3 \rho_1 \ddot{\delta z} = -\frac{4}{3}\pi a^3 \rho_1 g + \frac{4}{3}\pi a^3 \rho_1 g \tilde{E} \sin\left[2k(z_{eq}+\delta z)\right] \tag{2.61}$$

which, after linearization, yields

$$\frac{4}{3}\pi a^3 \rho_1 \ddot{\delta z} = -\frac{8}{3}\pi a^3 \rho_1 gk \sqrt{\tilde{E}^2-1}\ \delta z \tag{2.62}$$

The resulting equation of motion is then

$$\ddot{\delta z} + 2gk\sqrt{\tilde{E}^2-1}\ \delta z = 0 \tag{2.63}$$

From this equation, we can infer that, in the presence of gravity directed normal to the nodal planes of the acoustic standing wave, the frequency of oscillation of a levitated sample about its equilibrium position in that direction is given by:

$$\omega_{osc} = \sqrt{2gk}\ \sqrt[4]{\tilde{E}^2-1} \tag{2.64}$$

2.3 Levitation of Liquid Droplets

It is important to study the effect of the acoustic field on liquid droplets as well as solid objects. It will be shown that, for sufficiently large droplet diameters, surface tensions forces will be inadequate to maintain droplet stability. As a result, large droplets will shatter in the acoustic field. For liquids, this limitation is more constraining than the rapid falloff of levitating force with increasing sample size described in Sec. 2.2.1.7. The deformation limitation is quantified here. This problem is compounded by the possible dynamic effect of induced droplet oscillations in the acoustic field. The excitation of one of the fundamental modes of the droplet due to acoustic effects will, most likely, cause the droplet to shatter prematurely. As a result, this issue is addressed here as well.

2.3.1 Distortion of Droplet Shape from Spherical

When a liquid sample is suspended within the acoustic field, its shape will deform due to the nonuniform pressure distribution at its surface. For large droplets, the surface tension of the fluid may not be large enough to prevent the sample from shattering. The following development attempts to quantify this limit. The theory presented here has been used in earlier work [6] which examined the equilibrium shape of water droplets in free fall, and assumes that the pressure distribution over the surface of the droplet is known. It is also assumed that the droplet is suspended against gravity.

2.3.1.1 Mathematical Model

Initially, it is assumed that the droplet is spherical, so that the acoustic pressure over its surface can be readily obtained from the theory presented in Sec. 2.2.1. By equating internal and external pressures with surface tension forces, an equilibrium shape is determined. The deviation of this shape from spherical results in new boundary conditions for the wave equation of the acoustic field, which will result in a new distribution of acoustic pressure over the surface of the droplet. However, it will be assumed that, for small deformations, the change in the pressure distribution is negligible. Without this simplification, it would be necessary to solve the acoustic wave equation for a general droplet shape, which is neither instructive nor practical. The initial deformation of the droplet from spherical will be adequate in determining droplet stability within the acoustic field.

In the following development, only acoustic, hydrostatic and surface tension forces are taken into account. Circulation internal to the droplet, as well as ambient flow disturbances, if present, are not modeled. The geometry of the deformed droplet is shown in Fig. 2-5.

By balancing forces at the surface of the droplet, we can write

$$\sigma\left[\frac{1}{R_1(\theta)} + \frac{1}{R_2(\theta)}\right] = p_i(\theta) - p(\theta) \qquad (2.65)$$

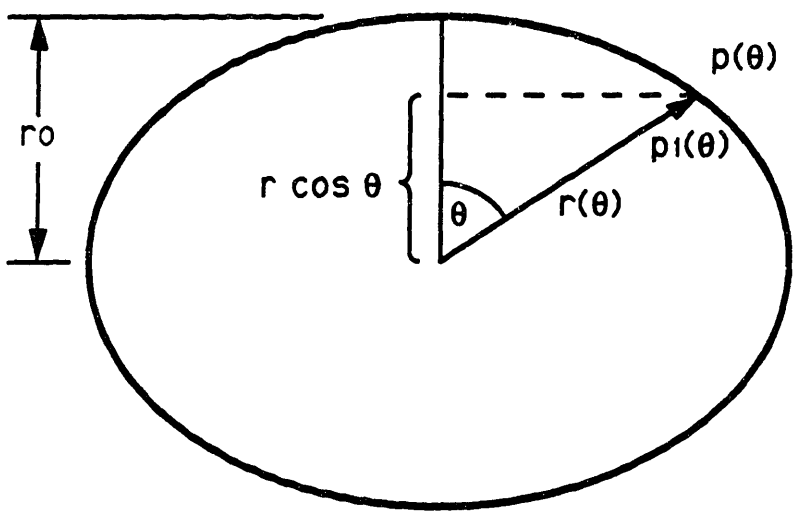

Figure 2-5: Deformation geometry of a liquid droplet. It is assumed that the droplet is radially symmetric about the vertical axis ($\theta = 0$).

where R_1 and R_2 are the local principal radii of curvature of the droplet. Replacing p_i with the local hydrostatic pressure, we obtain

$$\sigma\left[\frac{1}{R_1(\theta)} + \frac{1}{R_2(\theta)}\right] = \rho_1 g (r_o - r\cos\theta) - \delta p(\theta) + \left[p_i(0) - p_0\right] \qquad (2.66)$$

where $p_i(0)$ represents the internal pressure at the upper surface of the droplet, p_0 represents the ambient atmospheric pressure in the absence of an acoustic field, and $\delta p = p - p_0$. In order to convert this equation into a form that can be numerically evaluated, it is necessary to express both $r(\theta)$ and $\delta p(\theta)$ as cosine series. We therefore define,

$$r = a\left(1 + \sum_{n=0}^{\infty} c_n \cos n\theta\right), \quad r_0 = a\left(1 + \sum_{n=0}^{\infty} c_n\right) \qquad (2.67)$$

$$\delta p(\theta) = \frac{r_0 A^2}{4a^2} U(\alpha, \cos\theta) = \frac{\rho_0 A^2}{4a^2} \sum_{n=0}^{\infty} q_n \cos n\theta \qquad (2.68)$$

Making these substitutions, Eq. (2.66) becomes

$$\sigma\left[\frac{1}{R_1(\theta)} + \frac{1}{R_2(\theta)}\right] = \rho_1 g a\left(1 + \sum_{n=0}^{\infty} c_n - \cos\theta - \sum_{n=0}^{\infty} c_n \cos\theta \cos n\theta\right)$$

$$- \frac{\rho_0 A^2}{4a^2} \sum_{n=0}^{\infty} q_n \cos n\theta \qquad (2.69)$$

A relation between the radii of curvature and the coefficients c_n of the deformation is needed. In earlier works [7][8][9], Imai, Savic, and Landau showed that, for reasonably small deformations,

$$\frac{1}{R_1(\theta)} + \frac{1}{R_2(\theta)} \cong \frac{1}{a} J(\theta) \tag{2.70}$$

where

$$J(\theta) = 2 + \sum_{n=0}^{\infty} (n^2-2)\, c_n \cos n\theta + \sum_{n=0}^{\infty} n c_n \sum_{m=1}^{n} \cos (n-2m)\theta \tag{2.71}$$

At this point, two nondimensional parameters, the bond number (N_{BO}) and an acoustic number (N_{AC}) are introduced. They are defined by

$$N_{B0} = \frac{\rho_1 g a^2}{\sigma}, \quad N_{AC} = \frac{\rho_0 A^2 k}{4\sigma\alpha} \tag{2.72}$$

The equation for force balance then becomes

$$J(\theta) = N_{BO}\left(1 + \sum_{n=0}^{\infty} c_n - \cos\theta - \sum_{n=0}^{\infty} c_n \cos\theta \cos n\theta\right) - N_{AC} \sum_{n=0}^{\infty} q_n \cos n\theta \tag{2.73}$$

which can be manipulated into the following form:

$$K - N_{BO} \sum_{n=0}^{\infty} c_n + \frac{1}{2} N_{BO} \sum_{n=0}^{\infty} c_n \left[\cos (n+1)\theta + \cos (n-1)\theta\right] + \sum_{n=0}^{\infty} (n^2-2)\, c_n \cos n\theta$$
$$+ \sum_{n=0}^{\infty} n\, c_n \sum_{m=1}^{n} \cos (n-2m)\theta = - N_{AC} \sum_{n=0}^{\infty} q_n \cos n\theta \tag{2.74}$$

where

$$K = 2 - N_{BO} + N_{BO} \cos\theta. \tag{2.75}$$

By exploiting the orthogonality of the cosine series, it is possible equate terms in cos kθ. This yields the following relationship among the coefficients:

$$\frac{1}{2} N_{BO} (c_{k+1} + c_{k-1}) + (k^2-2)\, c_k + k\, c_k + 2 \sum_{j=k+2}^{\infty} j\, c_j = -N_{AC} q_k, \quad k \geq 2 \qquad (2.76)$$

The coefficient c_1 corresponds to rigid body motion in the vertical direction, and is therefore set to zero for our purposes. These equations can be written in matrix form if the series expansions are truncated after several terms. In this numerical model, only terms up to cos 9θ are considered. The resulting matrix equation is therefore

$$\begin{bmatrix} 4 & N & 8 & 0 & 12 & 0 & 16 & 0 \\ N & 10 & N & 10 & 0 & 14 & 0 & 18 \\ & N & 18 & N & 12 & 0 & 16 & 0 \\ & & N & 28 & N & 14 & 0 & 18 \\ & & & N & 40 & N & 16 & 0 \\ & & & & N & 54 & N & 18 \\ & & & & & N & 70 & N \\ & & & & & & N & 88 \end{bmatrix} \begin{bmatrix} c_2 \\ c_3 \\ c_4 \\ c_5 \\ c_6 \\ c_7 \\ c_8 \\ c_9 \end{bmatrix} = -N_{AC} \begin{bmatrix} q_2 \\ q_3 \\ q_4 \\ q_5 \\ q_6 \\ q_7 \\ q_8 \\ q_9 \end{bmatrix} \qquad (2.77)$$

where $N = \frac{1}{2} N_{BO}$. The constant term, c_0, can be found by invoking conservation of volume, treating the droplet as incompressible fluid. We have, for the volume of the deformed droplet,

$$V = \int_0^{2\pi} \int_0^{\pi} \int_0^{r(\theta)} r^2 \sin\theta \, dr \, d\theta \, d\phi = \frac{2}{3}\pi \int_0^{\pi} r^3(\theta) \sin\theta \, d\theta \qquad (2.78)$$

Substituting the series expansion for the droplet radius, we obtain the approximate expression

$$V \cong \frac{4}{3}\pi a_0^3 + 2\pi a_0^3 \int_0^{\pi} \sum_{n=0}^{\infty} c_n \cos n\theta \sin\theta \, d\theta \qquad (2.79)$$

which holds for reasonably small deformations. For an incompressible sample, this volume must equal the original volume of the sphere. This leads to the constraint:

$$\sum_{n=0}^{\infty} \int_{0}^{\pi} c_n \cos n\theta \sin \theta \, d\theta = 0 \tag{2.80}$$

Isolating the first term yields

$$c_0 = -\frac{1}{2} \sum_{n=2}^{\infty} \int_{0}^{\pi} c_n \cos n\theta \sin n\theta \, d\theta \tag{2.81}$$

Using the trigonometric formula

$$\int_{0}^{\pi} \cos n\theta \sin \theta \, d\theta = \begin{cases} \frac{-2}{n^2-1} & n \text{ even} \\ 0 & n \text{ odd} \end{cases} \tag{2.82}$$

produces the desired result:

$$c_0 = \sum_{n=1}^{\infty} \frac{c_{2n}}{4n^2-1} \tag{2.83}$$

At this point, it is possible to predict the equilibrium shape of any liquid object suspended in the acoustic field. The solution is a function of four non-dimensional parameters. These are: ρ_1/ρ_0, α, $\tilde{E}$, and N_{BO}. The acoustic number, N_{AC}, can be expressed in terms of N_{BO} and α as

$$N_{AC} = \frac{1}{3} \frac{N_{BO}}{T(\alpha)} \tag{2.84}$$

These four parameters are all that is required to completely specify the problem. Assuming that the ambient fluid is air and the droplet is liquid water, the ratio ρ_1/ρ_0 is fixed. Also, at a given acoustic wavelength, the droplet diameter determines both α and N_{BO}. The only other parameter that can be varied is $\tilde{E}$, which is directly related to the acoustic field strength. The

shape of a levitated droplet of water in a given acoustic field is therefore characterized by the two parameters, α and $\tilde{E}$.

2.3.1.2 Predictions Based on Mathematical Model

A numerical model was developed that determines the theoretical shape deformation of a droplet under acoustic levitation. The model computes the equilibrium location of the droplet within the acoustic field, and determines the pressure distribution at that location. Based on this distribution, an equilibrium shape is found. In order to study deformation effects arising from various acoustic field strengths, the theoretical droplet size was held constant at a value corresponding to $\alpha = 0.7$, and the acoustic energy was varied from $\tilde{E} = 1$ to $\tilde{E} = 1.7$. The resulting pressure distribution and equilibrium shape for each trial is shown in Fig. 2-6. At the minimum energy required for levitation, a diameter water droplet whose diameter corresponds to $\alpha = 0.7$ is only slightly distorted. Its top surface is flattened, and its sides are stretched outwards. However, at energies only slightly larger than this minimum value, more severe distortions appear. The upper and lower surfaces become concave, and the droplet as a whole becomes much more flattened. At this point, the local curvature of the droplet at its upper and lower surfaces is quite acute. It is assumed that the surface tension of the actual droplet will be inadequate to maintain stability. At this point, it is predicted that the droplet will shatter under the combined effect of acoustic and gravitational forces. This phenomenon is not part of the model.

It is apparent that, for a given droplet size, there exists a maximum acoustic field energy for which the droplet will not shatter. In order to quantify this relationship, it would be useful to define a parameter characteristic of the magnitude of the deformation. An appropriate choice is the droplet aspect ratio. It is defined as the ratio of the maximum thickness of the droplet in the direction normal to the standing wave to its maximum diameter in the direction parallel to the nodal plane (See Fig. 2-7). The predicted aspect ratios for droplets of various sizes under varying acoustic energies were determined from the model presented above. The results are

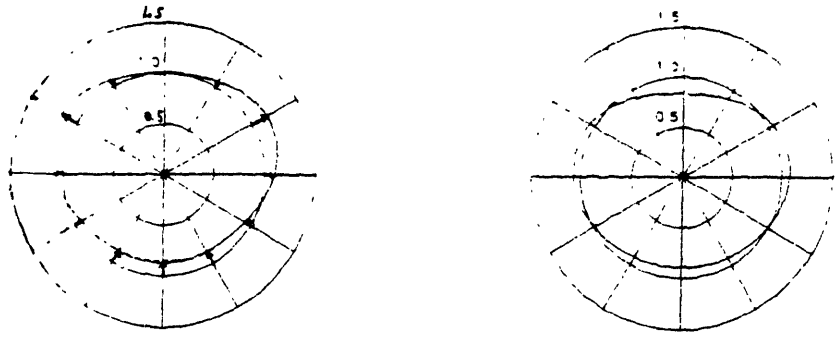

(a) $\tilde{E} = 1$

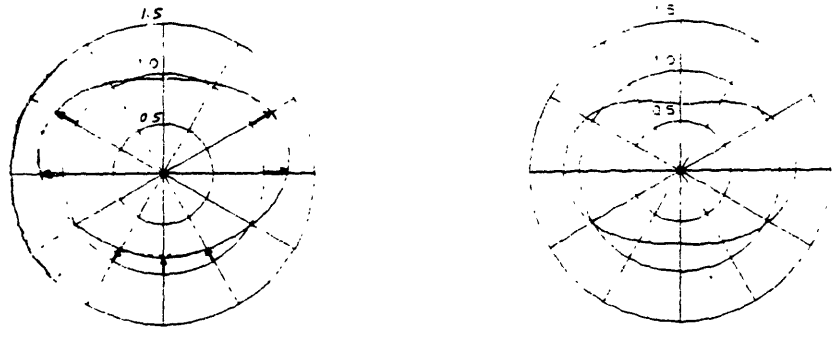

(b) $\tilde{E} = 1.2$

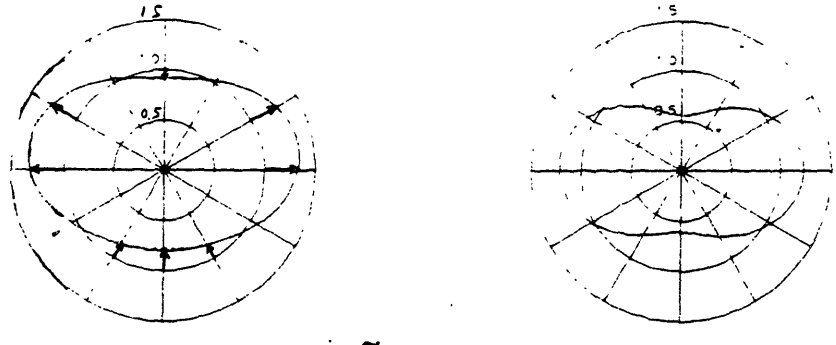

(c) $\tilde{E} = 1.45$

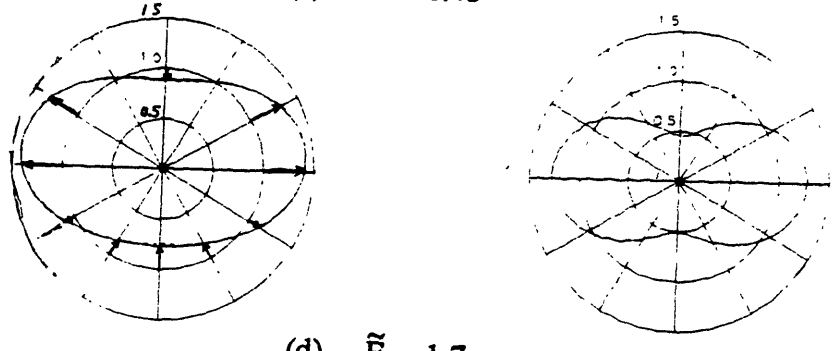

(d) $\tilde{E} = 1.7$

Figure 2-6: Deformation of a water droplet from spherical under the combined effect of gravity and acoustic forces. The inverse radial pressure distributions are shown at left and the corresponding deformed shapes are shown at right for: (a) E = 1, (b) E = 1.2, E = 1.45, E = 1.7. The value of α is 0.7 for all cases. Note the large shape distortions predicted for higher acoustic energies.

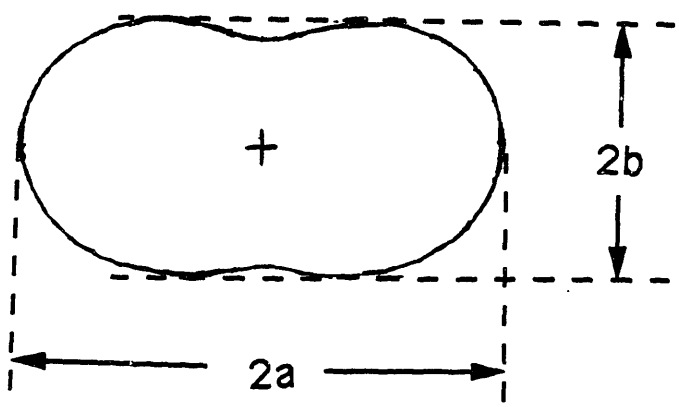

Figure 2-7: Definition of deformed droplet dimensions. The aspect ratio is defined as b/a, and the equivalent radius is (for small deformations) approximately $\sqrt[3]{a^2 b}$

presented in Fig. 2-8. As expected, the droplet shape deteriorates rapidly as the acoustic field strength is increased above the minimum value required for levitation. This implies that, in order to maintain droplet stability, the value of $\tilde{E}$ should be only slightly larger than unity. However, at this level, the droplet is only marginally stable, and transients in the acoustic field will cause the droplet to fall. It is therefore necessary to have excess power in the acoustic field. Thus, a reasonable lower limit for the acoustic energy is $\tilde{E} = 1.2$. The theoretical droplet aspect ratio which corresponds to the anticipated shattering of the actual droplet must be estimated. Referring to Fig. 2-6, it can be inferred that droplet shatter will occur at a theoretical aspect ratio of about 0.5. Finally, from Fig. 2-8, it can be concluded that the largest droplet that can be supported has a value of α equal to 0.85. As expected, this value represents more of a constraint on the size of the droplet capable of being levitated than does the sudden falloff of levitating force for large solid objects.

It is important to note that this theoretical limit is valid only for levitation against gravity. In the absence of gravity, a considerably weaker acoustic field is sufficient to stabilize the liquid droplet. The field strength need only be large enough to prevent loss of positional stability of the droplet in the presence of flow turbulences in the ambient medium. As a result, larger droplets can be suspended within a gravity-free environment without risk of droplet shatter.

2.3.2 Droplet Oscillations in the Acoustic Field

As described in Sec. 2.2.2, the restoring force of the acoustic field on a suspended droplet causes the droplet to undergo oscillations about the equilibrium position in a direction perpendicular to the nodal plane. This creates the potential for excitation of one of the fundamental oscillatory modes of the droplet itself. These oscillations arise from interactions between viscous and inertial forces within the droplet and surface tension forces over its boundary. It has been shown in many texts [10] that the first oscillatory mode of a droplet is given by

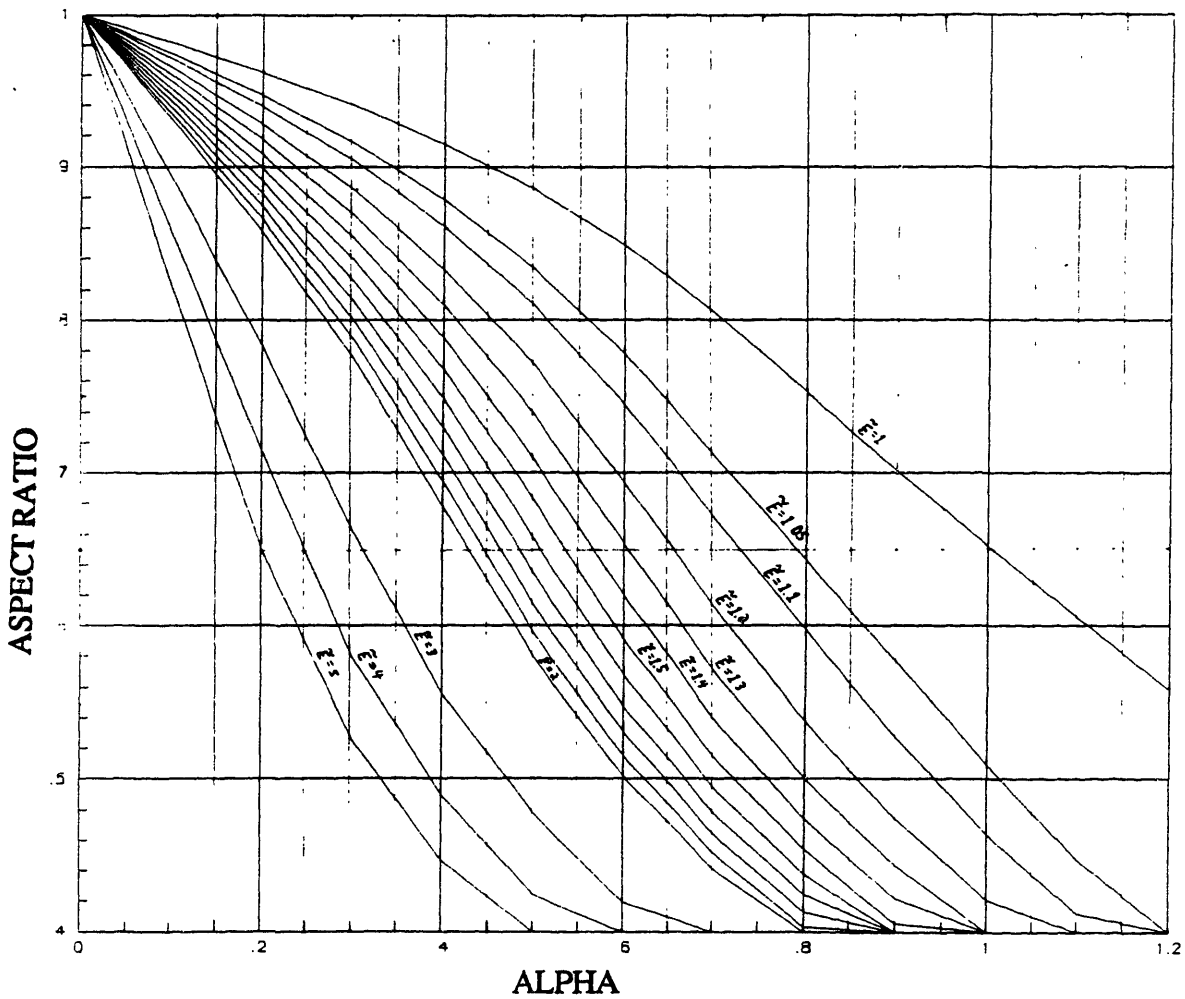

Figure 2-8: Predicted aspect ratio of droplets of various nondimensional size subjected to various acoustic energies.

$$\omega_1 = \sqrt{\frac{8\sigma}{\rho_1 a^3}} \tag{2.85}$$

where a is the radius of the droplet, and σ and ρ are the respective surface tension and density of the droplet.

In the absence of gravity, the acoustic force required to keep the droplet stabilized is low compared to the corresponding case for levitation in the presence of gravity. The acoustic field strength need only be sufficiently strong to prevent ambient disturbances from forcing the sample out of the acoustic region. Because the frequency of droplet motion about the nodal plane induced by the acoustic field decreases with decreasing field strength, it is expected that the frequency of this oscillation will be well below the first resonance of the droplet for the required acoustic energies anticipated in a gravity-free environment.

For levitation against gravity, on the other hand, the oscillations induced by the acoustic field must be considered. Here, the energy of the acoustic field will be much higher, so that the sample can be suspended against the force of gravity. As a result, the frequency of the oscillations induced by the acoustic field will be significantly higher than would be the case in a gravity-free environment. Using Equations (2.63) and (2.82), the relationship between the fundamental oscillatory frequency of the droplet and the frequency of oscillation induced by the acoustic field can be compared. The results are graphed in Fig. 2-9. From the graph, we conclude that excitation of the fundamental mode occurs only at extremely large values of $\tilde{E}$, and then only for large droplets. In these regimes, it is anticipated that the pressure forces alone will be sufficient to cause shattering of the droplet without the added effect of droplet motion. Consequently, it is expected that induced droplet oscillation will not occur for droplets of diameters in the range of interest.

It should be noted that, if desired, others methods are available for intentionally inducing droplet modal oscillations. The most direct method, for example, would be to modulate the intensity of the acoustic field at the desired frequency. The magnitude of the pressure forces on the droplet would then vary sinusoidally over the droplet surface, and shape

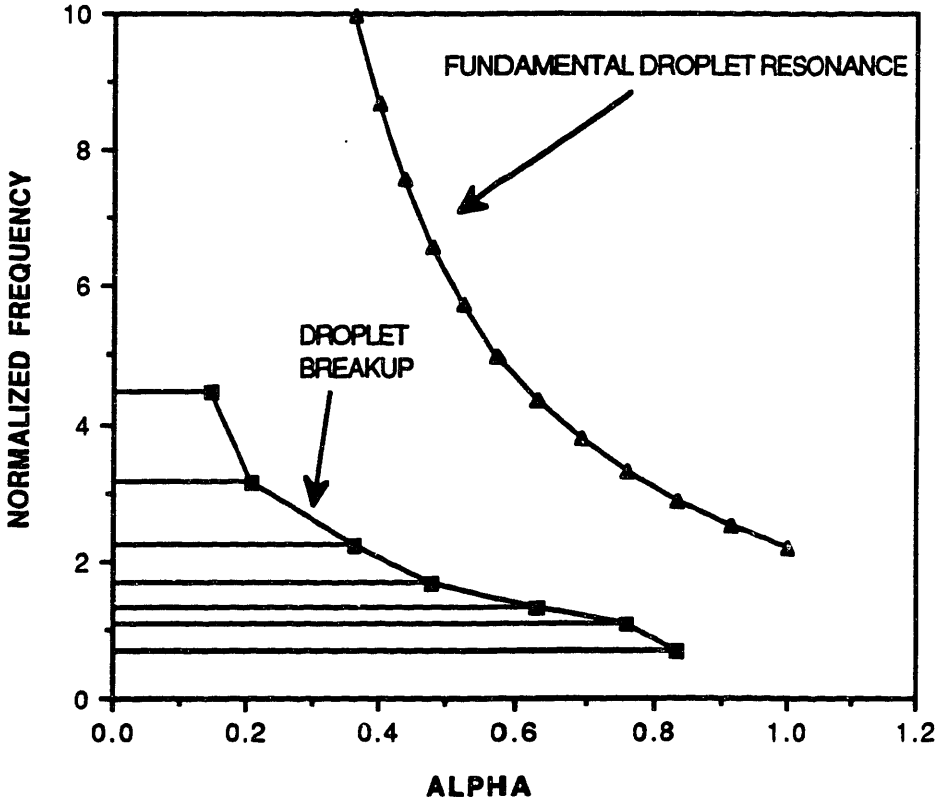

Figure 2-9: Frequency of oscillation in position of a droplet suspended against gravity for various acoustic energies. The droplet breakup limit corresponds to the largest droplet capable of being levitated at a given acoustic energy without droplet shatter, as predicted by Fig. 2-8. The fundamental frequency of shape oscillation of the droplet is shown for comparison. It is clear that the acoustic field is not predicted to induce shape oscillations in the levitated droplet.

oscillations will occur. Unfortunately, the distribution of this forcing over the surface of the droplet cannot be adjusted. As a result, the mode shapes of the droplet under levitation may deviate significantly from the theoretical mode shapes.

Chapter 3
Development of the Acoustic Levitation Hardware

3.1 Principle of Operation

The purpose of the acoustic levitation hardware is to create and maintain a stable acoustic standing wave of sufficient strength to make levitation possible. This acoustic field is generated between a driver and a reflector which define the boundary of the acoustic region, as shown in Fig. 3-1. The driver is an active element, which generates periodic compression waves in the acoustic medium by means of a mechanical displacement. It is excited by a sinusoidally varying electric signal. By designing the driver to exhibit a sharp resonance at the excitation frequency of interest, the magnitude of the compression waves generated is amplified considerably. As a result, the acoustic field created is correspondingly stronger. The compression waves impinge upon the reflector and are scattered back towards the driver. When the separation distance between the driver and reflector is an integral number of half wavelengths of the compression waves, a standing wave is created. The field is maintained because the scattered waves arriving at the driver are in phase with the newly generated waves. Energy is therefore continuously added to the field. Equilibrium is reached when the energy dissipated by viscous mechanisms in the acoustic medium balances the energy delivered by the driver. The acoustic field established in this way has alternating nodal and antinodal planes, as shown in Fig. 3-1. These planes are parallel to the transmitting surface of the driver. By placing the driver and reflector several wavelengths apart, several nodal planes are created, each of which is capable of suspending an object.

3.2 Design of Driver

The design of the acoustic driver is based the design of several earlier devices [2][3][11]. Most of these are designed for containerless processing applications, and are therefore incapable of maintaining ambient conditions suitable for cloud physics experiments.

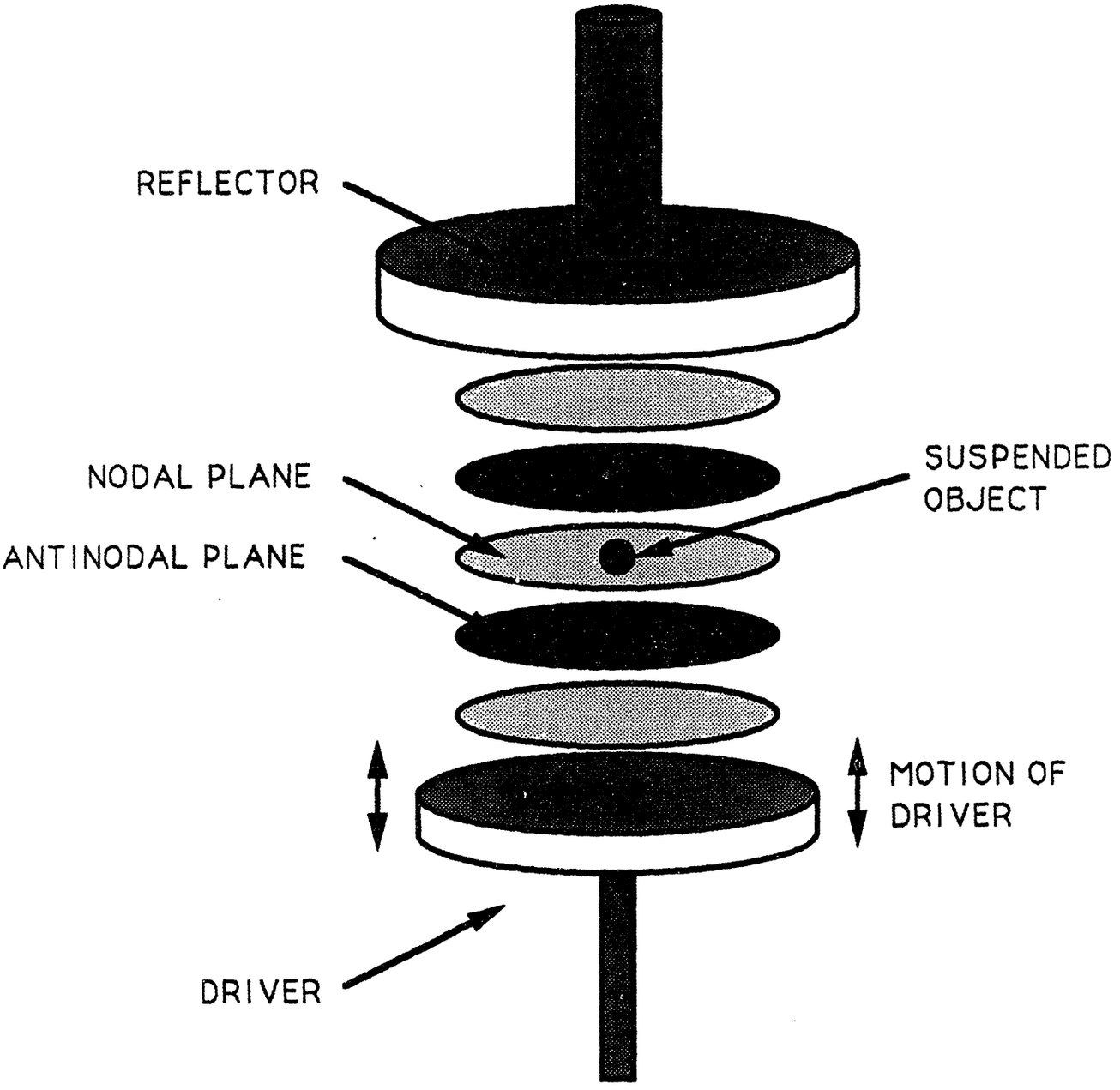

Figure 3-1: Theory of operation of acoustic levitator. Nodal and antinodal planes are interlaced within the acoustic region.

Also, some of these devices operate in closed chambers and do not allow access to diagnostic equipment. The main design goal for the acoustic driver is therefore to suspend objects of interest indefinitely while emulating the ambient conditions that naturally occur in the atmosphere. The acoustic drivers integrated into the two acoustic levitation facilities are essentially identical.

3.2.1 Choice of Operating Frequency

The choice of operating frequency for the acoustic driver represents a trade off between several performance and implementation criteria. Clearly, for levitation purposes, the theory presented in Chapter 2 suggests that the acoustic field have large wavelength. This increases the maximum diameter of a sample capable of being levitated. However, larger wavelengths imply lower frequencies, which, in turn, require larger physical dimensions for the acoustic driver. More importantly, in the interest of safety and comfort, it is desirable that the operating frequency be beyond the range of human hearing. Consequently, the target operating frequency is 23 kHz, which corresponds to an acoustic wavelength of 1.5 cm ($k = 4.19\ cm^{-1}$) in air at room temperature. This is just above the range of human hearing, which extends to 20 kHz.

3.2.2 Design of Driver Elements

The acoustic energy required for levitation is generated by means of an acoustic driver, which transmits compressive waves into the acoustic region. This device resonates at a specific frequency which is determined by its physical dimensions. Incorporated into the acoustic driver are three elements, shown in Fig. 3-2. The first is a resonator, whose dimensions dictate the operating frequency of the driver. The second is an electromechanical actuator, which converts an excitation voltage into a mechanical displacement. The third element is a transmitter, which is responsible for converting the mechanical energy stored

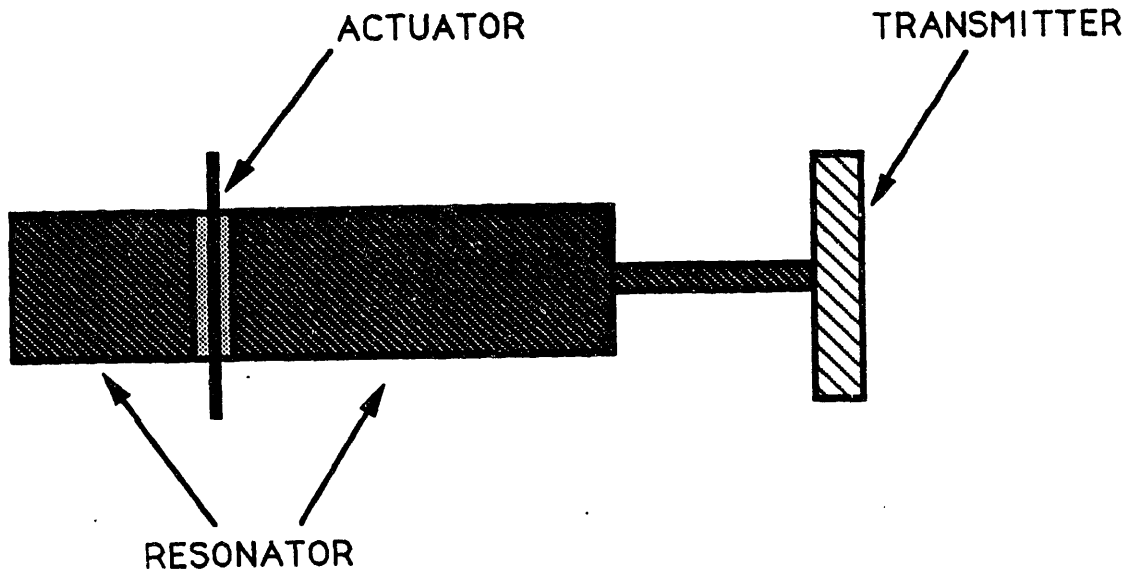

(a)

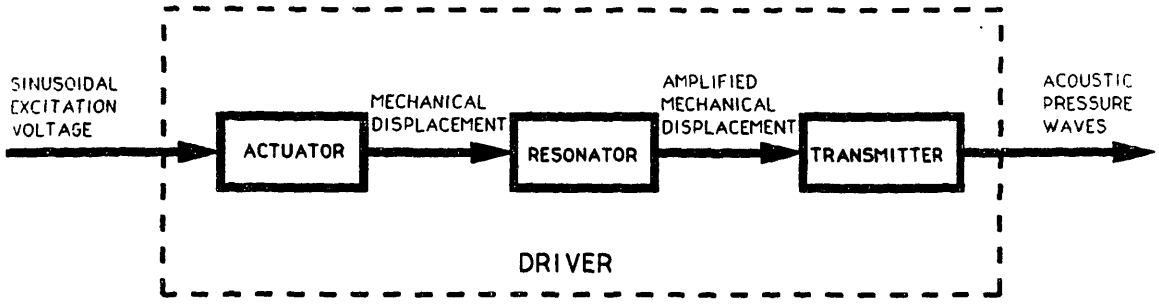

(b)

Figure 3-2: Definitions of the acoustic driver elements: (a) pictorial description, (b) functional description. The driver converts a high voltage sinusoidal signal into a high intensity acoustic compression wave having the same frequency as the excitation.

within the resonator into acoustic pressure waves. The design of each of these elements is presented below.

3.2.2.1 Resonator

The structure of the driver is dictated primarily by the design of the resonator. It is this element that is responsible for amplifying the mechanical displacements created by the excitation voltage. The amplification depends strongly on the relationship between the dimensions of the resonator and the frequency of excitation of this element. Because any object of any geometry will exhibit some sort of resonance, many possible configurations exist. The particular choice of resonator configuration is based on certain desirable properties of the resonance achieved. The first of these properties is large amplification at the required resonant frequency. This suggests the use of a material with low viscous damping, so that dissipation of mechanical energy into heat is minimized. Another property is that the resonant frequency and associated mode shape be predictable and well-behaved. This implies that the required resonance should lie far from any other resonances of the element. Finally, the energy developed within the resonator should be readily coupled to the transmitter.

The resonator chosen for the driver is essentially a rod of circular cross-section vibrating in an axial mode. The governing partial differential equation for this type of vibration is:

$$\frac{E}{\rho}\frac{\partial u}{\partial x} = \frac{\partial u}{\partial t} \tag{3.1}$$

where E and ρ represent the modulus of elasticity and density of the rod, respectively. Assuming that both ends of the rod are free, the modal frequencies are given by

$$\omega_n = \frac{n\pi}{L}\sqrt{\frac{E}{\rho}} \tag{3.2}$$

where L represents the length of the rod. These modal frequencies are spaced far apart, as required. One end of this rod serves as the transmitting end, which creates the necessary compression waves in the acoustic medium. In order to increase the displacement amplitude at this end, it is desirable to taper the rod. Common tapers, for which analytical expressions are available, include conical, exponential and stepped designs. The geometries of these tapers are shown in Fig. 3-3. The amplifications resulting from these geometries are as follows [12]:

$$\frac{V_2}{V_1} = \left(\frac{d_1}{d_2}\right)^2 \qquad \text{(stepped)}$$

$$\frac{V_2}{V_1} = \left(\frac{d_1}{d_2}\right) \qquad \text{(exponential)}$$

$$\frac{V_2}{V_1} = \frac{1}{\cos\frac{\omega L}{2c} - \frac{\omega L d_2}{c(d_1-d_2)}\sin\frac{\omega L}{2c}} \qquad \text{(conical)} \qquad (3.3)$$

where V_2 is the displacement amplitude at the transmitting end, V_1 is the displacement amplitude at the opposite end, ω is the operating frequency, c is the wave propagation velocity, and L, d_1 and d_2 are geometric parameters defined in Fig. 3-3. Clearly, the stepped configuration is capable of providing a much larger displacement amplification. However, the sharp discontinuity in the resonating device results in some dissipation of mechanical energy into heat. This phenomenon is not as pronounced in exponential or conical tapers. Nevertheless, due to its enhanced displacement amplification, the stepped configuration is preferred. The slight loss in efficiency is compensated for by suppling more electrical power to the driver.

3.2.2.2 Actuator

The actuator converts the electrical excitation sinusoid (whose frequency corresponds to the resonant frequency of the resonator) into mechanical energy. Electromagnetic actuators are the simplest elements to use, but these devices have extremely poor response characteristics at

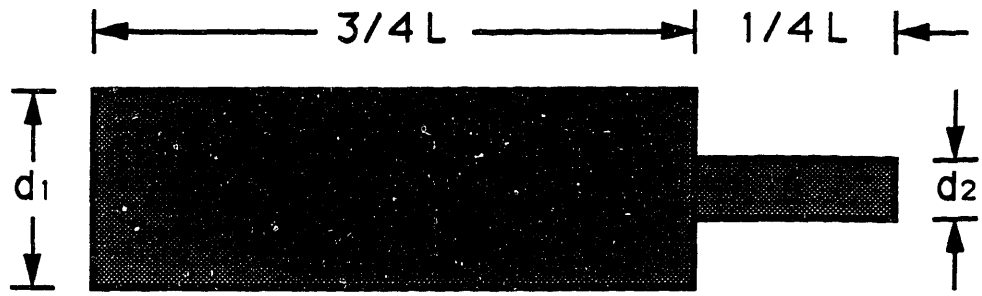

(a) STEPPED

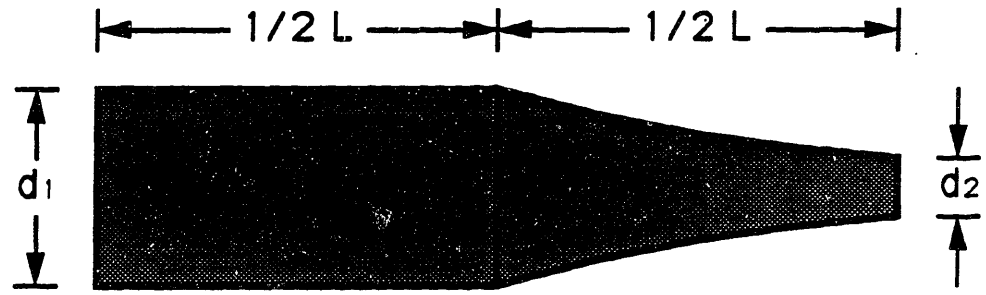

(b) EXPONENTIAL

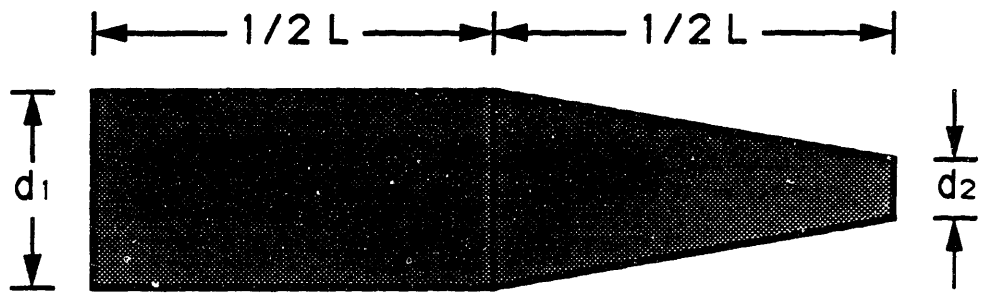

(c) CONICAL

Figure 3-3: Common resonator geometries: (a) stepped, (b) exponential, (c) conical.

the frequencies of interest. Typically, the bandwidth of these devices is limited to a few kilohertz. A more appropriate class of device for frequencies in the ultrasonic range is the piezoelectric transducer (PZT). The response of this element in the ultrasonic region is a strain proportional to the applied voltage. Thus, a PZT of finite thickness will produce a displacement directly proportional to the instantaneous voltage across it. PZT's have good response characteristics at ultrasonic frequencies, provided that the first resonance of the PZT crystal itself lies far above the frequencies of interest. Above this resonance, the response of the PZT rolls off steadily.

The placement of the PZT element along the resonating rod is critical. With conventional electromagnetic actuators, the applied voltage is converted into a driving force. In order to excite the mode of interest, this force should be applied at a point of maximum displacement amplitude (as well as having the correct frequency). PZT's, on the other hand, generate displacements rather than forces. As a result, for maximum modal excitation, the location of the actuator along the rod should be at a point where the displacement amplitude is zero. For proper operation, the PZT's must be precompressed between sections of the resonator. This ensures that the crystals will remain in contact with the resonating structure throughout the compression/rarefaction cycle. Precompression also prevents the PZT's from cracking when operated at high voltages.

3.2.2.3 Transmitter

The transmitter couples the energy of the resonator to the surrounding medium. The efficiency with which the transmission is achieved depends upon the surface area of the transmitting element exposed to the acoustic region of interest. Ideally, the coupling between the resonator and the transmitter should be lossless, and the transmitting element should not affect the resonance frequency of the driver. With these specifications in mind, the most appropriate transmitter would be a thin, infinitely rigid, relatively lightweight circular plate attached to the transmitting end of the resonator. This piston-like element would produce

uniform pressure waves in the vicinity of the symmetric axis of the driver. Near the edge of the transmitter, the planar nature of the standing wave deteriorates. It has been shown that, for good transmission efficiency, the following criterion must be satisfied [2]:

$$a > (0.7)\lambda \tag{3.4}$$

where a represents the radius of the transmitting device, and λ is the wavelength of the acoustic standing wave in air.

From a practical standpoint, realizing this piston-like transmitter is difficult at ultrasonic frequencies. The transmitter itself is subject to deformation when excited by the high frequency mechanical displacements. At sufficiently high frequencies, modal resonances of the plate itself occur, which destroy the uniform displacement distribution of the transmitter. For a circular plate, the frequencies at which these resonances occur are given by [13]:

$$\omega_{ij} = \frac{\lambda_{ij}}{a^2}\sqrt{\frac{Eh^2}{12\rho(1-\nu^2)}} \tag{3.5}$$

where it is assumed that the plate is excited by a point force located at its center. Here, ω_{ij} represents a resonant frequency, and λ_{ij} represents the corresponding eigenvalue. The parameters E, ρ, and ν are the modulus, density and Poisson's ratio of the transmitter material, respectively, and the variables a and h represent the radius and thickness of the plate, respectively. These resonances are axisymmetric and Bessel-shaped in nature. Clearly, in order to keep the resonant modes of the plate above that of the resonator, the transmitter must have a large thickness and a small diameter. However, the increased thickness increases the transmitter's mass (thereby altering the resonance characteristics of the driver), while the decreased diameter reduces its acoustic efficiency.

Rather than designing the transmitter to exhibit piston-like behavior at the operating frequency of the driver, a better design involves matching a particular modal frequency of the transmitting plate to that of the resonator. In this manner, the operating frequency of the driver

remains essentially unchanged. The desired mode corresponds to ω_{01}, an axisymmetric Bessel-shaped mode with a nodal circle of radius approximately equal to one-half of the plate radius. This mode is shown in Fig. 3-4. In this mode, the planar nature of the acoustic pressure waves diminishes at the nodal circle. As a result, the criterion for good transmission efficiency, expressed in Eq. (3.4), relates to the radius of the nodal circle rather than that of the plate itself. Within this nodal circle, the pressure waves are sufficiently planar so that the theory of acoustic levitation presented earlier is sufficiently accurate.

The nature of the vibration of the transmitter is such that the acoustic field generated by the driver is axisymmetric. Furthermore, the particular mode shape chosen creates secondary effects in the acoustic field that exert radial restoring forces on objects suspended in the field. These radial forces drive objects towards the axis of symmetry of the levitator. This favorable effect prevents suspended particles from migrating out of the acoustic region in the presence of disturbances, which would be the case for a perfectly planar acoustic field. Hence, lateral stability can be achieved in the acoustic field.

3.2.3 Description of Driver Hardware

A complete diagram of the baseline acoustic driver is shown in Fig. 3-5. Detailed mechanical drawings of this hardware can be found in Appendix A. The main resonating element consists of two titanium sections held together by a central steel bolt. The steel bolt serves to precompress two PZT crystals which are located between the two sections of the resonator. The titanium transmits longitudinal waves rather well, and resists cracking in the presence of high frequency compression/rarefaction cycles. The lower section is one quarter of the length of the driver, and the upper section is three quarters of the length. The upper part of the upper section is stepped to increase the displacement amplitude at the transmitting end. The diameter ratio across the step is approximately 6 to 1, giving a displacement amplification of 36. The entire resonator acts as the electrical ground for the driver. Electrical continuity is established by the central steel bolt. The overall length of the driver is approximately 8 in.

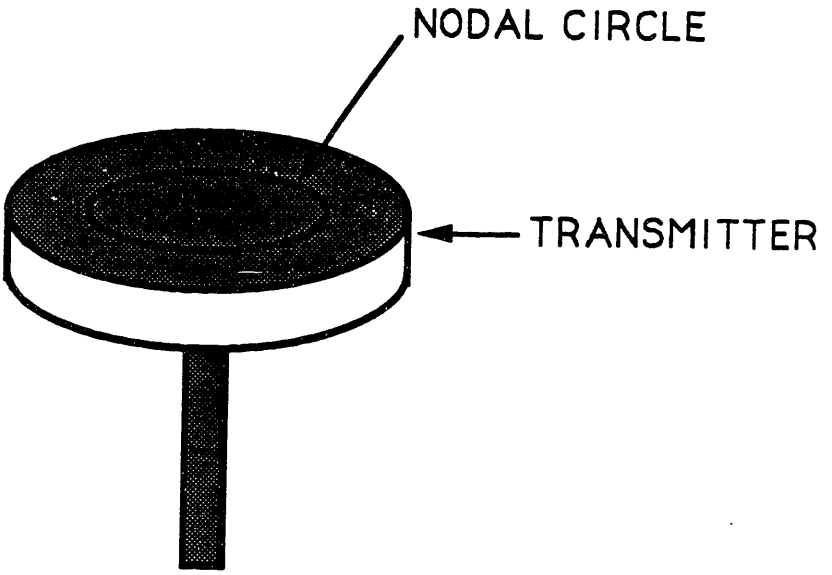

Figure 3-4: Resonating mode of the transmitting plate. Motion of the plate within the nodal circle is in-phase with the motion of the driver and out-of-phase outside of the circle.

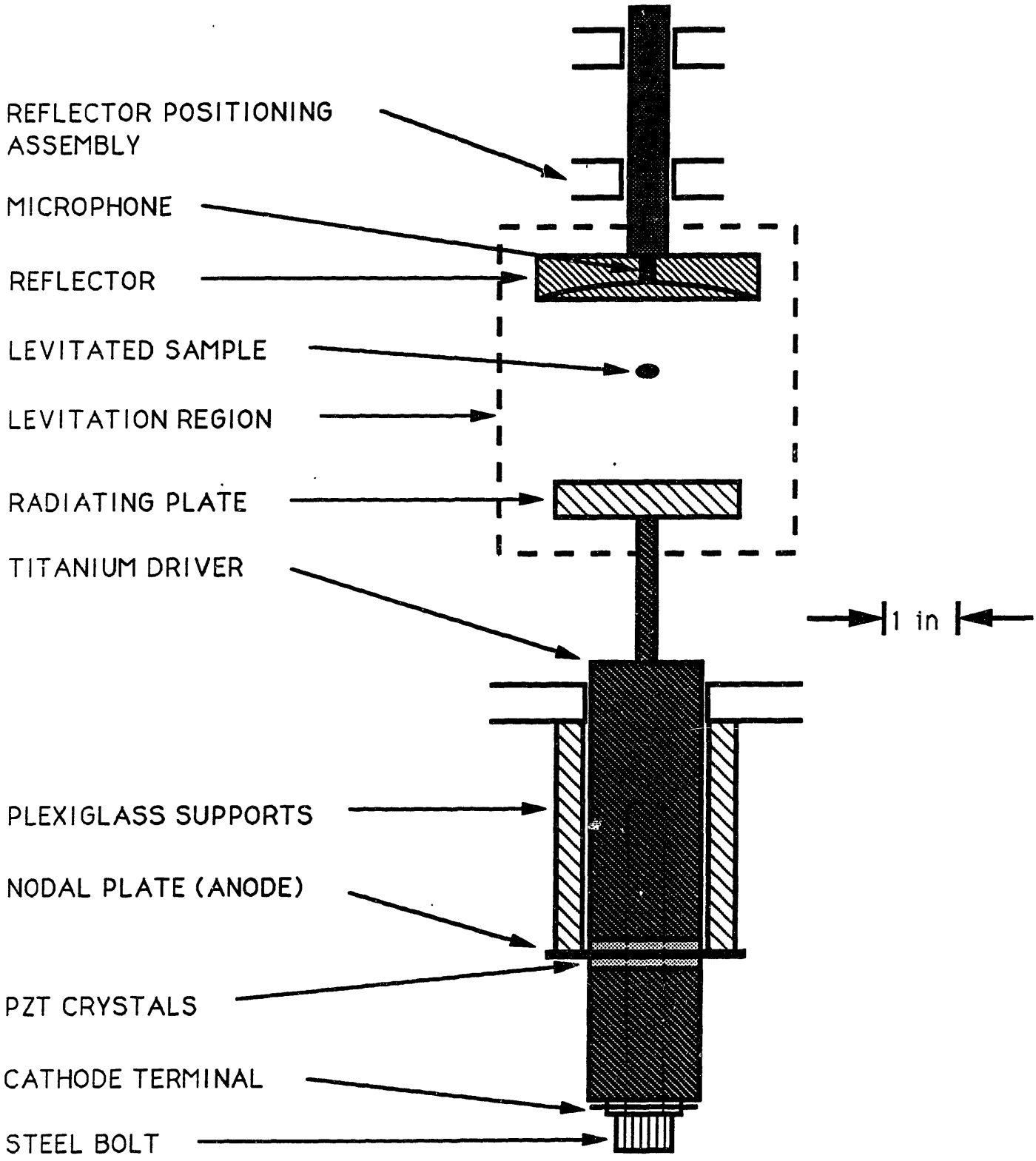

Figure 3-5: Detail of the acoustic levitator hardware.

Between the two sections are two annular PZT actuator crystals. These crystals strain in the direction parallel to the driver axis with a voltage applied across their thickness. The response of the crystals is limited to frequencies below 35 kHz, which is sufficiently far above the operating frequency of the driver. With the resonator vibrating in the second longitudinal mode, displacement nodes are established at the one quarter and three quarter points along the length of the resonator. The PZT crystals are therefore properly placed for driver operation in the second mode. Between the crystals is a steel nodal plate, which acts as the positive terminal for the driver. It is important that this plate is carefully isolated from the titanium sections and other electrical ground points, as the voltage potential at the plate can be quite large. The crystals and the plate are therefore shielded from the central steel bolt by several layers of electrical tape wrapped around the bolt. In addition to providing electrical isolation between the positive terminal and ground, the electrical tape also helps align the crystals and the nodal plate with the titanium sections. The positive terminals of the PZT's face each other, both making contact with the nodal plate. As a result, both crystals expand for a positive applied voltage and contract for a negative applied voltage. This effect is shown in Fig. 3-6.

The central steel bolt is responsible for precompressing the annular PZT crystals, so that the crystals make mechanical contact with both sections of the resonator over the entire compression/ rarefaction cycle. The bolt is torqued to 50 ft-lbs. During the precompression of the PZT's, it is important that the nodal plate is shorted to ground. This dissipates the static charge created within the PZT's during the precompression process. The nodal plate must also be shorted to ground during disassembly of the driver for the same reason.

The nodal plate has a larger diameter than the resonating structure, so that the driver can be supported there. This plate has been found to be the best location from which to support the driver because mechanical vibration is minimized there. By mounting the driver at the nodal plate, the vibrational energy developed in the driver is not transmitted to the support hardware. As a result, almost all energy is imparted to the transmitting plate and the acoustic field. Mounting the driver from a location other than a nodal point not only results in a loss of

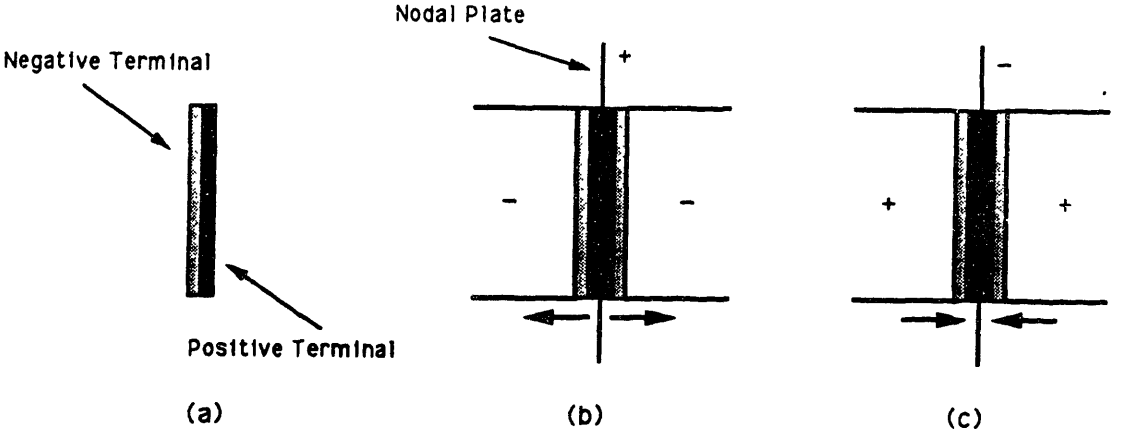

Figure 3-6: Actuation of the driver by PZT crystals: (a) polarity of PZT element, (b) positive applied voltage (PZT's expand), (c) negative applied voltage (PZT's contract).

transmission efficiency, but also has the undesirable effect of inducing vibrational modes in structures that make contact with the support hardware. This can create unwanted noise and vibration near the facility. The supports consist of three rods which are made out of plexiglass to provide insulation between the nodal plate and ground. The attachment point of one of the rods to the nodal plate serves as the positive terminal of the driver.

The end of the resonating assembly is attached to an aluminum transmitting plate. Its dimensions are approximately 2.5 in. in diameter by 0.5 in. thick, giving a primary resonance of about 23 kHz. The plate is held in place by a small section of threaded steel rod. This plate vibrates in the axisymmetric Bessel-shaped mode described in Section 3.2.2.3. It should be noted that the construction process for the transmitter is iterative. That is, the transmitting plate is first machined to the approximate dimensions. It is then mounted to the driver resonator, and the performance of the driver as a whole is evaluated. The dimensions of the transmitting plate are then adjusted in an iterative manner, until optimum performance is achieved. Note that this process is not required if the transmitter is designed to move in a piston-like manner.

The electronic system which controls the acoustic driver consists of an oscillator, amplifier, resonance tracking circuit (described in the next section) and diagnostic equipment. The oscillator provides the sinusoidal excitation voltage to the amplifier. The amplifier supplies the driver with the sinusoidal signal at a sufficiently high voltage level to create the high intensity acoustic field.

3.2.4 Driver Resonance Tracking

The acoustic driver operates at approximately 23 kHz, which is above the range of human hearing. This corresponds to an acoustic wavelength of about 1.5 cm and an acoustic wave number of approximately 4.0 cm^{-1}. The resonance characteristics of the driver are determined by observing the current that flows through the driver PZT's. At resonance, the amplitude of this signal is maximized, and it is in phase with the excitation voltage applied across the terminals of the driver. For small deviations between the frequency of the excitation

and the resonance of the driver, the amplitude of the current signal is diminished, and its phase with respect to the phase of the excitation voltage is nonzero. These effects are shown in Fig. 3-7, where the amplitude and relative phase of the current signal are plotted against the excitation frequency. The figure indicates that the driver resonance width is approximately 12 Hz. At resonance, the impedance of the driver is approximately 150 Ω.

It is important that the frequency of the excitation voltage delivered to the driver correspond precisely to the frequency of the driver resonance. Fig. 3-7 suggests that a discrepency as small as 5 Hz (less than 0.025 % of the operating frequency) results in a significant reduction in power delivered to the driver and, consequently, a weaker acoustic field. It is anticipated that several effects cause the resonance to shift, making it necessary to actively control the excitation frequency. The primary effect on the resonance frequency of the driver is drift due to thermal effects. Changes in the temperature of the resonating and transmitting elements, caused by small amounts of viscous dissipation of mechanical energy into heat as well as fluctuations in the ambient conditions, alter the speed of propagation of compression waves through these media. This shifts the resonances of these elements, making it necessary to adjust the excitation frequency slightly. As a result, some method is required to monitor the relationship between driver resonance and excitation frequency.

The relative phase shift of the current signal provides a good measure of the accuracy with which the excitation frequency tracks the resonance of the driver. At resonance, the relative phase shift is zero. It becomes nonzero if the excitation frequency does not quite correspond to the resonance frequency of the driver. Moreover, the direction of the phase shift depends on whether the excitation frequency is too high or too low. Consequently, the phase error between the voltage and current signals indicates how the excitation frequency should be adjusted in order to maintain resonance.

A phase-locked loop, shown in Fig. 3-8, utilizes this phase error signal to automatically control the excitation frequency. The controller monitors the relative phase shift between the voltage applied to the driver and the current through it. In the presence of resonance shifting,

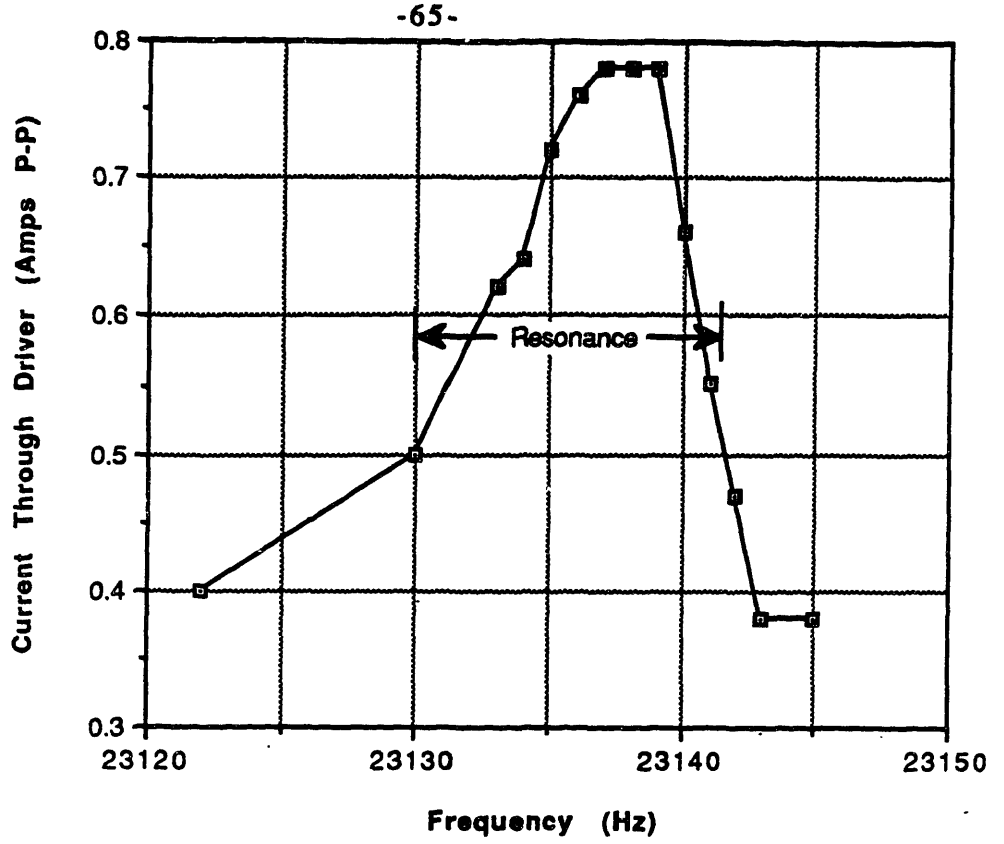

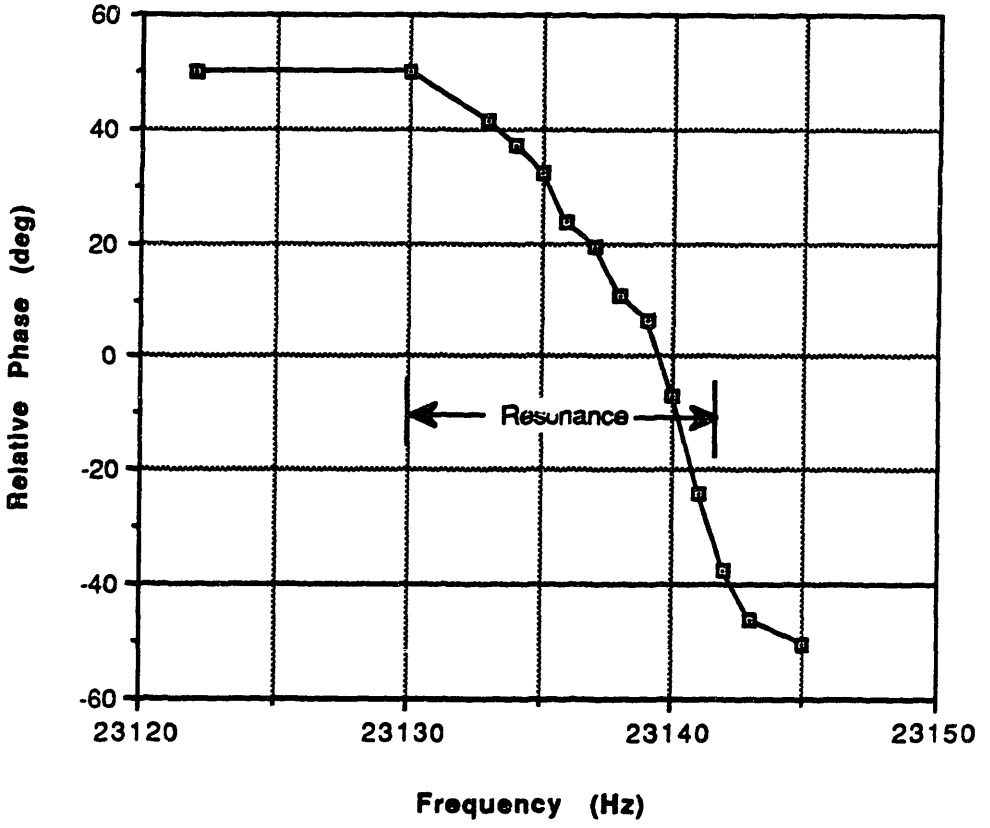

Figure 3-7: Acoustic driver amplitude and phase response near resonance. The sharp resonance is apparent. The voltage applied to the driver is approximately 120 V peak-to-peak.

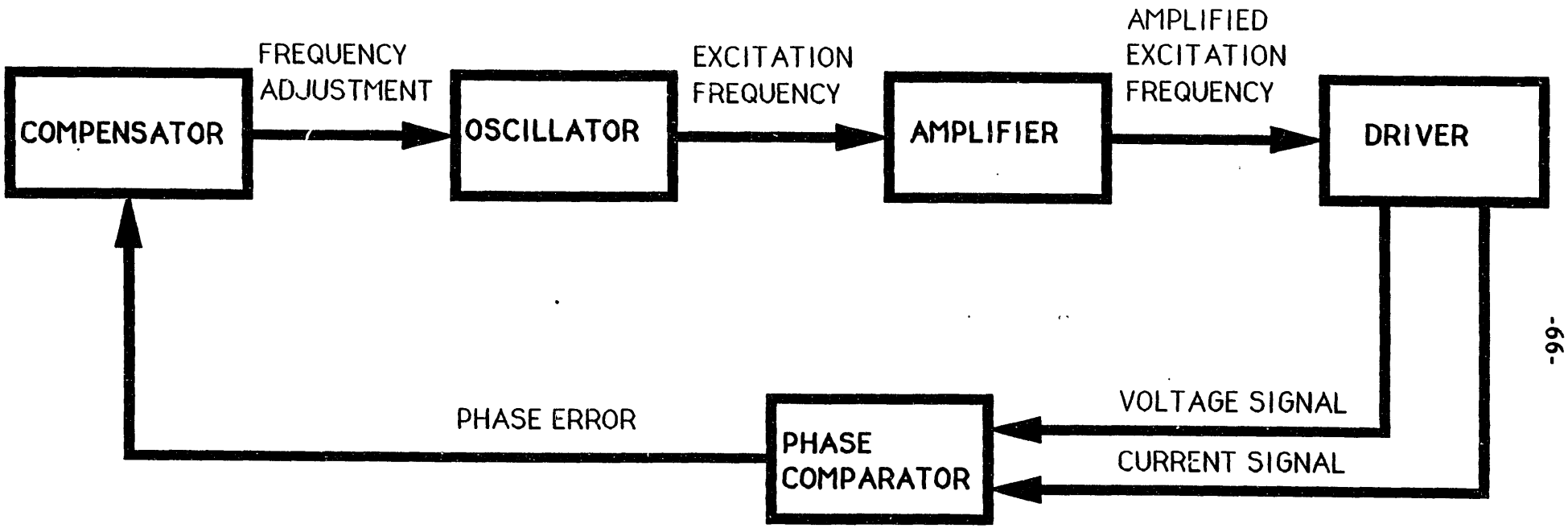

Figure 3-8: Driver resonance tracking system. The ability to achieve precise control of the oscillator frequency makes resonance tracking possible.

the phase error signal is used to adjust the frequency of the excitation signal. In this way, resonance is maintained automatically. A detailed summary of the operation of the phase-locked loop system is presented in Appendix B.

3.3 Reflector Assembly

The design of the reflector is based on the need to focus the acoustic field to a region close to the axis of the acoustic driver. As a result, a slightly concave reflector is desired in lieu of a flat plate. Ideally, the reflector should be perfectly smooth and rigid, so that approaching acoustic pressure waves are reflected entirely. The curvature is such that the reflector does not destroy the essentially planar nature of the field, yet focuses the majority of the acoustic energy to a region bounded by the perimeter of the transmitting plate. Consequently, the radius of curvature should be on the order of the maximum driver-reflector separation. This curvature also plays a role is establishing the secondary radial restoring forces which direct suspended samples towards the axis of the driver.

It is also important that the driver-reflector separation be controllable, so that the required separation for the acoustic standing wave can be achieved precisely. The required driver-reflector separation is given by

$$d = \frac{nc}{2f} \tag{3.6}$$

where n is the number of nodal planes in the acoustic field, c is the speed of sound in air, and f is the operating frequency of the driver. This relation can be expressed in terms of the temperature within the acoustic region, yielding

$$d = \frac{n}{2f}\sqrt{\gamma RT} \tag{3.7}$$

where γ and R are the specific heat ratio and gas constant for air, respectively. In the presence of thermal gradients and shifting of the operating frequency of the driver, the required separation distance will change according to

$$\frac{\delta d}{d} = \frac{1}{2}\frac{\delta T}{T} - \frac{\delta f}{f} \tag{3.8}$$

The amount by which the actual separation distance can deviate from the required value for a particular set of operating conditions without appreciable loss in acoustic field strength is inversely related to the sharpness of the resonance achieved in the acoustic region. Consequently, a positioning mechanism for the reflector is required, particularly in cases where the experiments conducted involve large temperature fluctuations in the acoustic region (e.g., experiments involving phase change phenomena). Additionally, some means must be provided to monitor the status of the standing wave in the presence of deviations in these operating conditions. A microphone mounted within the acoustic field performs this function. The information from the microphone determines the motion of the reflector required to maintain the standing wave.

In Fig. 3-9, a detail of the reflector assembly is presented. The reflector itself is made of aluminum, and the surface exposed to the acoustic field is polished. A small hole is drilled through the center of the reflector, in which is mounted a small microphone. The microphone monitors the status of the standing wave by converting the acoustic pressure at the reflector surface into an electrical signal and is used to maintain the correct driver/reflector separation. By mounting this device flush with the surface of the reflector, its effect on the acoustic field is minimized. The reflector position is adjusted by a small electric motor. In order to monitor the position of the reflector, a potentiometer is coupled to the motor. The reflector position is thus represented as an electrical signal.

The frequency of the microphone signal corresponds to that of the excitation voltage applied to the driver, but the signal is not sinusoidal. The intensity of the acoustic field saturates the microphone, and the resulting signal is (approximately) a square wave for all separation distances. The amplitude of this signal is therefore constant, independent of the driver/reflector separation. However, the phase of this signal, relative to the excitation voltage,

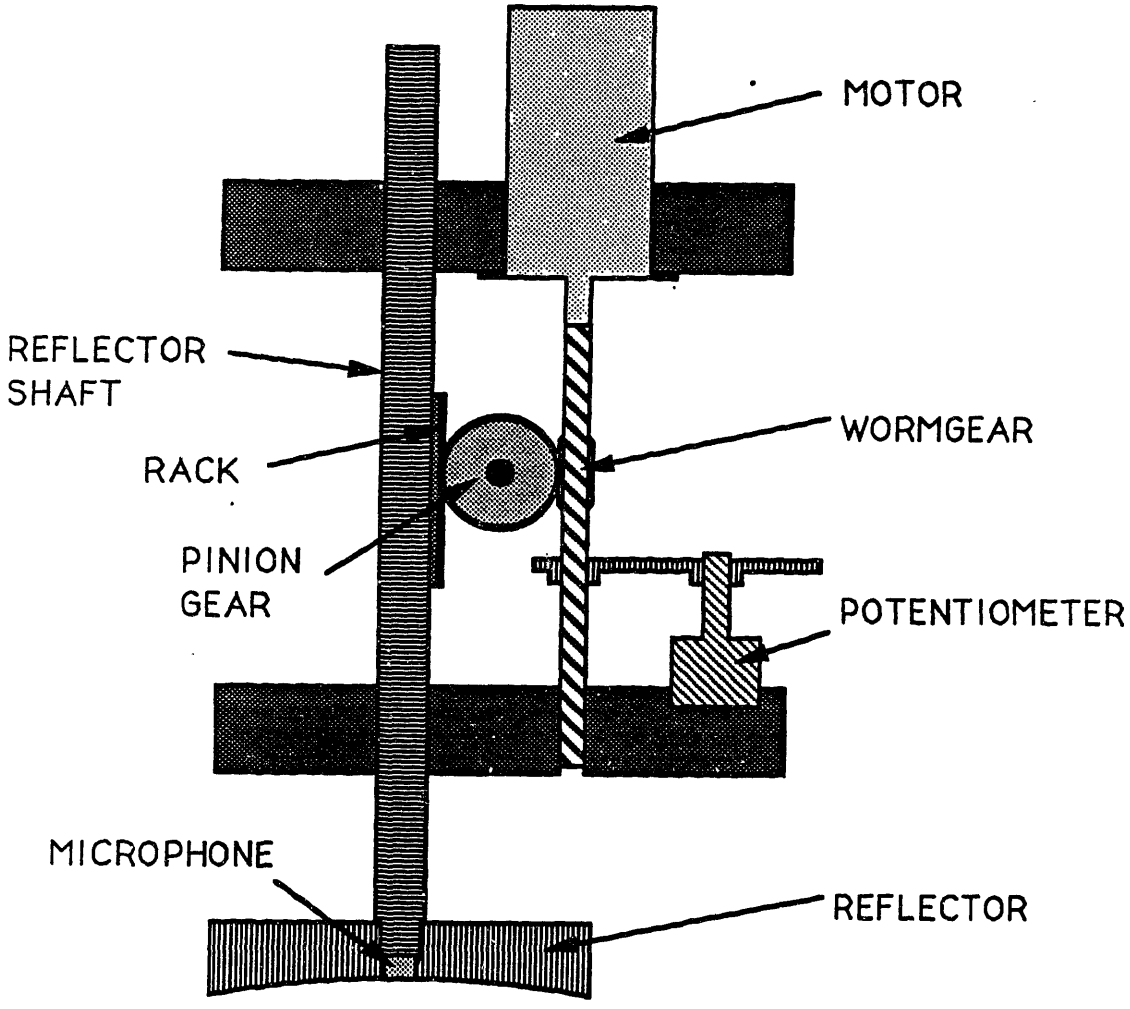

Figure 3-9: Detail of the reflector assembly.

shifts dramatically as the reflector is moved through a resonance. In Fig. 3-10, the relative phase of the microphone signal is plotted against the deviation in position of the reflector from resonance. The graph suggests that the position of the reflector must be controlled to within 0.5 mm in order to maintain the acoustic standing wave. Accordingly, the reflector assembly and positioning mechanism is designed to achieved this accuracy.

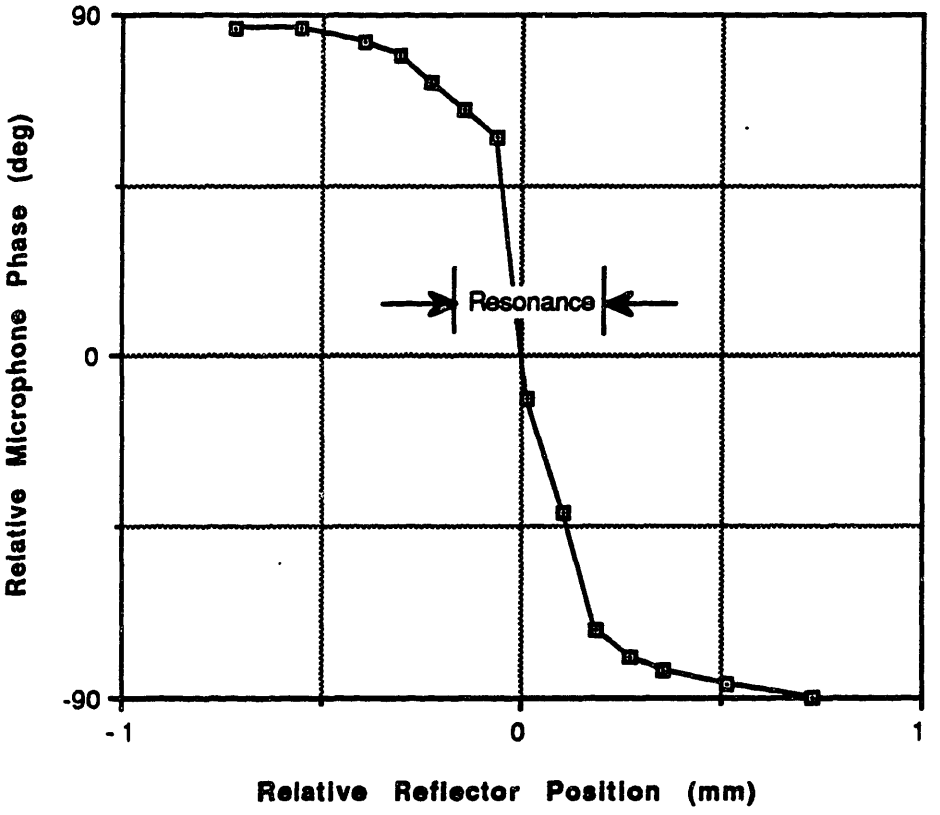

Figure 3-10: Response of the microphone as the driver/reflector seperation distance is adjusted. The microphone is saturated by the intense acoustic field, even when the seperation distance does not correspond to a resonance. The magnitude of the microphone signal is therefore constant for all seperation distances, and only the relative phase of this signal is shown here.

Chapter 4
Description of Acoustic Levitation Facilities

4.1 Overview

The development of two separate levitation facilities was motivated by the wide range of ambient conditions anticipated during cloud physics experiments. From the point of view of simulating these conditions, the most important specification is the presence or absence of a flow field around the hydrometeor. Rather than design one facility capable of simulating both types of environments, it was more practical to develop two specialized facilities. The Vertical Facility utilizes a strong acoustic field to suspend samples against the force of gravity without creating any type of ambient flow. The Ventilated Facility, on the other hand, utilizes a wind tunnel to simulate the ambient flow field of a free falling hydrometeor, and relies on an acoustic field to maintain positional stability of the sample within the test section. Both facilities are presented here, followed by a description of some of the diagnostic equipment available for use in either facility.

4.2 Vertical Facility

4.2.1 Description of the Vertical Facility

The Vertical Facility is shown in Fig. 4-1. In this facility, a strong acoustic field suspends samples against the force of gravity. The acoustic levitator is vertically oriented, with the axis of symmetry of the driver and reflector directed parallel to the gravitational field. Stable equilibrium locations for suspended samples are therefore slightly below the nodal planes of the acoustic field, as described in Sec. 2.2.2.2. The reflector curvature, in conjunction with the modal pattern generated by the transmitting plate, focuses the acoustic field so that stability in the horizontal plane is achieved. Samples are, therefore, directed

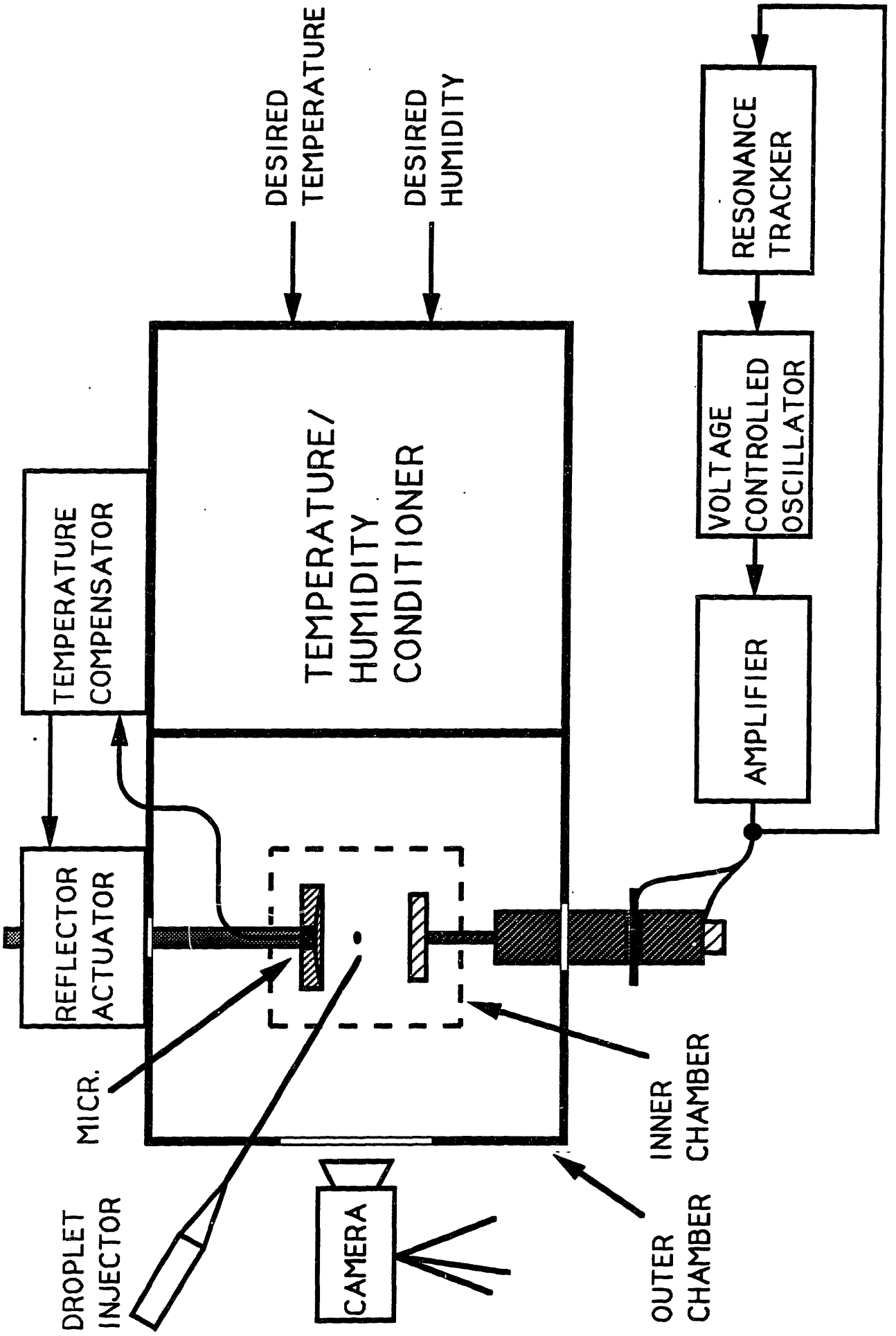

Figure 4-1: Overall schematic diagram of the Vertical Facility (not to scale).

towards the driver axis. Resonance tracking is achieved with the phase-locked loop described in Sec. 3.2.4.

The entire levitator assembly is contained within an environmental chamber (Standard Environmental Systems - model RTT/5S) capable of adjusting and maintaining a desired temperature and humidity. The chamber can maintain a desired temperature between -50 degrees C and 200 degrees C to within approximately 2 degree accuracy. The relative humidity is adjustable from almost 0 % to 100 %, and can be maintained to within 5% accuracy. The chamber is approximately 14" wide by 16" tall by 26" deep, with insulation to minimize heat transfer to and from the chamber. Refrigeration evaporators and heating coils are introduced from the back of the chamber. The acoustic levitation hardware is introduced through portals in the top and bottom walls of the chamber. A strong fan circulates the conditioned air in the chamber to ensure that the ambient conditions throughout the chamber are reasonably uniform. In order to prevent the ambient flow field from perturbing the suspended object, a removable cylindrical plexiglass shield of 5" diameter encloses the levitator. The walls of this inner chamber are thin (approximately 0.25 in.), and the temperature inside is affected primarily by conduction across these walls. A set of small holes at the top and bottom of the shield creates a small flow between the chambers, which reduces the time lag associated with modifying the temperature in the inner chamber. The front wall of the outer chamber has a glass window, which allows access to photographic equipment. Also, a small portal in the side wall facilitates the introduction of instruments into the test section.

In Fig. 4-2, the temperature within the test section of the Vertical Facility is plotted against time to demonstrate the time lag associated with the conduction of heat across the walls of the inner chamber. The test section is initially at room temperature, and the environmental system is commanded to establish a temperature of -20 degrees Celsius in the chamber. From the figure, the time constant is approximately 15 minutes.

If direct access to the droplet (e.g., physical contact, closeup photography) is required, the cylindrical plexiglass shield can be removed. Samples levitated in the Vertical Facility

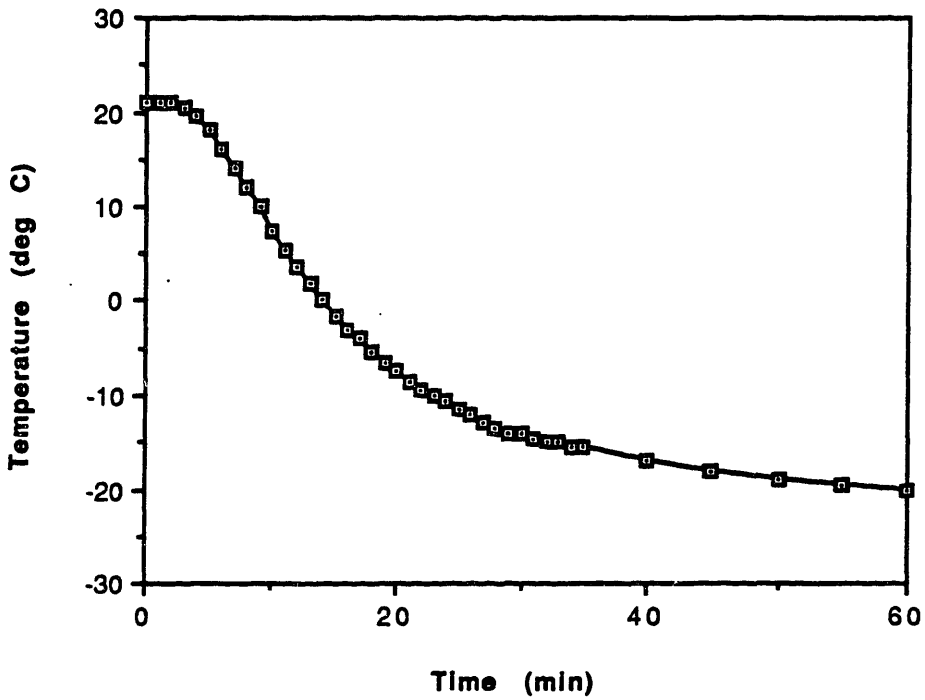

Figure 4-2: Temperature within the test section of the Vertical Facility for an initial temperature of 22 deg. C and a commanded temperature of -20 deg. C. The time constant associated with the heat transfer across the walls of the chamber is approximately 15 min.

under these conditions experienced slight excursions in the horizontal plane of less than 2 mm from the central equilibrium point. These motions were caused, primarily, by ambient flow disturbances. The excursions were periodic in nature, with a period of approximately one second, corresponding to a maximum velocity of 0.013 m/sec in the horizontal plane. The periodicity of the motion is indicative of the secondary restoring forces present in the acoustic field, which are responsible for stabilizing the samples in the horizontal plane. With the plexiglass shield in place within the environmental chamber, the motion of levitated samples was effectively eliminated, as the air within the test section was shielded from ambient flow disturbances. Photographs of liquid samples levitated in the Vertical Facility are shown in Fig. 4-3. Also shown in this figure is the coalescence of a spray of small droplets introduced into the acoustic field. The acoustic field confines the spray to the nodal planes and the droplets migrate toward the driver axis, where coalescence takes place.

4.2.2 Temperature Compensation System

In the presence of the large temperature deviations associated with certain cloud physics experiments (e.g., phase change phenomena), the speed of propagation of pressure waves in the air will deviate significantly from the corresponding value at room temperature, as described in Sec. 3.3. This implies that the wavelength of the standing wave changes for a given frequency, since the wavelength is directly proportional to the propagation speed. The required driver-reflector separation distance for standing wave resonance is therefore affected by temperature fluctuations. As a result, it is necessary to provide some sort of temperature compensation to maintain the acoustic standing wave.

The approach used in the Vertical Facility is a closed loop system, shown in Fig. 4-4. Here, the state of the standing wave is monitored by a microphone mounted at the surface of the reflector. As explained in Section 3.3, the phase of the microphone signal shifts considerably in relation to the phase of the excitation sinusoid delivered to the driver when the driver/reflector separation passes through a resonant spacing. By comparing the phases of

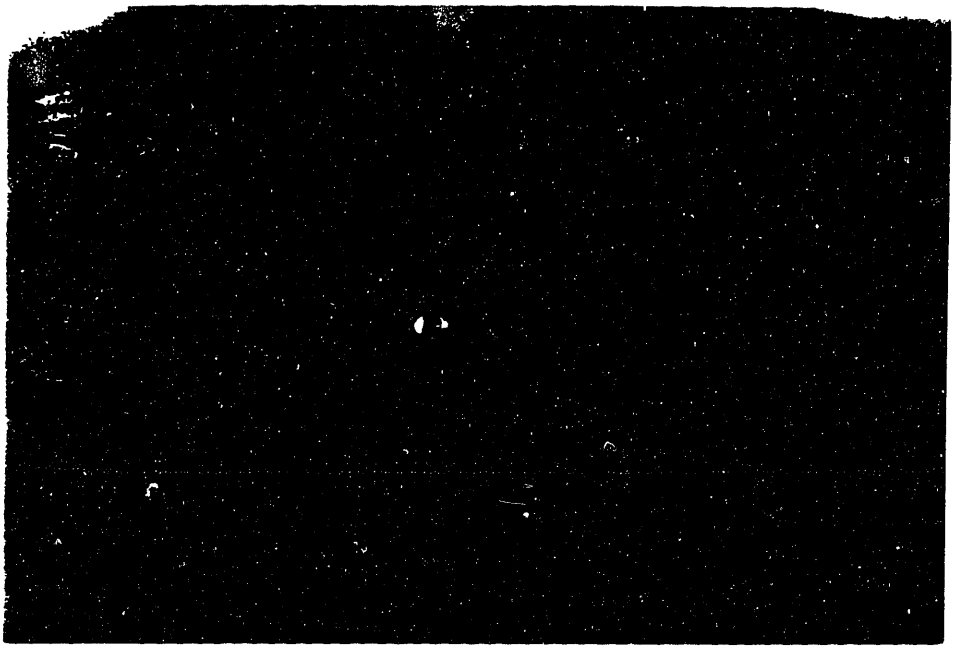

(a)

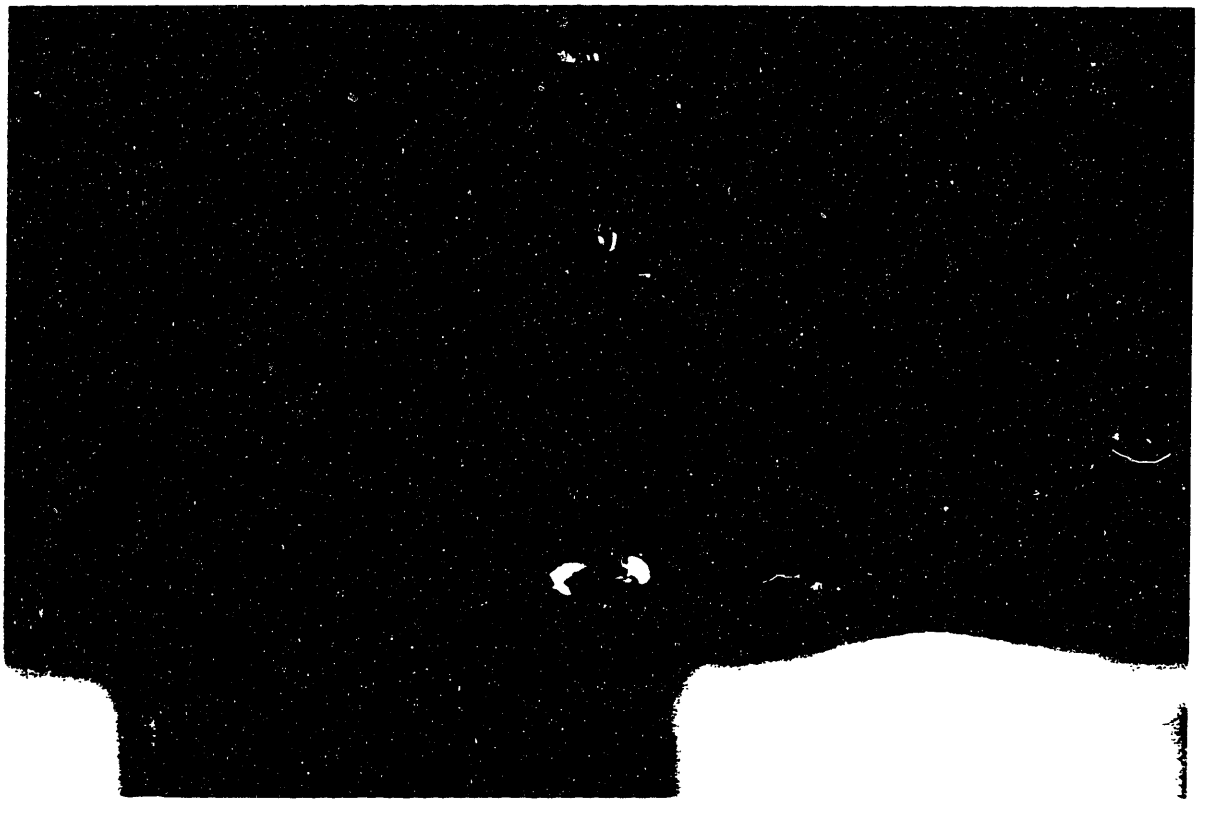

(b)

Figure 4-3: Photographs of samples suspended in the Vertical Facility: (a) single water droplet (2 mm diameter), (b) water droplets coalescing along the nodal planes of the standing wave after a fine mist is sprayed into the acoustic region.

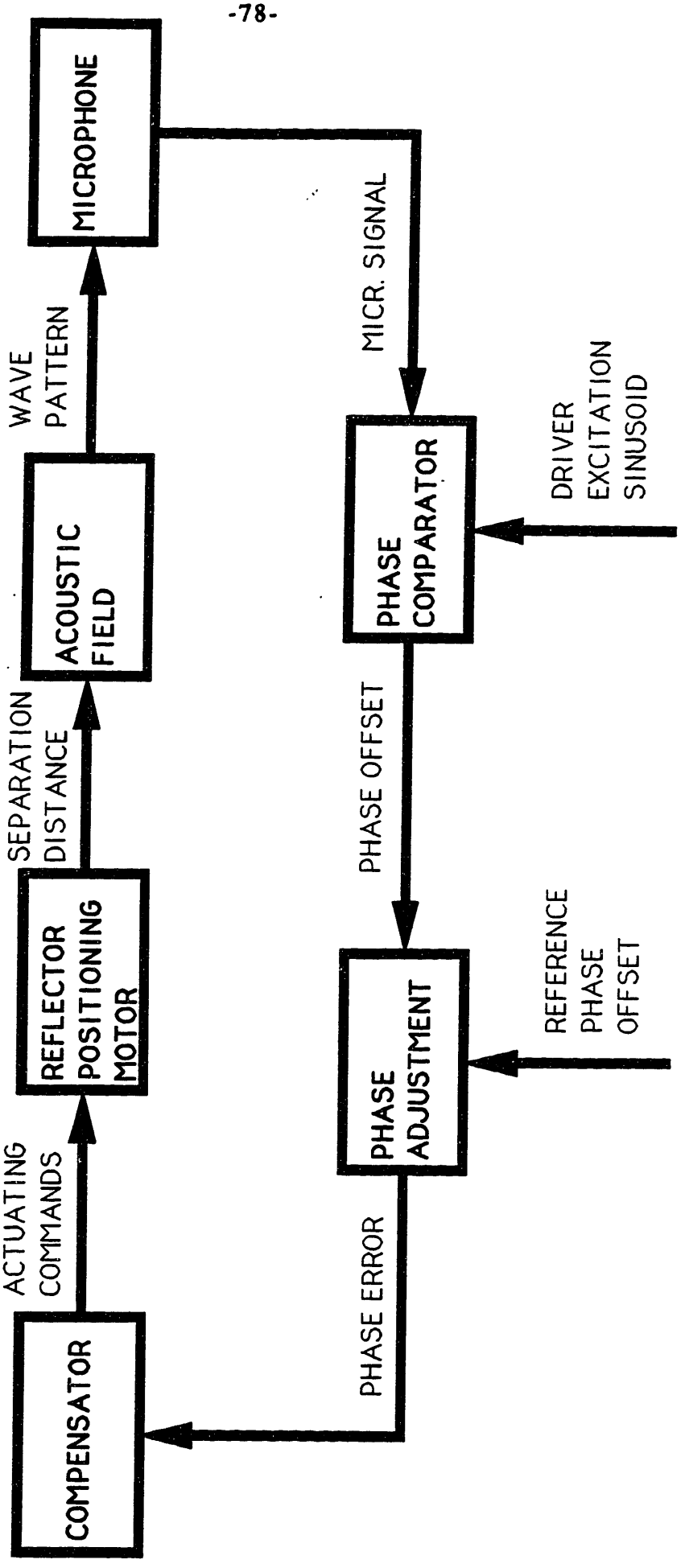

Figure 4-4: Temperature compensation system. The phase of the microphone signal determines the adjustment required to maintain the standing wave.

these signals, a phase offset signal is generated. The phase offset is then compared to a reference offset (determined experimentally) which corresponds to acoustic resonance, and an error signal is formed. The compensator uses this error signal to drive the reflector positioning mechanism, so that the required separation is maintained. By responding to the acoustic field itself, the microphone signal takes into account the net effect of the temperature distribution throughout the entire acoustic region. As a result, the signal relates directly to the status of the standing wave. Also, an absolute measurement of the driver-reflector separation distance is not required. Rather, the polarity of the phase offset signal determines the direction of required reflector position actuation, and its magnitude determines the duration of this motion. As a result, the only sensor employed is the microphone, which, by virtue of its location, does not affect the standing wave significantly. These features make the closed loop system favorable to an open loop approach, where the required separation distance is determined from a measurement of the temperature in the acoustic region and an absolute measurement of the actual driver/reflector separation is required.

In order to test the temperature compensating system, the temperature within the test section was cycled several times with the acoustic levitator operating and the compensator active. The position of the reflector, established by the compensator, was observed as a function of temperature. During the temperature cycling, a small sphere was suspended in the acoustic field to ensure that the standing wave was maintained throughout the cycle. The results, plotted in Fig. 4-5, show good agreement between the reflector position established by the compensator and the position predicted by the theory. This indicates that the phase of the microphone signal is indeed related to the error between the actual separation distance and the distance required for resonance.

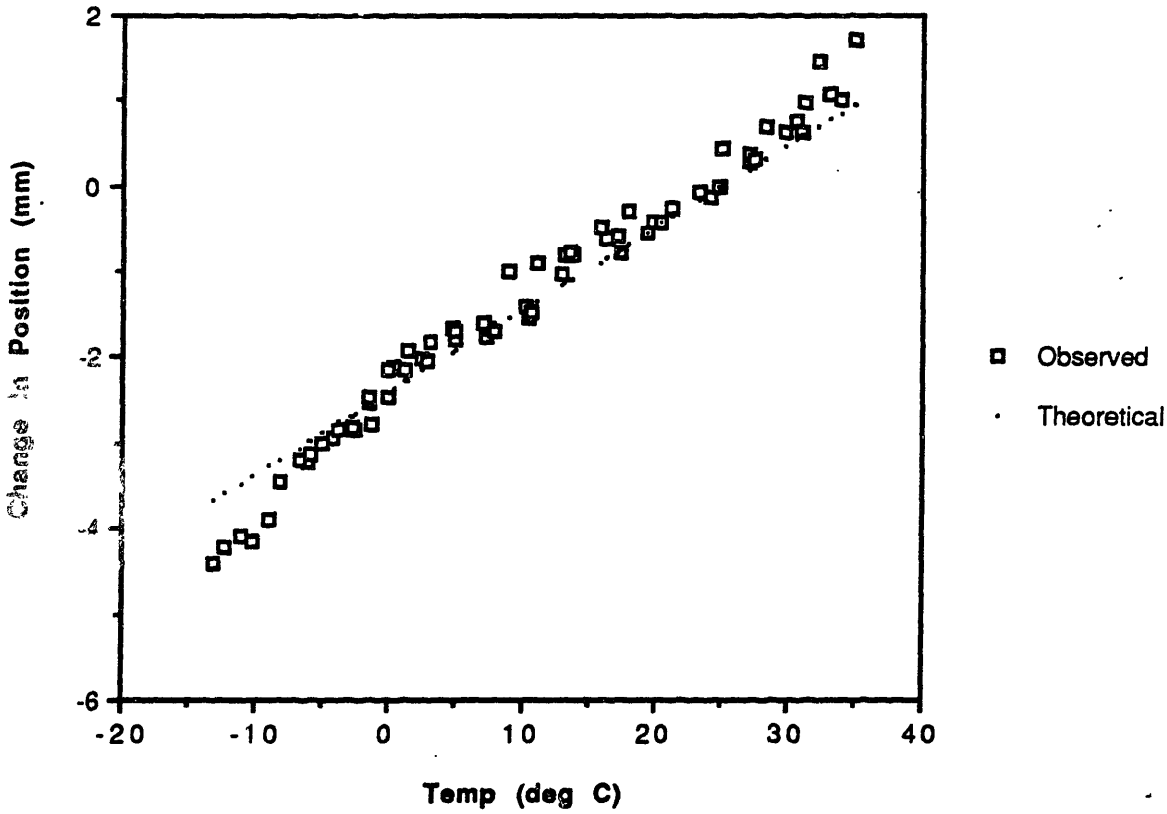

Figure 4-5: Relationship between the temperature of test section and the change in position of the reflector. The temperature compensator successfully adjusts the driver/reflector seperation in the presence of large temperature deviations.

4.3 Ventilated Facility

4.3.1 Principle of Operation

The Ventilated Facility achieves the force necessary for levitation against gravity with a small vertical wind tunnel. With the speed of the tunnel set at the terminal velocity of the suspended object, the aerodynamic and gravitational forces on the object just cancel. This creates a flow field around the suspended sample similar to the flow around a free falling hydrometeor. The driver and reflector are aligned with their axes of symmetry perpendicular to the flow. The purpose of the acoustic field in this case is to stabilize the position of the object. This is necessary for two reasons. First, the actual flow speed in the test section of the tunnel will most likely deviate from the exact terminal velocity of the object, causing it to migrate upstream or downstream. Other tunnels have been built [14] that circumvent this problem by tailoring the flow speed along the test section. This is achieved by diverging the flow slightly, so that the velocity downstream (above the droplet) is somewhat less than the velocity upstream (below the droplet). The suspended object migrates towards a location where the proper flow velocity exists (i.e., the weight of the object equals the drag on it), and vertical stability is achieved. However, turbulence levels in these tunnels must be held at extremely low levels for this approach to succeed, since the velocity profile of the flow must be well-behaved and predictable. The other consideration that warrants the use of the acoustic stabilizing field is horizontal stability. Because the flow entering the test section is divergent, a stable horizontal location for the suspended object does not exist. This problem is much more difficult to solve in conventional wind tunnels, and usually requires placing a flow shaping obstacle upstream of the test section. The velocity profile in the test section then exhibits radial dependance, and a stable equilibrium for the suspended object exists directly downstream of the obstacle. However, this approach significantly increases the turbulence levels in the tunnel, and is not very effective for large objects.

The stabilizing effect of the acoustic field in both horizontal and vertical directions is shown in Fig. 4-6. In the Ventilated Facility, the driver axis lies in the horizontal plane, perpendicular to the flow. As a result, the nodal planes of the acoustic field are vertically oriented. Objects suspended in the flow field are therefore confined to these nodal planes. Clearly, this creates stability along only one axis in the horizontal plane. A second horizontally oriented driver/reflector pair can be placed perpendicular to the first for stability along the second horizontal axis. Objects would then be confined to vertical lines corresponding to the intersections of the two sets of orthogonal nodal planes. While this approach is straightforward, it requires two sets of acoustic levitator hardware and associated electronics. A simpler approach takes advantage of the secondary effects of the acoustic field from a single driver. With an appropriately curved reflector, the acoustic field generated by the driver exerts secondary forces on suspended objects towards the driver axis (Section 3.3). Therefore, some stability is achieved along the horizontal axis perpendicular to the driver axis. Of course, the restoring force in this direction is not as strong as the primary acoustic force directed along the axis of the driver.

This secondary radial restoring force is also responsible for creating vertical stability in the Ventilated Facility. For example, if the tunnel flow speed in the test section is greater than the terminal velocity of the object, the object will move downstream. However, as it moves in this direction, the secondary acoustic force (which is directed upstream above the driver axis) increases. Eventually, a point is reached where the sum of the acoustic and gravitational forces will just cancel the aerodynamic force. A similar phenomenon will occur if the tunnel speed is less than the terminal velocity. Therefore, provided that the tunnel speed is sufficiently near the terminal velocity, vertical stability can be maintained.

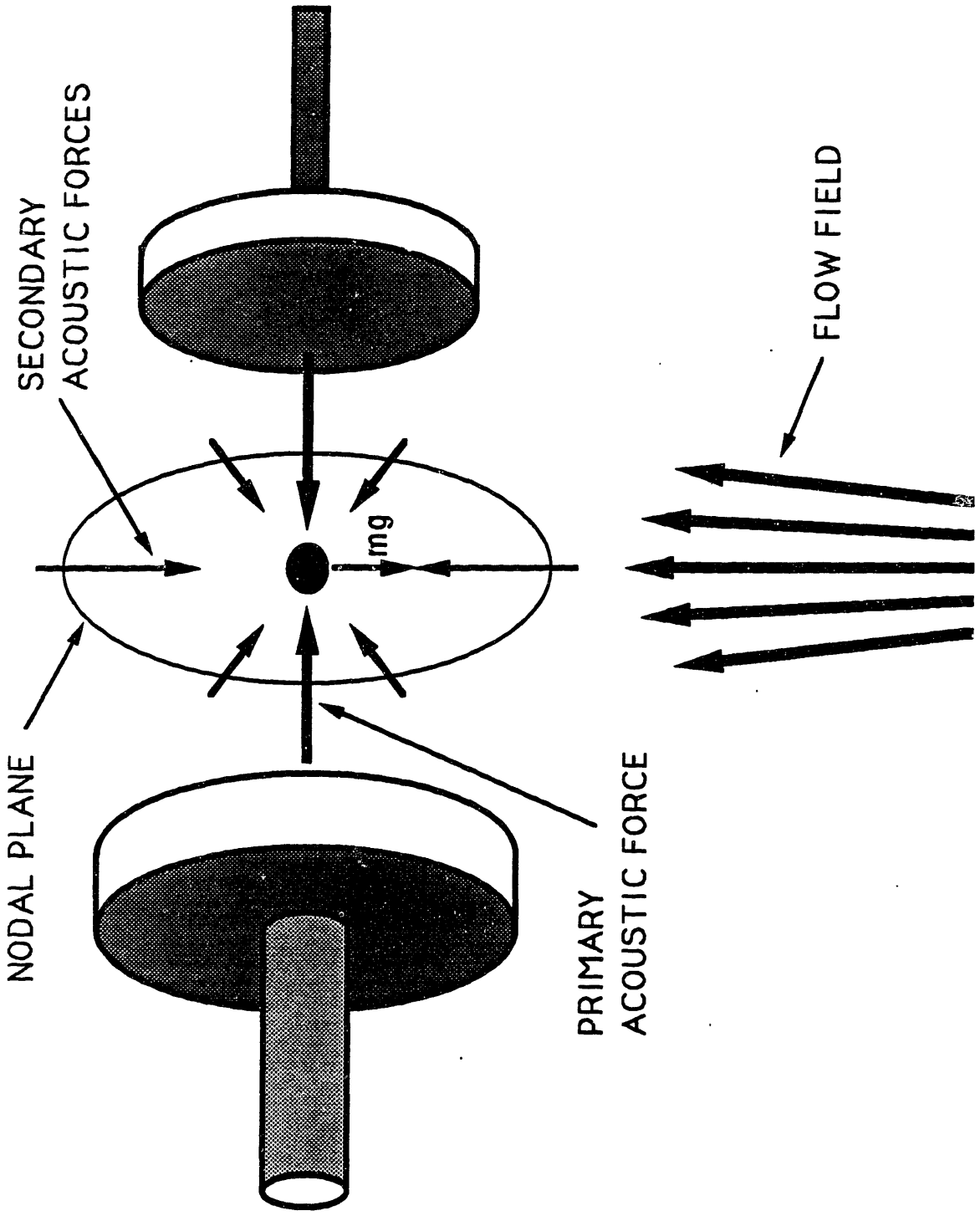

Figure 4-6: Acoustic stabilization of a suspended sample in the Ventilated Facility. The primary acoustic force confines the object to a nodal plane. The secondary forces position the sample in the horizontal plane to a point directly above the center of the flow. These forces also compensate for discrepencies between the weight of the object and the aerodynamic drag on it.

4.3.2 Description of the Ventilated Facility

The Ventilated Facility, shown in Fig. 4-7, consists of a vertical wind tunnel, a refrigeration unit, a single acoustic levitator with the associated control electronics, and droplet injector. The dimensions of the facility are approximately 56" wide by 69" tall. Due to the stabilizing forces arising from the acoustic field, the precision with which the wind tunnel flow speed must be controlled is not as critical as would be the case for a conventional vertical wind tunnel. Consequently, the design of the wind tunnel is less constrained. Most importantly, a closed tunnel can be employed. This facilitates temperature and humidity control in the test section, as the air is recycled continuously. Furthermore, trace gases concentrations can be maintained more easily with a closed tunnel. The refrigeration system is conventional, and is described in Appendix C, while the wind tunnel, test section and droplet injector are discussed below.

4.3.2.1 Wind Tunnel

The wind tunnel for the Ventilated Facility is shown schematically in Fig. 4-8. The tunnel design is not as constrained as would be the case for a conventional vertical wind tunnel, due to the stabilization provided by the acoustic field. The maximum speed for the tunnel is 10.5 meters per second, which exceeds the terminal velocity of the largest stable water droplet at sea level. The main components are the fan assembly, the plenum and heat exchangers, the low turbulence vertical segment, and the return channel. The inner walls of all elements of the tunnel are coated with waterproofing finish to avoid excessive water absorption during humid operating conditions. Also, foam insulation surrounds the outer walls of all sections, thereby minimizing heat transfer to the ambient surroundings.

The fan for the tunnel is eight inches in diameter and accelerates the return air from the test section into the plenum. It is belt driven by an electric motor. The motor lies outside of the tunnel to protect it from the potentially harmful conditions (humidity, extreme temperatures, etc.) associated with the airflow. This configuration also prevents heat generated by the motor

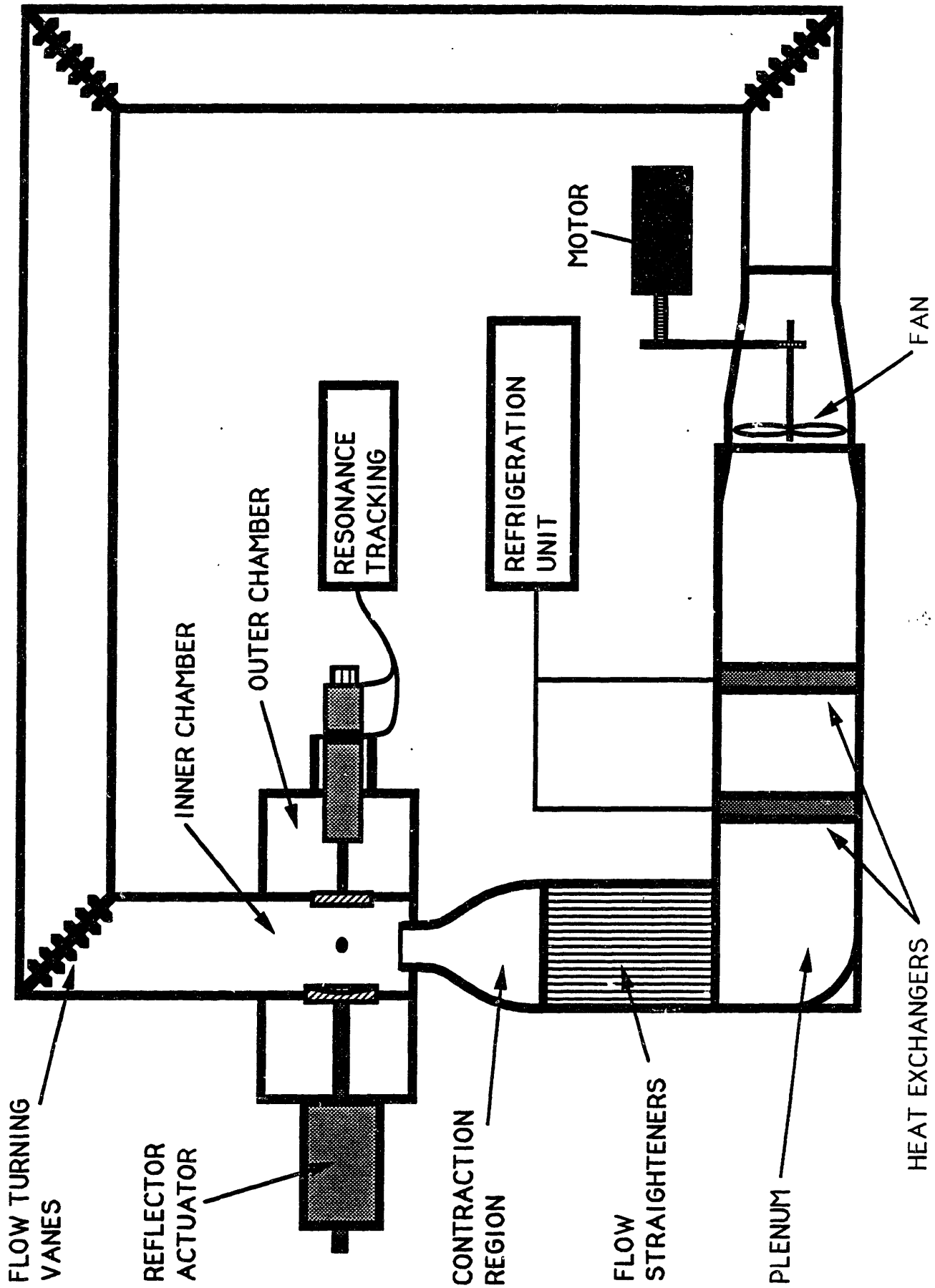

Figure 4-7: Overall schematic diagram of the Ventilated Facility (not to scale).

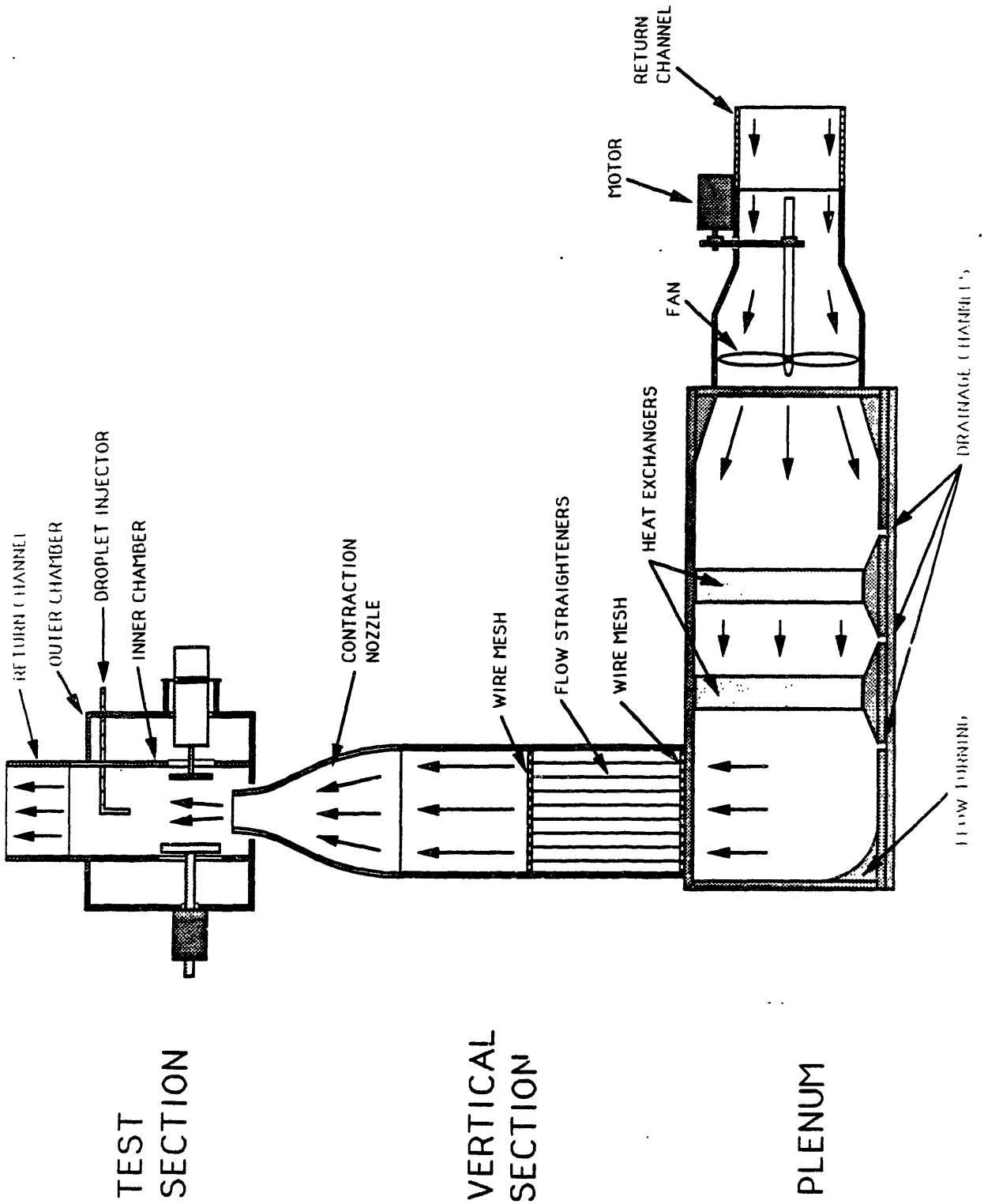

Figure 4-8: Detail of the wind tunnel.

from being absorbed by the conditioned airflow. The motor chosen is a variable speed DC unit with excellent voltage to speed linearity. A heavy duty rheostat controls the speed of the tunnel.

The plenum settles the air emerging from the fan, allowing it to equilibrate before entering the vertical section of the tunnel. It is constructed from plywood and measures 30" long by 12" wide by 12" deep. A small diffusing section slows down the incoming air. At this point, the velocity of the airflow is minimized. Consequently, the heat exchangers are located across the plenum, so that maximum heat transfer is achieved. The fins on the heat exchangers also serve to straighten the flow to some degree. Drainage channels are located on either side of the heat exchangers for de-icing purposes.

From the plenum, the airflow is turned in the vertical direction. The cylindrical vertical section of the tunnel is 8" in diameter and contains a set of flow straightening tubes bounded above and below by wire mesh. After passing through these elements, the turbulence in the airflow is minimized. The contraction nozzle then accelerates the flow into the test section. The nozzle has an area ratio of 16 to 1, and creates a laminar flow profile across its outlet. Because the facility can tolerate a small level of turbulence (due to the stabilization arising from the acoustic field), the exact nozzle geometry is not critical. The outlet of the nozzle is two inches in diameter and approximately two inches below the test section, and the flow remains essentially laminar throughout the acoustic region.

The return channel redirects the flow emerging from the test section back to the fan. It is composed of four sections of PVC tubing of 6 1/2" diameter circular cross section. At each corner, plexiglass flow turning vanes are installed to reduce upstream turbulence. These sections are heavily insulated, as a large amount of surface area comes in contact with the airstream.

The wind tunnel is capable of maintaining a stable, laminar flow at the test section, as shown in Fig. 4-9. The relationship between the voltage applied to the motor and the flow speed at the test section is extremely linear, primarily due to the linearity of the speed of the

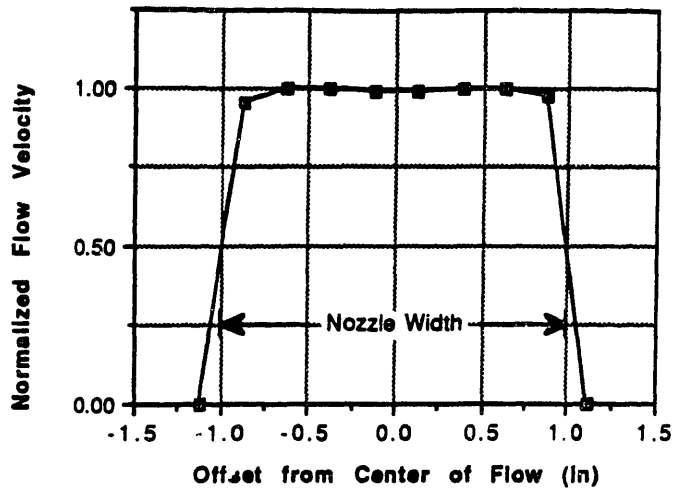

(a) 2 INCHES ABOVE NOZZLE (TEST SECTION LOCATION)

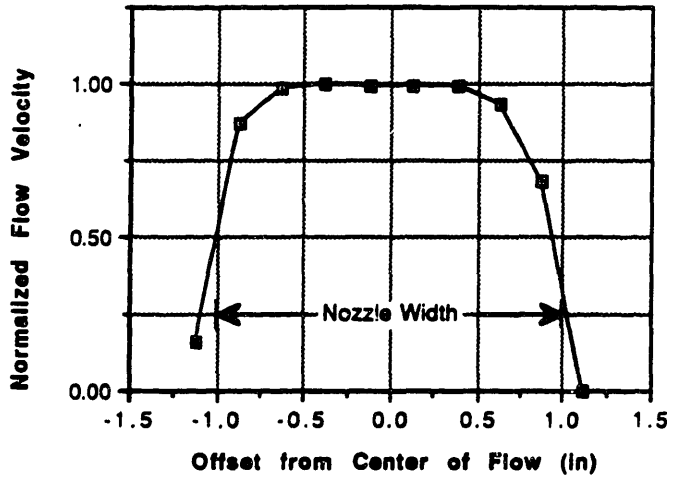

(b) 4 INCHES ABOVE NOZZLE

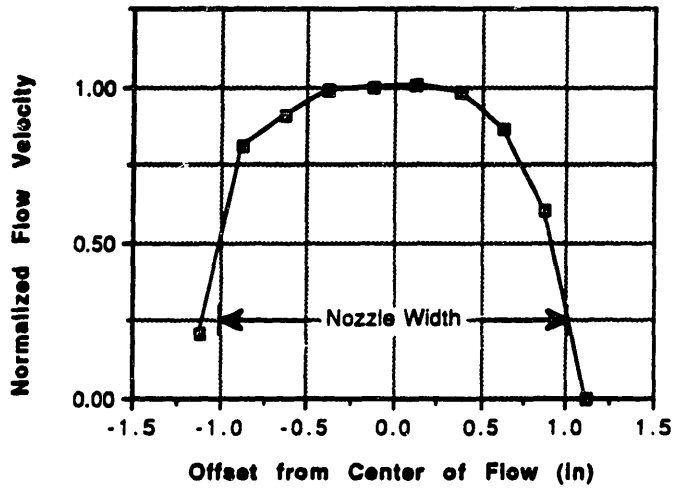

(c) 6 INCHES ABOVE NOZZLE

Figure 4-9: Velocity profile of the wind tunnel flow across the test section: (a) 2 inches above nozzle, (b) 4 inches above nozzle, (c) 6 inches above nozzle. The values were normalized with respect to the flow speed at the nozzle outlet. It is apparent that the flow is laminar at the test section, which is located 2 inches above the outlet.

motor with respect to the applied voltage and the linearity of the mass flow rate in the tunnel with respect to the rotation rate of the fan. The maximum flow speed attainable is 10.5 m/sec, which is greater than the terminal velocity of the largest stable water droplet at sea level.

4.3.2.2 Test Section and Acoustic Levitator Hardware

The test section of the Ventilated Facility, viewed from above, is shown in Fig. 4-10. Precise control of the acoustic field is not as critical in this facility as compared with the Vertical Facility, because the primary levitating force is aerodynamic. However, the strength of the acoustic field does have a bearing on the stability of a suspended sample in the presence of turbulence. Increasing the strength of the acoustic field increases the secondary forces that stabilize the sample within the test section. It is therefore desirable to maintain some degree of resonance tracking. As a result, the driver resonance tracking circuit is also employed in this facility. In addition, because the Ventilated Facility provides manual access to the reflector positioning mechanism, the positioning of the reflector was performed manually in lieu of implementing an automatic temperature compensator.

A plexiglass cylinder of 8 in. diameter encloses the test section. The laminar flow emerging from the contraction nozzle is 2 in. across. It is therefore assumed that the effect of this enclosure on the airstream is minimal. The enclosure has two large portals for the acoustic driver and reflector, located about 2 in. downstream of the outlet of the contraction region. Both the driver and reflector assemblies are mounted to an outer chamber along a horizontal axis. The inner chamber also has several small portals for droplet injection apparatus and diagnostic equipment. The lower 4 in. of the cylindrical inner chamber is uninsulated. This makes the test section visible to the naked eye, and allows access to video equipment. The heat transfer across this uninsulated section is negligible.

In Fig. 4-11, the temperature of the test section is plotted against time to assess the performance of the refrigeration system. The air in the wind tunnel was initially at room temperature, and the refrigeration system was run continuously. From the figure, a time

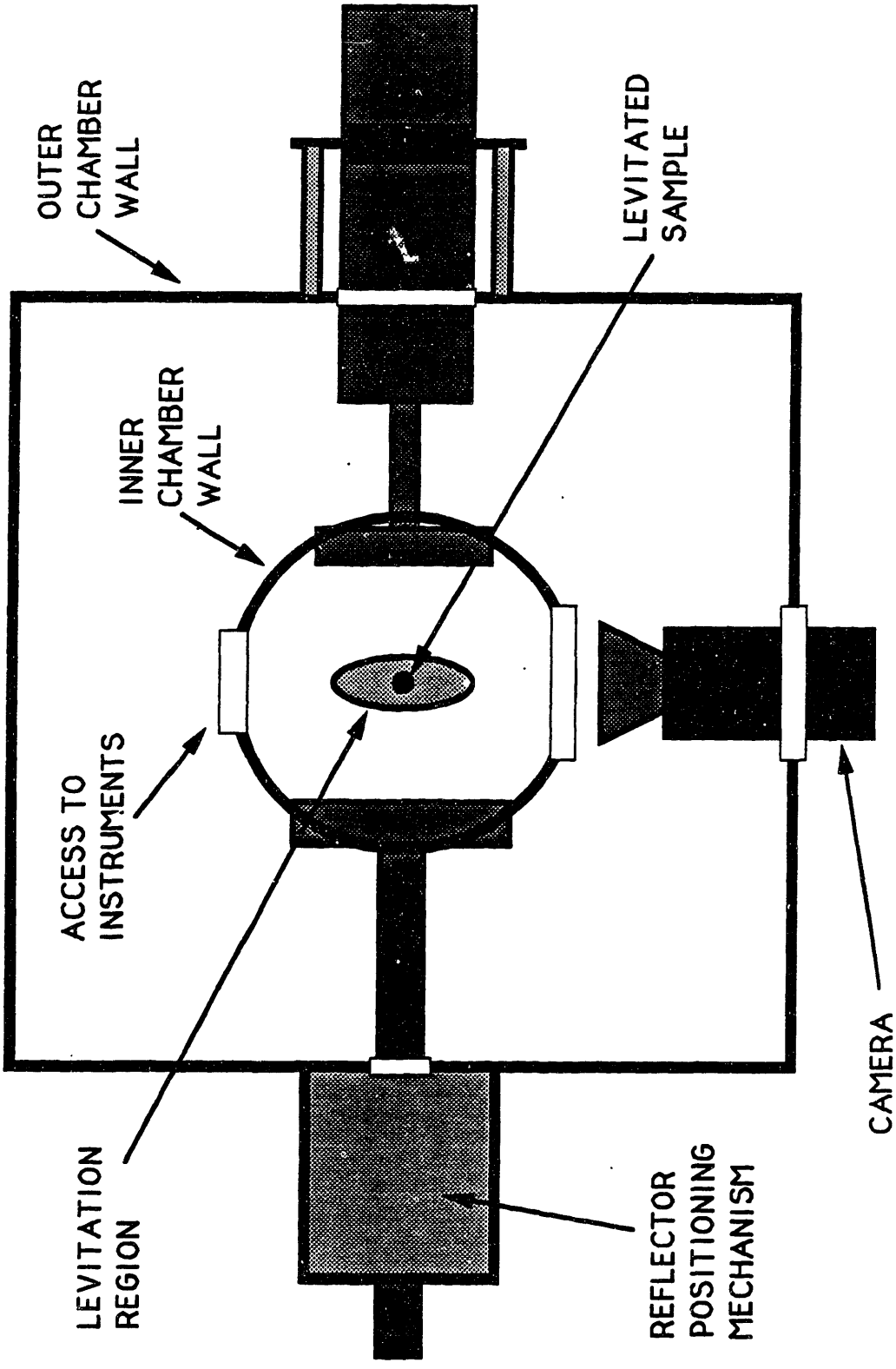

Figure 4-10: Top view of the test section of Ventilated Facility.

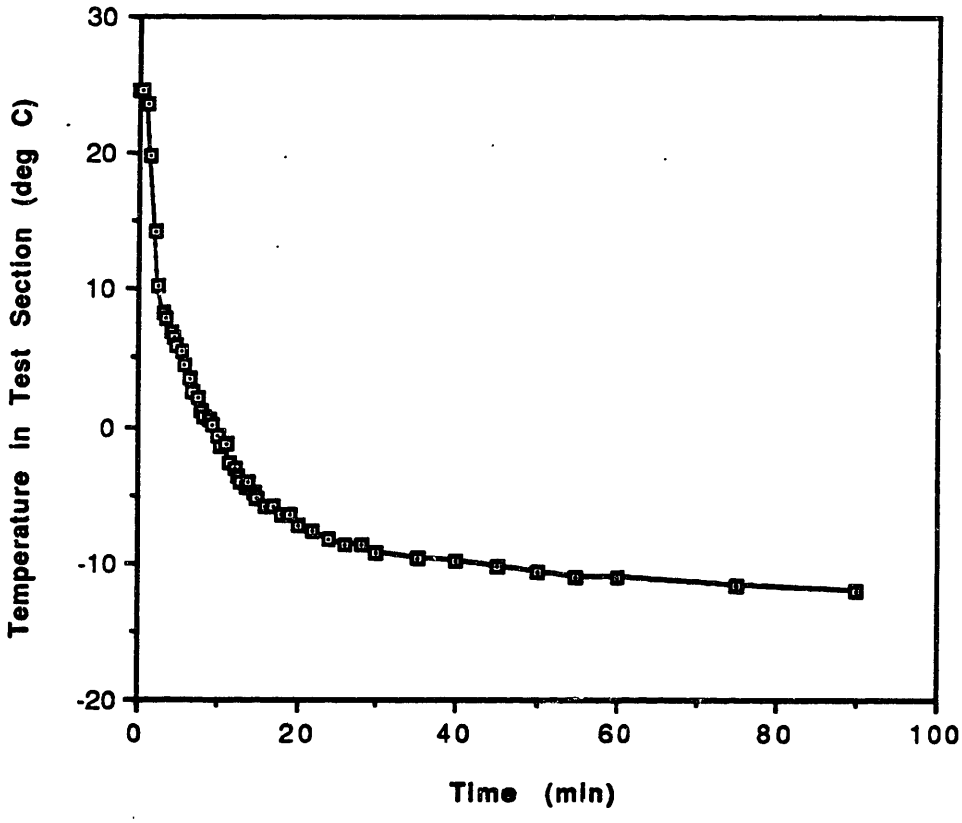

Figure 4-11: Temperature within the test section of the Ventilated Facility for an initial temperature of 24 deg. C. The refrigeration system operates continuously. The time constant associated with the heat capacity of the air in the wind tunnel is approximately 5 min.

constant of approximately 5 min was identified. This time constant is associated with the heat capacity of the air in the wind tunnel.

An additional feature of the Ventilated Facility is that the walls of the test section can be removed, if necessary, for experiments that do not require significant deviation from ambient temperature conditions. In this case, the wind tunnel is run as an open system, with the return channel removed. Objects suspended in the test section are then directly accessible to the experimenter and to closeup video equipment.

Objects suspended in the Ventilated Facility were confined to a nodal plane of the standing wave. Motion in this plane was observed in both the horizontal and vertical directions, however. This motion was due to small levels of turbulence in the wind tunnel airstream. Without the secondary stabilizing forces present in the acoustic field, this turbulence would be sufficient to perturb the object from the test section. As expected, a high intensity acoustic field facilitated the capture of objects in the test section, as the secondary acoustic forces were correspondingly greater. Once the object was captured, however, it was possible to reduce the field strength without losing droplet stability. At moderate field strengths, suspended droplets took the approximate shape of freely falling hydrometeors. Photographs of droplets suspended in the Ventilated Facility are shown in Fig. 4-12.

4.3.2.3 Design of Droplet Injector

An important operating issue for use of the Ventilated Facility is that of introducing liquid droplets into the Ventilated Facility. The requirement is that, upon injection, the droplet must be close enough to the proper location and velocity so that it may be captured by the acoustic field. Many droplet production devices have been developed for cloud research applications [15][16][17][18][19][20]. Unfortunately, most of these devices can produce droplets no larger than 0.1 mm. in diameter. Furthermore, many designs produce droplets streams rather than individual droplets. Finally, many of these production devices have large

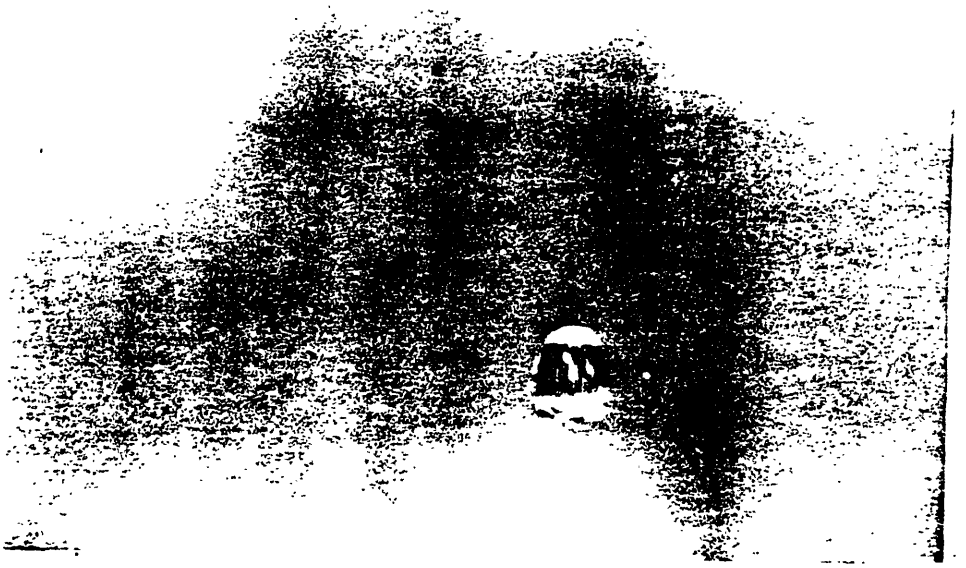

(a)

(b)

Figure 4-12: Photographs of droplets suspended in the Ventilated Facility: (a) single droplet, (b) pair of droplets in adjacent nodal planes. Gravity is directed downward. Note the effect of the acoustic field on the shapes of the droplets.

physical dimensions, which would interfere with the airflow in the tunnel. Consequently, a new approach was needed.

The greatest difficulty involved in designing the droplet injection mechanism for wind tunnel operation is related to the surface tension of the liquid. Clearly, to minimize flow disturbances, it is necessary to locate the injector downstream rather than upstream of the test section. The obvious approach is to place a narrow tube in the airstream, with the outlet facing upstream (in the direction of gravity), and let a prescribed amount of liquid flow out of the tube. This liquid collects on the tip of the instrument until the required volume is dispensed. At this point, however, it is difficult to release the droplet from the instrument due to the surface tension of the liquid, which causes it to stick to the instrument. The droplet will fall off the injector only when its weight becomes larger than the sum of the aerodynamic drag on the droplet and this surface tension force. At this point, however, the droplet is too heavy to be suspended by the wind tunnel alone, even with the secondary stabilizing forces arising from the acoustic field. As a result, the droplet falls upstream, passing through the test section and into the contraction nozzle.

In order to release the droplet from the injection device before it becomes exceedingly large, a force must be exerted on it. One way to achieve this is by pulsing a small amount of air around the surface the injection tube in the upstream direction, as shown in Fig. 4-13. This pushes the droplet off the device with a certain initial velocity. The velocity decreases rapidly as the droplet progresses upstream. If the initial velocity imparted is within a specific range, the droplet velocity will approach zero just as the droplet enters the acoustic region. At this point, the droplet is trapped in the test section by the acoustic stabilizing forces, sufficiently far away from the injection device so that its effect on the flow is negligible.

The droplet injector for the Ventilated Facility is shown in Fig. 4-14. The device is introduced several inches downstream (i.e., above) the test section. Liquid is introduced through the center channel of a probe and collects on the tip of the device. The pulse of air required to release the droplet is discharged through an outer channel of annular cross section,

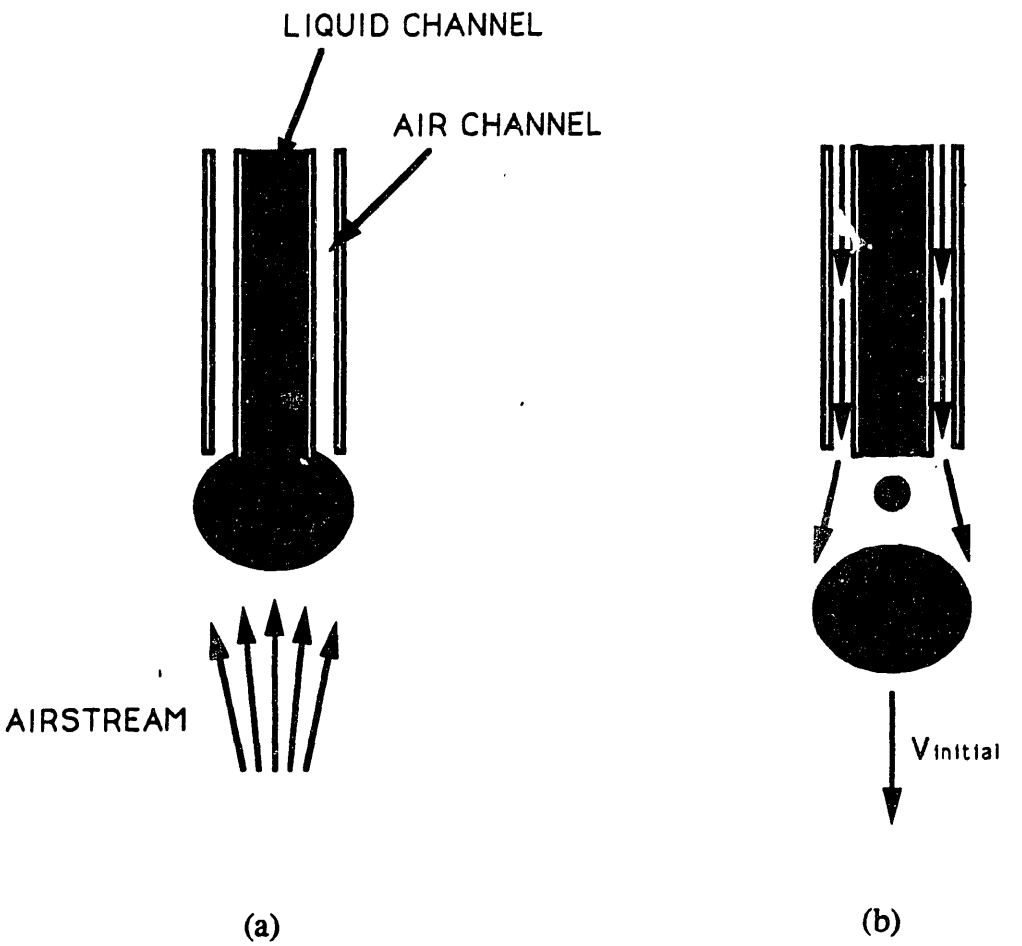

Figure 4-13: Droplet injector operation: (a) droplet attached to the tip of the injector by surface tension forces, (b) droplet released by an annular pulse of air. Note the possible formation of a satellite droplet.

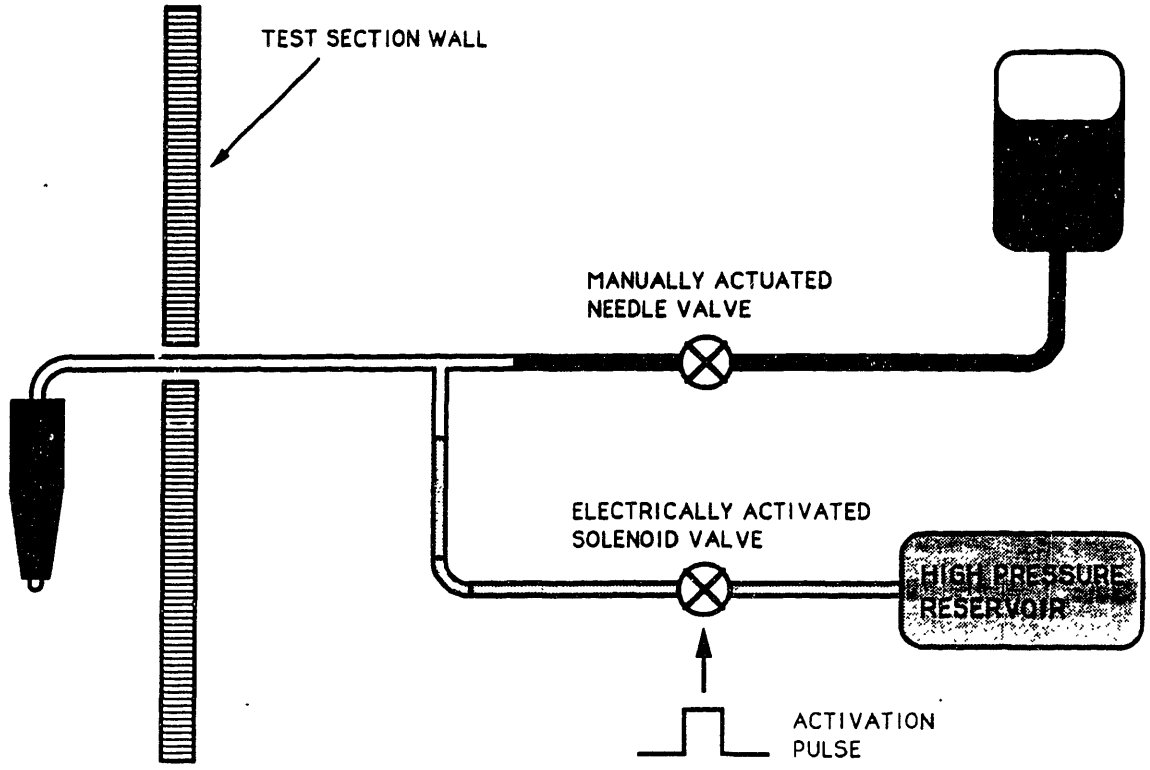

(a)

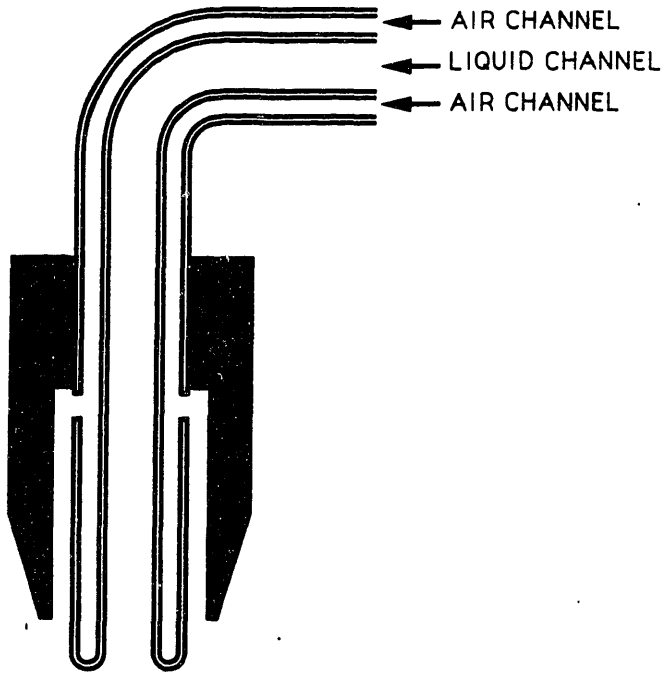

(b)

Figure 4-14: Diagram of the droplet injector: (a) complete injector, (b) closeup of the tip of the injector probe.

which has ports located around its circumference. A small plexiglass sheath surrounding the probe directs the pulse emerging from these ports into a uniform flow of annular cross section. The pulse is formed by drawing air from a high pressure reservoir controlled by a solenoid value. The solenoid value determines the duration over which the pulse lasts by receiving an electrical pulse of adjustable duration. Thus, the magnitude of the velocity imparted to the droplet is related to the droplet size, the pressure in the reservoir, and the solenoid pulse width.

Small droplets (having diameters smaller than 2 mm) were effectively released from the droplet injector into the airstream. Due to the sudden release of the droplet from the tip of the injector, a satellite droplet of smaller diameter was often formed. This droplet was almost always carried downstream by the flow in the test section, and did not affect the motion of the primary droplet. For droplet diameters greater than 2 mm, the performance of the injector was reduced significantly. As a large droplet was created on the tip of the injector, the flow field caused it to undergo rapid translational oscillations. As a result, it was difficult to predict the direction the droplet would travel upon its release from the injector. One possible solution to this problem would be to shield the tip of the injector, so that the local flow field is reduced and the corresponding aerodynamic forces on the droplet are diminished. The diameter of this shield would be large enough to contain the largest anticipated droplet, yet small enough so that its effect on the flow field in the test section can be neglected.

Rather than using a pulse of air to dislodge the droplet, it is also possible to utilize the hydrostatic pressure of the liquid supply to achieve the same effect. By quickly opening and closing the needle valve that controls the liquid flow rate, a small number of droplets is released from the tip of the injection device. The amount to which the valve is opened and the duration of this action determine the range of droplets sizes and the number of droplets released. Within this population of droplets, it is likely that at least one droplet will be captured in the acoustic field. This droplet has a terminal velocity approximately equal to the flow speed at the test section, and has approximately zero velocity relative to the acoustic field as is enters this region. This method, although performed manually, was quite repeatable. By selecting a flow

speed corresponding to the appropriate terminal velocity, a droplet of a desired size was introduced and stabilized in the test section. This method tended to work better for larger droplets.

4.4 Diagnostics and Data Acquisition

In order to monitor the operation of the acoustic driver, the pertinent signals are fed into an oscilloscope. These signals are the voltage applied to the driver, the current through it, the microphone signal, and the phase error signal described in Sec. 3.2.4. In this way, the status of the resonances of both the driver and acoustic field can be monitored, and the performance of the resonance tracking circuitry can be observed.

In the Vertical Facility, a number of thermometer probes are mounted within the inner and outer chamber. A portable temperature/humidity probe (Omega Instruments - model RH30-C) is used in both facilities. This probe is capable of measuring temperatures from -40 degrees to 500 degrees Celsius with 0.1 degree accuracy and relative humidities from 0 % to 99.9 % with 1 % accuracy. For the Ventilated Facility, a hot wire anemometer probe measures the flow speed. Its position within the test section can be adjusted, based on the particular experiment conducted.

Since both facilities have plexiglass test sections, video data is readily available. Cameras are used for still and motion picture photography. In addition, an infrared camera (Hughes Probeye - model 4100) is available for thermographic imaging. The camera has a range of -20 degrees C to 950 degrees C, and has a minimum resolution of 0.1 degree C. It can be used to study thermal effects in the test section and within the levitated object, such as the evaporative cooling of a suspended water droplet. In the Vertical Facility the closest proximity to the levitated sample attainable is eight inches with the levitator mounted inside the environmental chamber and two inches with the device operating in ambient conditions. In the Ventilated Facility, the closest proximity is six inches with the walls of the test section in place and three inches with the walls removed.

Chapter 5
Validation of the Facilities

5.1 Effect of the Acoustic Field on Ambient Conditions in the Test Section

Most cloud physics experiments call for an accurate replication of the ambient conditions in the atmosphere. It is therefore important to assess the effect of the acoustic field on the ambient conditions within the test sections of the Vertical and Ventilated Facilities. Two primary concerns are the possible creation of temperature gradients within the test section and the effect of the acoustic field on molecular diffusion. Both issues are examined here.

5.1.1 Temperature Gradients in the Test Section

A infrared thermographic image of the test section of the Vertical Facility, taken by the Hughes Probeye camera, is shown in Fig. 5-1. Different temperatures correspond to different colors in the images generated by the camera. The resolution selected for this image was 0.2 degrees Celsius per color. The presence of the acoustic levitator and the resulting acoustic field is apparent. The mechanical vibration of the transmitting plate of the driver results in the heating of this device, as expected. In addition, the acoustic standing wave itself creates small temperature gradients (less than 1 degree Celsius) within the test section. In the steady state, the power delivered to the acoustic field by the driver equals the rate of energy dissipation due to the viscosity of the acoustic medium and the dispersion of energy away from the test section. Of these two dissipative means, only the viscosity of the medium manifests itself as an increase in temperature. This effect can be seen in the figure. The nodal planes of the standing wave are seen as regions of increased temperature compared to the temperature within the antinodal planes. This indicates that the energy is being dissipated primarily in the vicinity of the nodal planes. The temperature within the nodal planes is approximately 21.2 degrees Celsius, while the temperature within the antinodal planes is in the neighborhood of 20.4 degrees. Celsius.

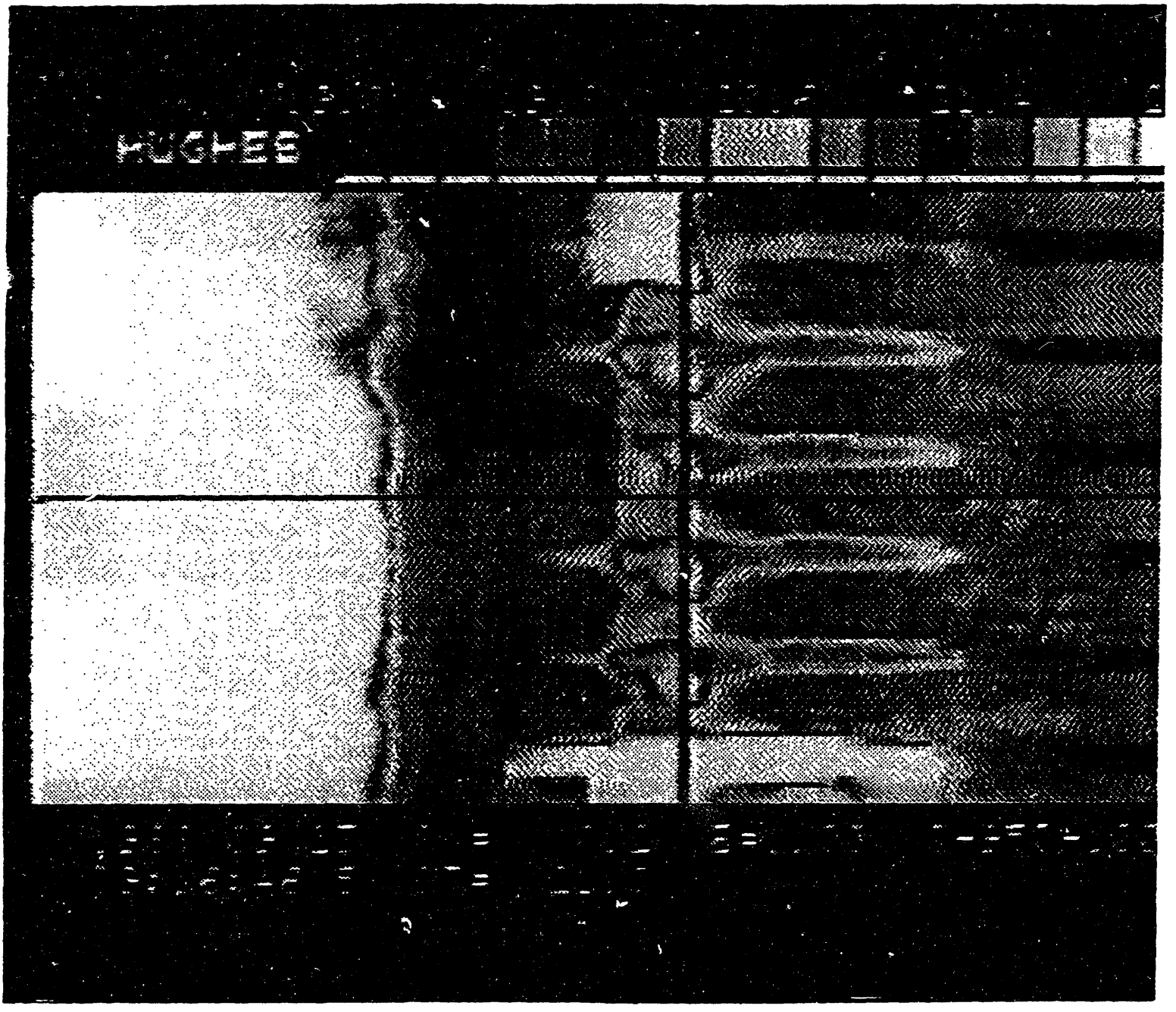

Figure 5-1: Thermographic image of the acoustic region in the Vertical Facility. The transmitting plate of the driver is at the bottom of the image, and the reflector is at the top. The heating of the transmitting plate due to mechanical vibration is apparent. The nodal planes are clearly visible as regions of increased temperature.

5.1.2 Molecular Diffusion Processes

In Fig. 5-2, a thermographic image of an evaporating droplet is shown. The nodal planes of the acoustic field are also visible. From this image, several observations can be made. First, the equilibrium position of the droplet is located slightly below the nodal plane. This is consistent with the theory developed in Chapter 2, which relates the equilibrium position of the droplet with the magnitude of the acoustic energy. Also, the surface temperature of the droplet is slightly below that of the surroundings. This is indicative of the evaporation of the droplet, and is related to the latent heat of vaporization of water. The observed surface temperature of the droplet is approximately 19.4 degrees Celsius, while the temperature of the air in the vicinity of the droplet is in the neighborhood of 20.8 degrees Celsius.

Many cloud physics experiments (e.g., trace gas absorption studies, evaporation experiments) relate to molecular diffusion processes within the medium surrounding a hydrometeor. It is therefore important to assess the effect of the acoustic field on molecular diffusion. As a result, a set of evaporation experiments were conducted.

The acoustic levitation theory presented in Chapter 2 predicts that, for small objects ($\alpha << 1$), the acoustic force varies as the cube of the radius of the object. Because the mass of a homogeneous object exhibits a similar dependence, it is anticipated that the acoustic field affects all particles equally. The theory predicts that the acoustic energy required for levitation is independent of particle radius, and depends only on the density of the particle. It is postulated that this effect is no longer valid as the particle diameter approaches the molecular scale. For particles this small, the surrounding medium can no longer be considered a continuum, as the mean free path of the molecules in the medium becomes significant. It is therefore postulated that the acoustic field does not affect phenomena on the molecular scale, such as water vapor diffusion.

The theoretical formulation which predicts droplet evaporation rates is identical to that utilized in determining droplet condensation growth rates in supersaturated environments [21].

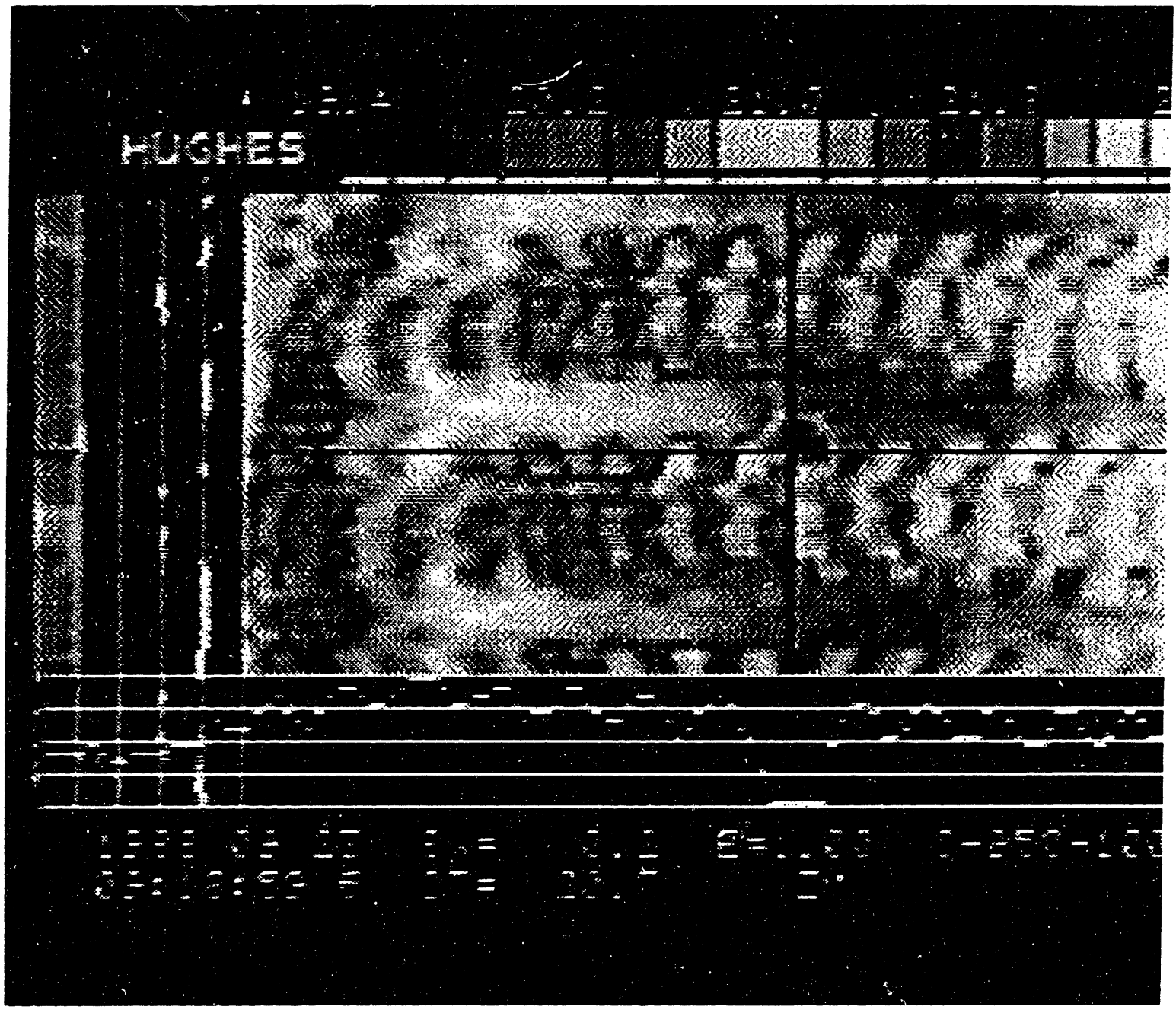

Figure 5-2: Enlarged view of the acoustic region of the Vertical Facility. Three nodal planes are visible, and a suspended water droplet is identified by the crosshairs. The equilibrium location of the droplet is slightly below the nodal plane of the acoustic field, as predicted by the theory. The temperature profiles along the crosshairs are shown along the left and lower borders of the image. Because the droplet is evaporating, its surface temperature (approximately 19.4 deg. C) is slightly below the local temperature in the test section (approximately 20.8 deg. C).

As a result, only the highlights of the underlying theory are presented here. If the ambient conditions (namely temperature and saturation ratio) in which the droplet lies do not change appreciably during the evaporation process, the droplet evaporation relation can be expressed as:

$$a\frac{da}{dt} = \frac{D_v}{\rho_l}(s_\infty \rho_{sat,\infty} - \rho_{sat,a}) \tag{6.1}$$

where a represents the radius of the droplet, D_v is the diffusivity of air, ρ_l is the density of water, s_∞ is the ambient saturation ratio, $\rho_{sat,\infty}$ is the ambient saturation vapor density and $\rho_{sat,a}$ is the saturation vapor density at the surface of the droplet. This equation gives the droplet evaporation rate as a function of the ambient conditions and the surface vapor density. For droplets visible to the naked eye, the surface vapor density is approximately constant over the duration of the evaporation. As a result, an evaporation rate constant, K, can be defined as follows:

$$K = \frac{D_v}{\rho_l}(\rho_{sat,a} - s_\infty \rho_{sat,\infty}) \tag{6.2}$$

Eq. (6.1) can then be integrated in time, yielding:

$$a(t) = \sqrt{a_0^2 - 2Kt} \tag{6.3}$$

where a_0 is the initial radius of the droplet. Results from the evaporation theory indicate that the magnitude of K decreases with increasing humidity, and that no evaporation occurs at saturation.

In order to study the effect of the acoustic field on molecular diffusion processes, a series of evaporation tests was conducted. The evaporation of levitated droplets was compared with the evaporation of droplets suspended on fine glass fibers. For each trial, the time history of the radius of the droplet was recorded. An evaporation rate constant, K, was then chosen to best fit the curve described by Eq. (6.3) to the data. An example of the time history of the

radius of a levitated droplet, along with the estimated value of K is shown in Fig. 5-3 (a). In Fig. 5-3 (b), the experimentally determined evaporation rate constants are plotted for several trials under varying ambient conditions, showing reasonable agreement between the rates associated with levitated droplets and the rates associated with droplets suspended in the Vertical Facility. It is presumed that secondary effects induced by the standing wave (droplet motion, small temperature gradients) introduced slight deviations from predicted evaporation rates. It follows that, to first order, the acoustic field does not affect diffusion processes on the molecular scale.

5.2 Effect of the Acoustic Field on Levitated Hydrometeors

The acoustic levitators for both facilities confine suspended samples to regions in the vicinity of the nodal planes of the acoustic field. This positioning is effected by pressure deviations over the surface of the sample. The ability to achieve precise positioning allows carefully controlled experiments to be conducted in either facility. However, this method of contact-free positioning does have limitations. The acoustic field cannot support objects above a critical size, and the pressure forces tend to deform liquid samples. These limitations, predicted in Chapter 2, are studied in detail here.

5.2.1 Solid Samples

The acoustic levitation theory predicts a rapid falloff in levitating force for spherical objects of large diameter, corresponding to $\alpha > 1$. For an acoustic wavelength of 1.5 cm, this falloff occurs at diameters greater than 5 mm. It is also predicted that the levitating force falls to zero for $\alpha = 2$, corresponding to a diameter of 10 mm. In order to establish these effects experimentally, styrofoam spheres of increasing size were placed in the acoustic field, and their motions were observed. Small spheres ($\alpha < 1$) were highly stable, rarely departing more than 0.5 cm from the driver axis. Surface roughness effects occasionally introduced rotations in the sample about the driver axis until a stable equilibrium orientation was achieved. Larger spheres

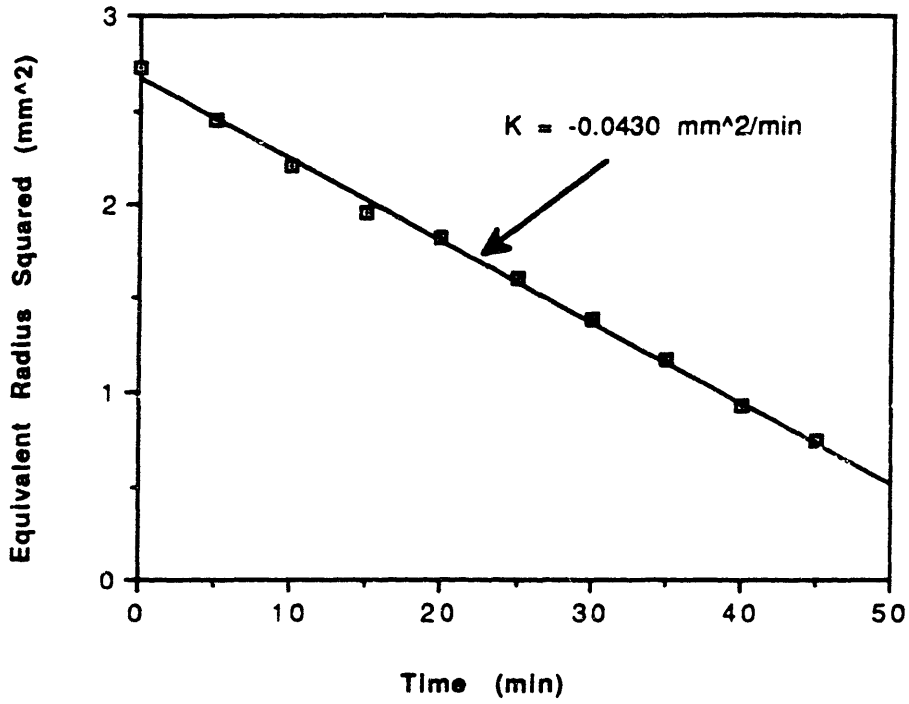

(a)

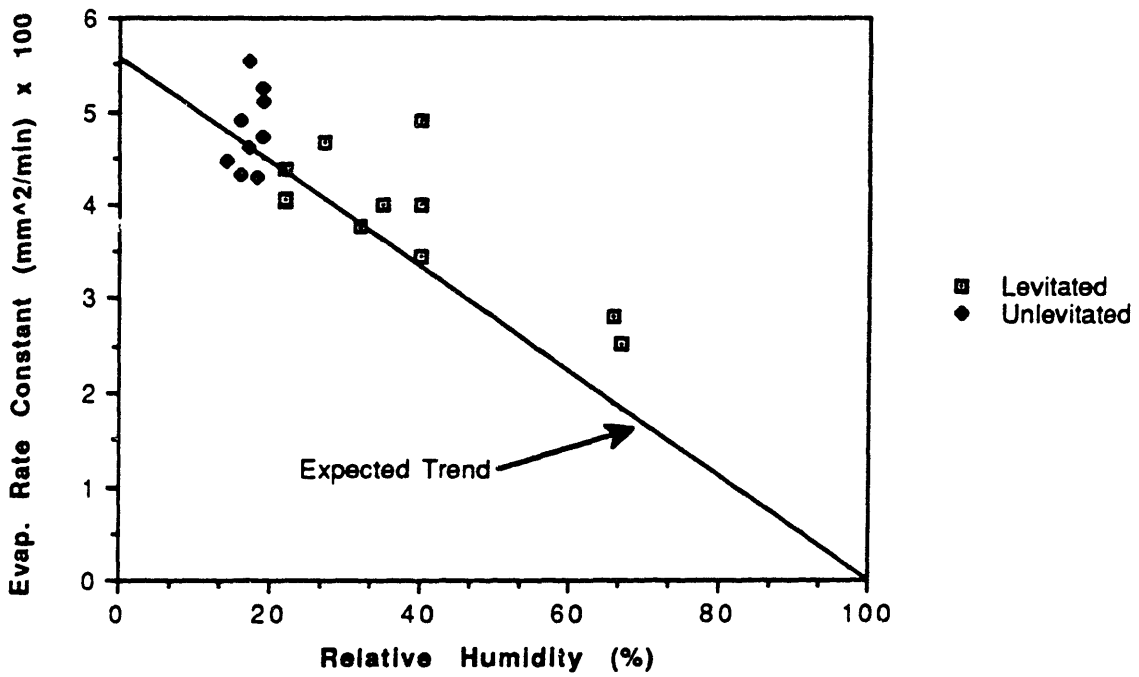

(b)

Figure 5-3: Comparison between the evaporation rate constants of levitated water droplets and droplets suspended from a glass rod for different ambient saturation levels. In (a), the time history of the square of the radius of a representative droplet is shown. According to the theory, the plot should be a straight line with a slope equal to the evaporation rate constant. In (b), the evaporation rate constants determined from several experiments are plotted, showing reasonable agreement between the levitated and suspended droplets.

experienced greater rotation rates, as well as occasional oscillations along the driver axis, as described in Sec. 2.2.2.2. In Fig. 5-4, a styrofoam ball of 8 mm diameter is shown levitated in the Vertical Facility. The largest samples levitated, for which α approached 1.8 (a diameter of approximately 9 mm), exhibited highly unpredictable behavior, jumping between nodal planes as a result of random changes in orientation. Still larger spheres could not be suspended in the acoustic field. This agrees quite well with the theory, which predicts the loss of levitation capability at a diameter in the neighborhood of 10 mm.

5.2.2 Liquid Samples

The primary effect of the acoustic field on a levitated droplet is to deform it into an oblate spheroid. The extent to which the droplet is distorted depends on the surface tension of the droplet, the magnitude of the acoustic field, and the size of the droplet. Whereas small droplet shape distortion is not expected to affect the levitation performance in the Vertical Facility, this phenomenon can have a profound effect in the Ventilated Facility if the acoustic field is too strong. The shape distortion alters the terminal velocity of the droplet, which makes it necessary to adjust the flow velocity in order to maintain stability. These effects are studied below.

5.2.2.1 Droplet Shape Distortions in the Vertical Facility

In Fig. 5-5, a large water droplet is shown suspended in the Vertical Facility, and the shape distortion is clearly visible. The dimensions of this droplet are 5 mm in diameter by 2 mm thick, corresponding to an equivalent radius of 1.8 mm. These distortions become more severe with larger droplets, eventually resulting in droplet shatter.

It is important to note that the deformations associated with droplets suspended in the Vertical Facility correspond, to first order, to the deformations characteristic of freely falling raindrops. In an earlier work by Green [22], an approximate relationship was derived which related the radius and aspect ratio of a freely falling droplet. The result was based on the

Figure 5-4: Photograph of a large (8 mm diameter) styrofoam ball suspended in the Vertical Facility. The nonspherical shape of the object, along with occasional perturbations in the ambient flow field, cause random changes in the orientation of the object. Objects of larger size cannot be levitated in the acoustic field.

Figure 5-5: Photograph of large water droplet in Vertical Facility showing the effect of the acoustic forces. The droplet is distorted into an oblate spheroid whose approximate dimensions are 5 mm by 2 mm.

assumption that the dynamic stresses caused by the flow around the droplet are small compared to the hydrostatic and surface tension forces within the droplet itself. The theory predicts:

$$a = \sqrt{\frac{\sigma}{g\rho_l}} \frac{\sqrt{(b/a)^{-2} - 2(b/a)^{-1/3} + 1}}{(b/a)^{-1/6}} \tag{6.4}$$

where the quantity (b/a) represents the droplet aspect ratio. This relationship has been found to be consistant with experimentally determined results in free fall chambers and vertical wind tunnels [23].

In order to compare the deformations of levitated droplets with the relationship developed by Green, the aspect ratios of water droplets suspended in the Vertical Facility were analysed. For each trial, the intensity of the acoustic field was slowly lowered until the acoustic force was insufficient to levitate the droplet. The droplets were filmed with a video camera operating at 30 frames per second. For each trial, the instant where loss of levitation occured was located by advancing frame-by-frame through the film. The aspect ratio of each droplet was recorded by observing the frame just before the droplet was lost. As a result, the data corresponds, approximately, to a normalized acoustic energy of $\tilde{E} = 1$. Small droplets remained roughly spherical, while larger droplets deformed into oblate spheroids. In Fig. 5-6, the observed aspect ratios are compared with Green's relationship, showing reasonable agreement with the theory. The predicted aspect ratios of the levitated droplets, derived from the theory in Chapter 2, are also shown in this figure. The theoretical value of $\tilde{E}$ used was 1.0. As predicted, the upper and lower surfaces of large droplets became concave at the onset of instability and rupture. This occured at a value of α near 0.7, which is consistent with the theoretical limit. The equivalent radius for a droplet of this size is approximately 1.75 mm. These results indicate that the Vertical Facility is capable of replicating, to first order, the shapes of freely falling water droplets in the atmosphere.

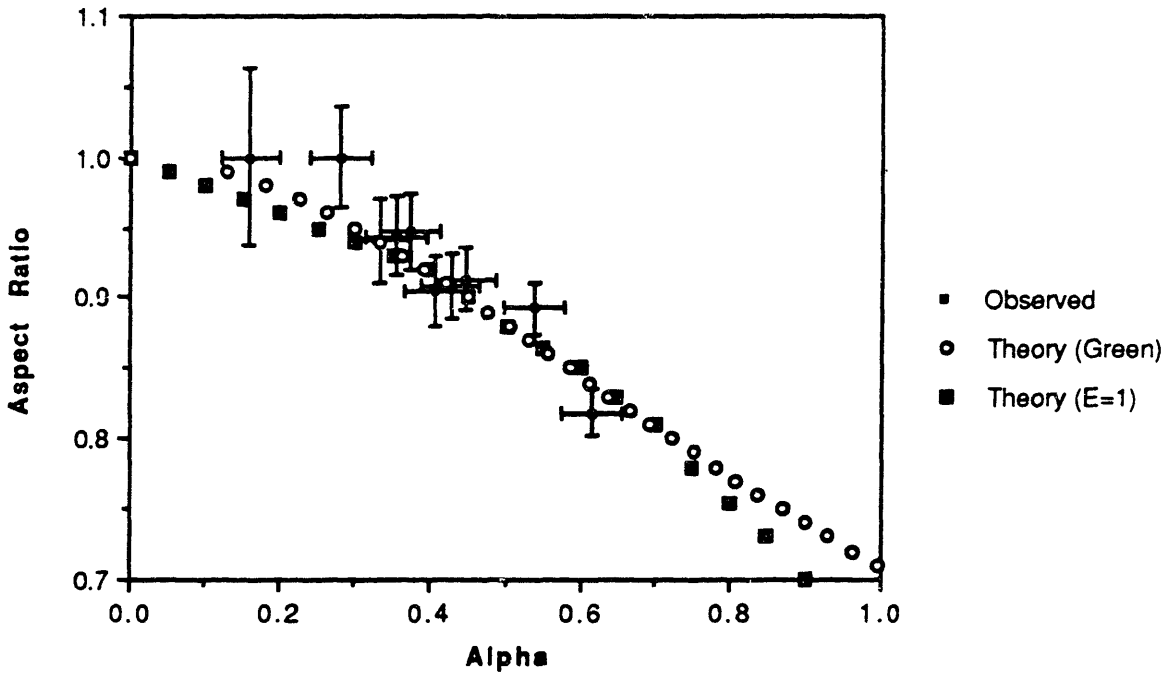

Figure 5-6: Comparison between the aspect ratios of droplets suspended against gravity in the Vertical Facility and aspect ratios of freely falling raindrops, as predicted by Green [22]. The predictions from the theory presented in Chapter 2 are also shown. The resolution of the photographic equipment used to observe the droplets is approximately 0.1 mm. As a result, small droplets appear ideally spherical (having an aspect ratio of unity), even though the acoustic field does cause a small amount of deformation. Nevertheless, there is reasonable agreement with both Green's theory and the acoustic levitation theory.

5.2.2.2 Capture Range Enhancement in the Ventilated Facility

The acoustic field present in the Ventilated Facility is not required to be as strong as the field in the Vertical Facility, because the primary levitating force is aerodynamic. Consequently, the shape deformations characteristic of liquid droplets in the Vertical Facility are not as pronounced in the Ventilated Facility. It is therefore assumed that the terminal velocity of a given droplet suspended in the Ventilated Facility should correspond well to the terminal velocity in free fall. As a result, it is anticipated that the flow field developed around the droplet in the Ventilated Facility will closely resemble the ambient flow field around the freely falling hydrometeor. The effect of changing the acoustic field strength on suspended droplets in the Ventilated Facility is shown in Fig. 5-7.

In order to confirm this claim, a study was conducted which compared these terminal velocities. Water droplets of various sizes were suspended in the Ventilated Facility. The excitation signal applied to the driver was in the neighborhood of 70 volts (peak-to-peak), which resulted in a normalized acoustic energy ($\tilde{E}$) of approximately 0.5.[2] For each trial, the wind tunnel flow speed was either increased or decreased until the acoustic field could no longer prevent the droplet from escaping. The flow speed at which this occurred was noted. Two sets of data were therefore generated. The first corresponded to the upper limit on the flow speed for a given droplet size, while the second set corresponded to the lower limit. For water droplets falling freely in the atmosphere, the terminal velocity as a function of droplet diameter was determined empirically [10]. The results from the Ventilated Facility, along with the empirically established terminal velocity, are plotted in Fig. 5-8. From this figure, we see that the upper and lower velocity limits bound the empirically based terminal velocity curve. It is therefore apparent that the droplet shape distortions in the Ventilated Facility do not affect the

[2]This value was determined based on the amplitude of the excitation signal. In the vertical facility (which contains a similar acoustic driver), it was determined that at least 100 volts (peak-to-peak) was required to support water droplets against gravity. It was therefore assumed that this amplitude corresponded to $\tilde{E} = 1$. Because the energy delivered to the driver is proportional to the square of the amplitude of the excitation signal, a 70 volt signal delivers about half as much power to the driver. The acoustic field strength in the Ventilated Facility was therefore estimated as $\tilde{E} = 0.5$ for this experiment.

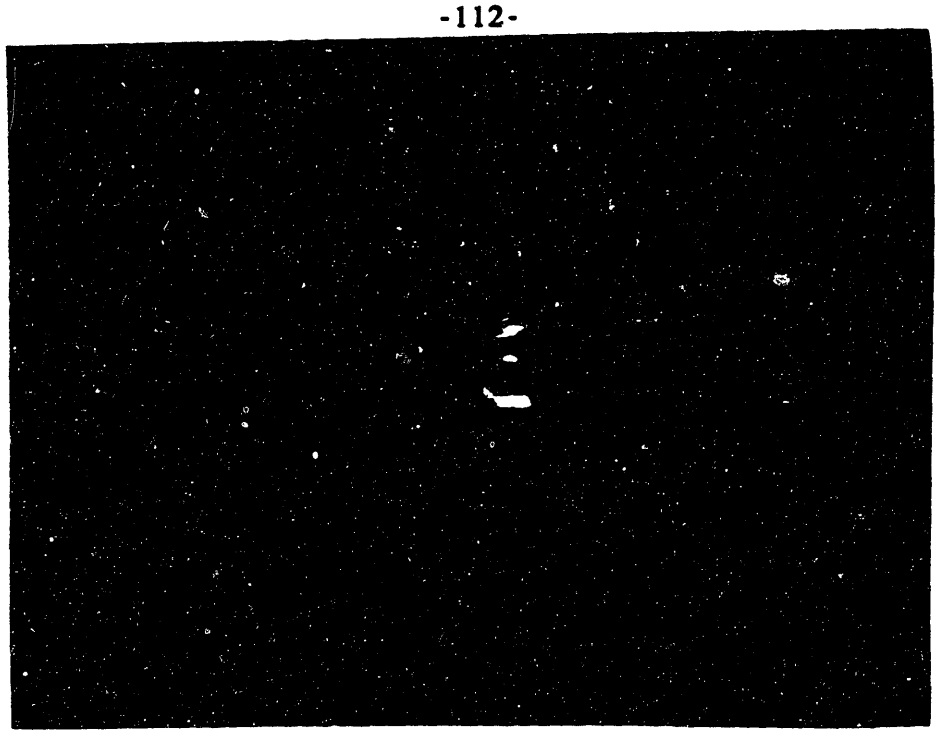

(a)

(b)

Figure 5-7: Photographs of droplets suspended in the Ventilated Facility under different acoustic field strengths: (a) high intensity field, (b) moderate intensity field. The change in the shape of the droplet is apparent.

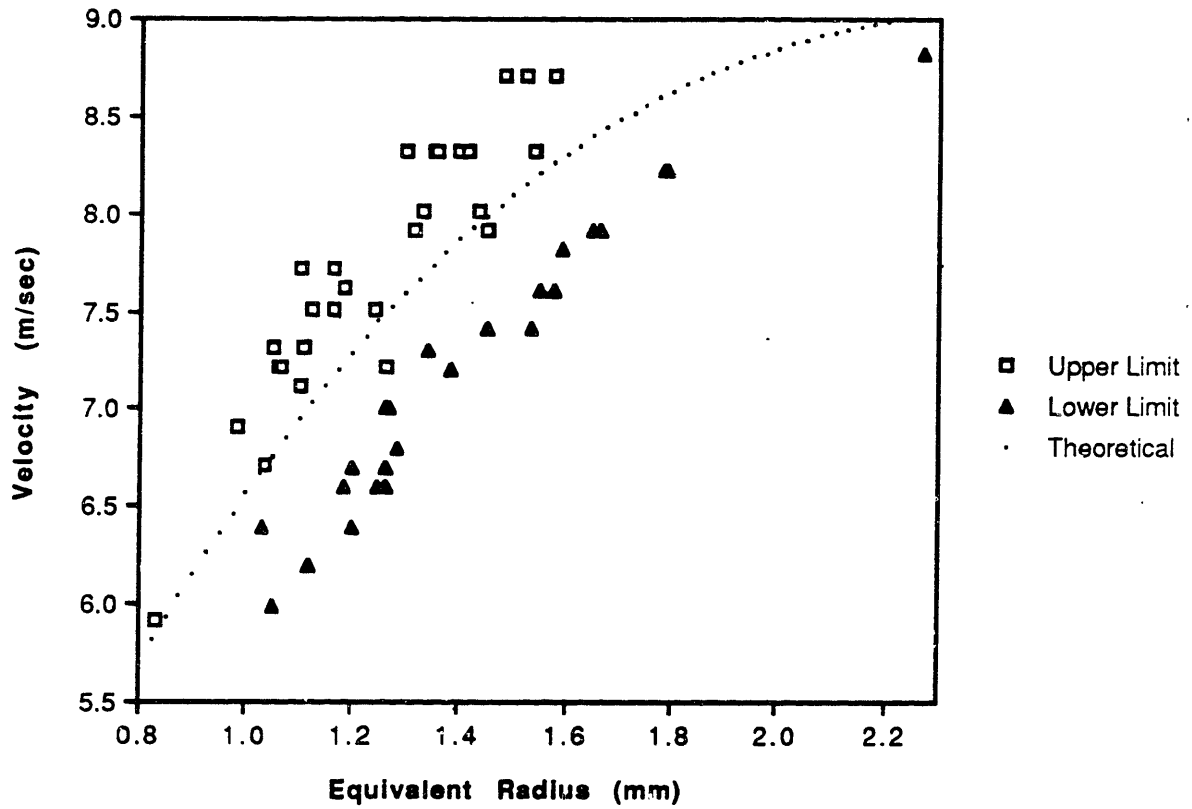

Figure 5-8: Experimentally determined upper and lower flow velocity limits for droplets suspended in the Ventilated Facilty. The empirically determined terminal velocity of droplets at sea level is shown for comparison. The data indicates a capture range of about ± 0.4 m/sec from this curve for droplet radii between 1 mm and 2 mm.

terminal velocity of the droplets significantly, provided that the acoustic field strength is moderate.

The upper and lower velocity limits, determined experimentally, define a velocity capture range for the Ventilated Facility. The data indicates that this capture range extends approximately ± 0.4 m/sec from the theoretical terminal velocity for droplet sizes between 2 mm and 4 mm in diameter. It is interesting to note that the equilibrium position of a suspended droplet in the vertical direction was observed to change as the flow speed was altered slightly. Near the upper limit, the droplet was stable downstream of the axis of the driver, and near the lower limit, the droplet was stable upstream of the axis of the driver. This phenomenon is consistent with the presence of the secondary acoustic restoring forces. As a result, the degree to which the flow speed deviates from the actual terminal velocity of the droplet can be determined by observing the equilibrium location of the droplet. This suggests that feedback control of the wind tunnel velocity, based on the droplet position, can be implemented. This approach would be extremely useful if the aerodynamic drag on a suspended droplet changes considerably over the course of an experiment. For example, if evaporation of the droplet were to occur, the controller would gradually reduce the flow speed to correspond to the changing terminal velocity of the droplet.

5.2.3 Phase Change Phenomena

In order to demonstrate the capability of the acoustic levitation facility to support an object over changing conditions, a series of phase change experiments were conducted in both facilities. Water droplets were introduced into the Ventilated Facility, and the wind tunnel temperature was reduced to freezing levels. Over the course of each trial, the reflector position was manually adjusted to compensate for the changing acoustic wavelength of the standing wave. This stabilized the droplet in the acoustic field over the entire course of the experiment. A video camera filmed each trial, and the temperature of the test section was recorded periodically.

Images of freezing droplets suspended in the Ventilated Facility are shown in Fig. 5-9. Two types of freezing phenomena were observed, depending on the initial temperature of the airstream. Droplets introduced into a cold environment (where the temperature of the airstream was already below 0 degrees Celsius), froze rather suddenly. Within the span of 30 milliseconds, the droplet, which originally appeared transparent, became opaque. This was indicative of the sudden freezing of the entire surface of the droplet. The frozen droplet remained essentially spherical, and gradually accreted ice from the vapor in the airstream. As the accretion process continued, the asymmetry of the frozen droplet increased. The terminal velocity gradually became sensitive to the orientation of the frozen object, due to its nonspherical shape. Eventually, the acoustic field was incapable of stabilizing the sample for all orientations, and the sample was lost. This type of freezing suggests that under these conditions the center of the droplet is still warm when the outer surface freezes. It should be noted that the airstream temperature must be several degrees below freezing for this phenomena to occur.

Droplets introduced into a warm environment exhibited a different behavior altogether. As the airstream was slowly chilled, freezing was initiated from within the droplet, resulting in crystalline structures propagating outwards from the center of the droplet. The observed droplet remained translucent, and the crystal growth was apparent to the naked eye. Because the crystal structure was irregular, the terminal velocity of the freezing droplet was extremely sensitive to orientation, and stability of the sample was difficult to maintain. These observations suggest that the temperature profile within the droplet was essentially uniform, and nucleation was not restricted to the droplet surface alone.

The phase change phenomenon was also studied in the Vertical Facility. In Fig. 5-10, consecutive frames from a videotape of a levitated droplet are shown. The droplet, initially at room temperature, was placed in the test section of the facility, where the temperature was set at -13 degrees Celsius. As expected, freezing occurred over the entire surface of the droplet in

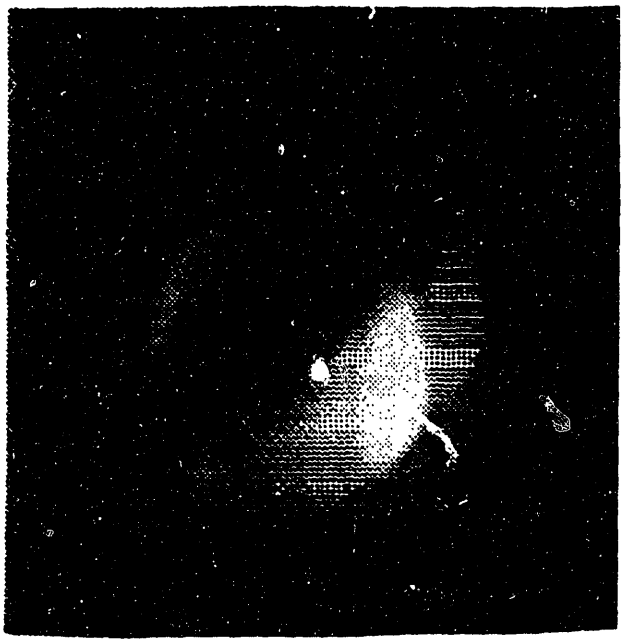

BEFORE FREEZING

AFTER FREEZING

(a)

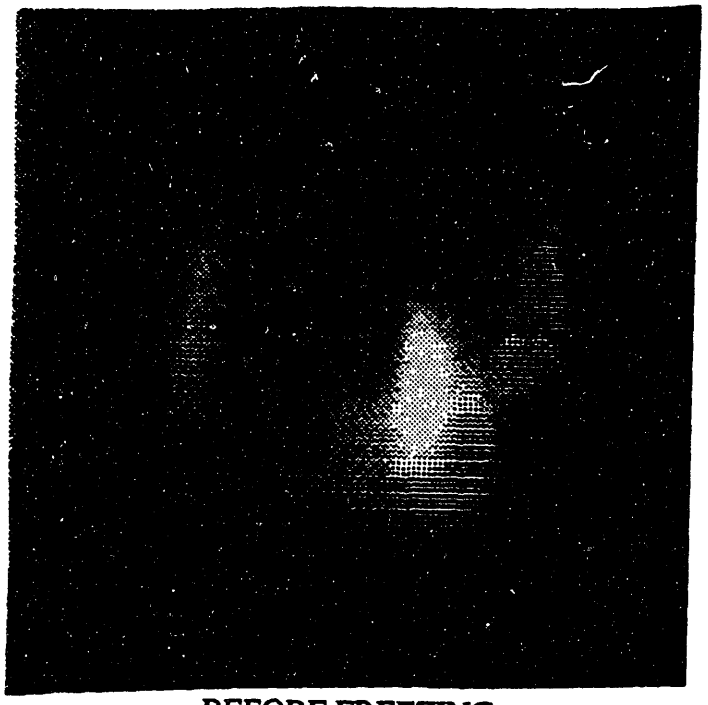

BEFORE FREEZING

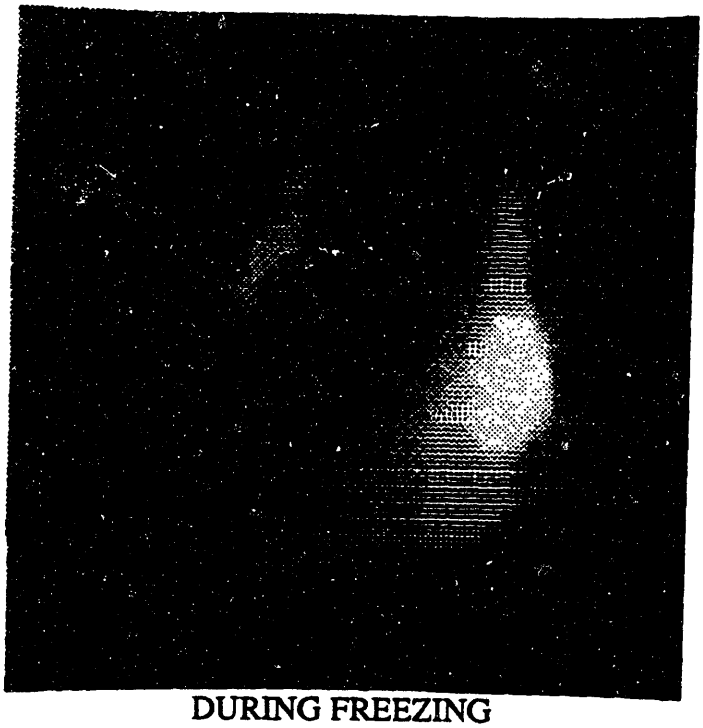

DURING FREEZING

(b)

Figure 5-9: Results from the freezing experiments in the Ventilated Facility. These photographs were digitized from a videotape, so that consecutive frames could be shown. In (a), the ambient temperature was -6 deg. Celsius, and the frames shown are 1/30 sec. apart. The sudden freezing of the surface of the droplet is apparent. In (b), the ambient temperature was only slightly below freezing, and the frames shown are approximately 1 sec. apart. The gradual growth of an ice crystal, while difficult to see here, was observed by the naked eye during the experiment. The quality of these images was deteriorated significantly by poor lighting during the experiment and by the digitization process itself.

(a) BEFORE FREEZING

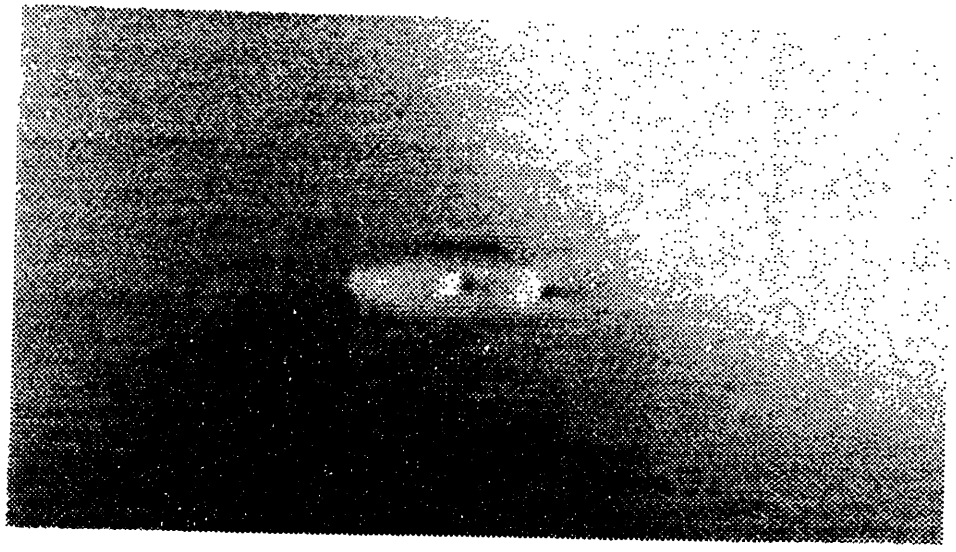

(b) AFTER FREEZING

Figure 5-10: Consecutive frames from a video of a droplet suspended in the Vertical Facility. The ambient temperature is -13 deg. C. The frames are 1/30 sec. apart. The sudden freezing of the entire outer surface of the droplet suggests that the outer surface was supercooled before freezing. It is important to note that the apparent change in the aspect ratio of the droplet between the two frames is an optical effect. The upper and lower surfaces of the droplet are lost in the background of the second image, making the droplet appear more distorted than in the first image.

the span of one frame of the videotape (1/30 second), suggesting that the surface of the droplet cooled faster than its center.

Chapter 6
Conclusion and Recommendations

6.1 Summary of Results

The basic capabilities of both the Vertical and the Ventilated Acoustic Levitation Test Facility have been demonstrated. In the Vertical Facility, solid samples as large as 9 mm in diameter were levitated. The primary limitation on sample size is related to the nondimensional parameter, α, which is a measure of the fraction of the acoustic standing wave occupied by the sample. As a result, levitation of larger objects requires a longer acoustic wavelength and a correspondingly lower frequency. In the interest of safety and comfort, the acoustic levitator designed here operates at a frequency just above the upper range of human hearing. It should be noted that protection of human operators should be incorporated into a facility designed to operate at a lower frequency.

The capability of the Vertical Facility to support liquid samples was also demonstrated. For this case, the droplet size limitation was related to droplet deformation constraints. Beyond a critical size, the surface tension forces were insufficient to maintain droplet stability in the presence of the acoustic field. This occured at an equivalent droplet diameter of approximately 4 mm. Droplets of this size deformed into oblate spheroids under the effect of the acoustic forces.

It was also verified that the acoustic field present in the Vertical Facility does not significantly affect molecular diffusion in the test section. It is therefore possible to conduct trace gas absorption and evaporation experiments in this Facility without any significant effect on the diffusion process by the acoustic field.

Finally, the ability to study phase change phenomena in the Vertical Facility was demonstrated. Stability of the levitated sample was maintained even as the sample froze. This capability makes it possible to study phenomena such as ice nucleation in this facility.

In the Ventilated Facility, the capability of the wind tunnel to provide the levitating force on water droplets was demonstrated. The flow speed could be made sufficiently high so that even the largest stable droplets could be levitated. The acoustic field, used only for stabilization in this facility, could be reduced to moderate levels while still maintaining positional stability of the droplet. As a result, the shape deformations characteristic of levitated droplets in the Vertical Facility were not as pronounced in the Ventilated Facility. This was validated by comparing the terminal velocities of droplets suspended in the Ventilated Facility with empirical results from studies of droplets in free fall. The flow field around freely falling hydrometeors was therefore successfully simulated in the Ventilated Facility.

Stability during phase change was also demonstrated in the Ventilated Facility. The acoustic field successfully stabilized the droplet within the test section during the transition from liquid to solid phase. Provided that shape asymmetry effects did not become significant, the frozen droplet could be suspended indefinitely. As the nonuniformity of the surface became significant, the terminal velocity of the frozen droplet became increasingly sensitive to orientation. As a result, stability became more difficult to maintain. In order to compensate for this effect, the acoustic field could be intensified, resulting in increased stabilizing forces. Because the frozen droplet was not subject to acoustically induced shape deformations, the maximum acoustic field strength was limited only by the capabilities of the acoustic driver hardware.

6.2 Recommendations for Future Development

A number of additional enhancements can be made to both facilities. In the Vertical Facility, a method of creating more rapid temperature changes in the test section while maintaining stability of the levitated object is desired. The rate at which the temperature in the test section can be changed is limited by the heat transfer across the walls of the inner chamber. This chamber is used to prevent the circulating air in the environmental chamber from perturbing the levitated object. One approach would be to use a more highly conductive

material for these walls. It is important that the temperature compensation system be capable of responding to rapid changes in temperature, should such an approach be implemented.

In the Ventilated Facility, a major improvement can be made concerning the introduction of droplets into the test section. The current droplet injector is repeatable for small droplets, but highly unpredictable for larger droplets. More research is required to develop a reliable method of releasing a droplet into the test section in a repeatable manner. One approach, mentioned in Chapter 5, would be to shield the tip of the injector probe. This would reduce the magnitude of the aerodynamic forces on the droplet prior to release. The position of the droplet at the time of release would then be more predictable.

It would also be useful to develop some method of automatic control of the wind tunnel flow velocity. As the suspended droplet evaporates, its terminal velocity is reduced. Eventually, a point is reached where the forces from the acoustic field are insufficient to overcome the discrepancy between the terminal velocity and the flow velocity at the test section. As explained in Chapter 5, it may be possible to provide velocity control by observing the equilibrium position of the droplet. As the droplet evaporates, its position in the test section moves downstream, where the acoustic forces compensate for excessive flow velocity. The wind tunnel velocity can therefore be adjusted based on this deviation in position of the suspended droplet from some desired reference.

6.3 Potential Experiments for the Facilities

There are a broad variety of experiments which could potentially benefit from the capabilities of the Acoustic Levitation Test Facility. For example, hydrometeor evolution experiments, such as ice crystal or snowflake growth, aerosol or trace gas effects, and electrostatic charging effects can be readily conducted in either facility. Single particle phase change behavior including ice nucleation and melting phenomena can be studied in either environmentally controlled facility, depending on the ambient flow conditions desired. Collision experiments can be run in the Ventilated Facility, making use of the droplet injector.

Finally, the study of electromagnetic scattering behavior of hydrometeors is possible. It is clear that the unique capabilities of the facilities, if properly exploited, can provide a useful tool for better understanding dynamic atmospheric processes.

Appendix A
Details of Acoustic Levitator Hardware

Detailed mechanical drawings of the acoustic driver and reflector assemblies are shown in Figures A-1 through A-4. In Fig. A-1, the two titanium resonating sections are shown. When machining these sections, the tolerances should be as small as possible (0.003 in. or less). The remaining components are shown in Fig. A-2. The transmitting plate is made out of aluminum and must be machined to match the resonating frequency of the driver. This is done in an iterative manner, as explained in Section 3.2.3. The assembled driver is shown in Fig A-3.

The reflector assembly is not as constrained as the driver hardware. However, the assembly must be capable of positioning the reflector to an accuracy of 0.5 mm or less. As a result, any backlash in the positioning mechanism should be eliminated. The reflector assembly for the Vertical Facility is shown in Fig. A-4.

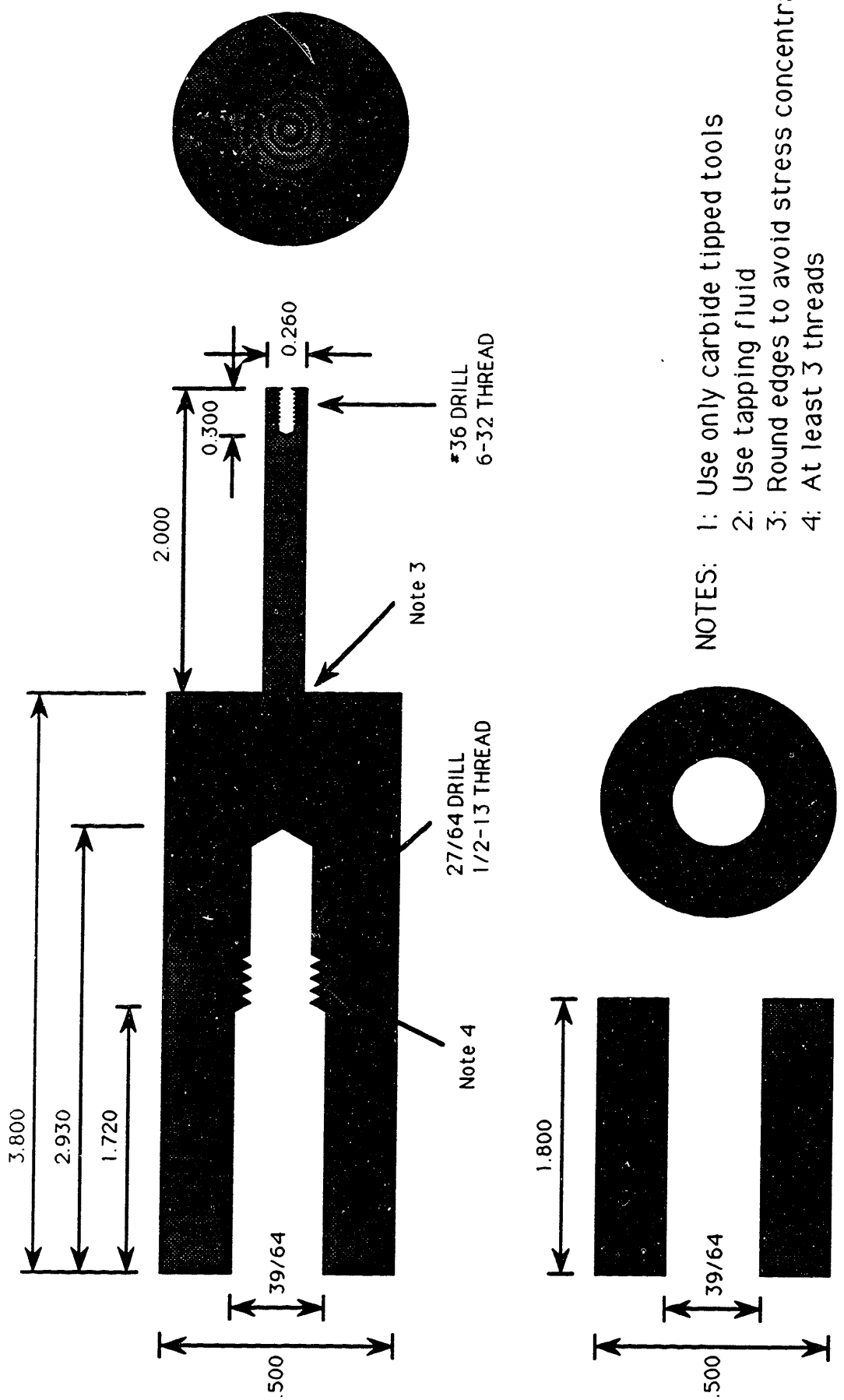

Figure A-1: Detail of the titanium sections of the driver.

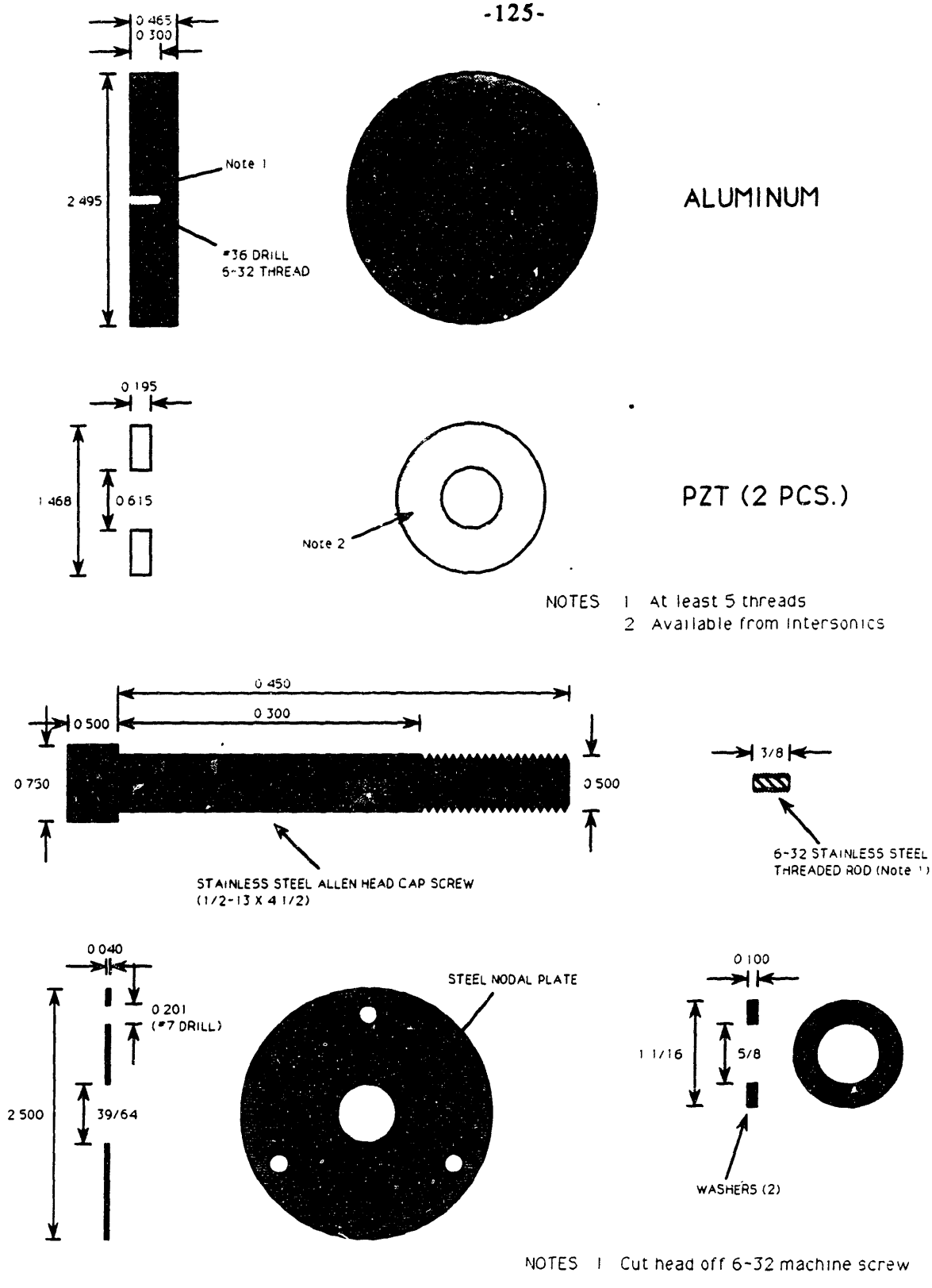

Figure A-2: Detail of the transmitting plate, PZT crystals, and additional components.

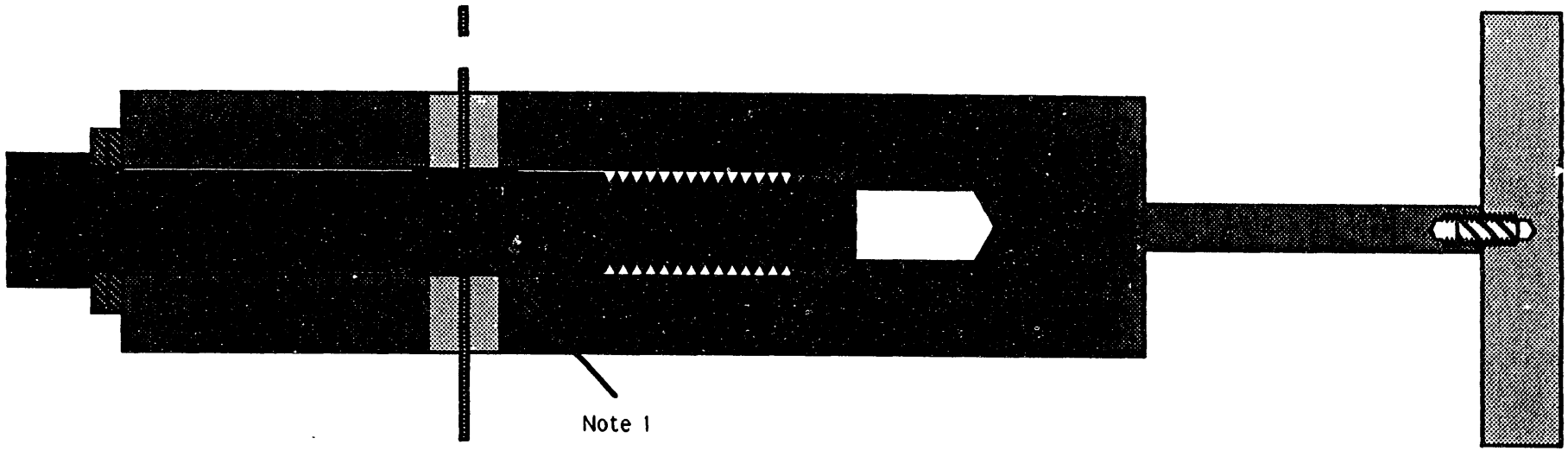

NOTES:
1: Wrap several layers of electrical tape around cap screw to get snug fit with PZT's
2: Positive sides of PZT's must face each other
3: When tightening cap screw, short out nodal plate to titanium
4: Torque down on cap screw to about 50 ft-lbs

Figure A-3: Assembly of the driver elements.

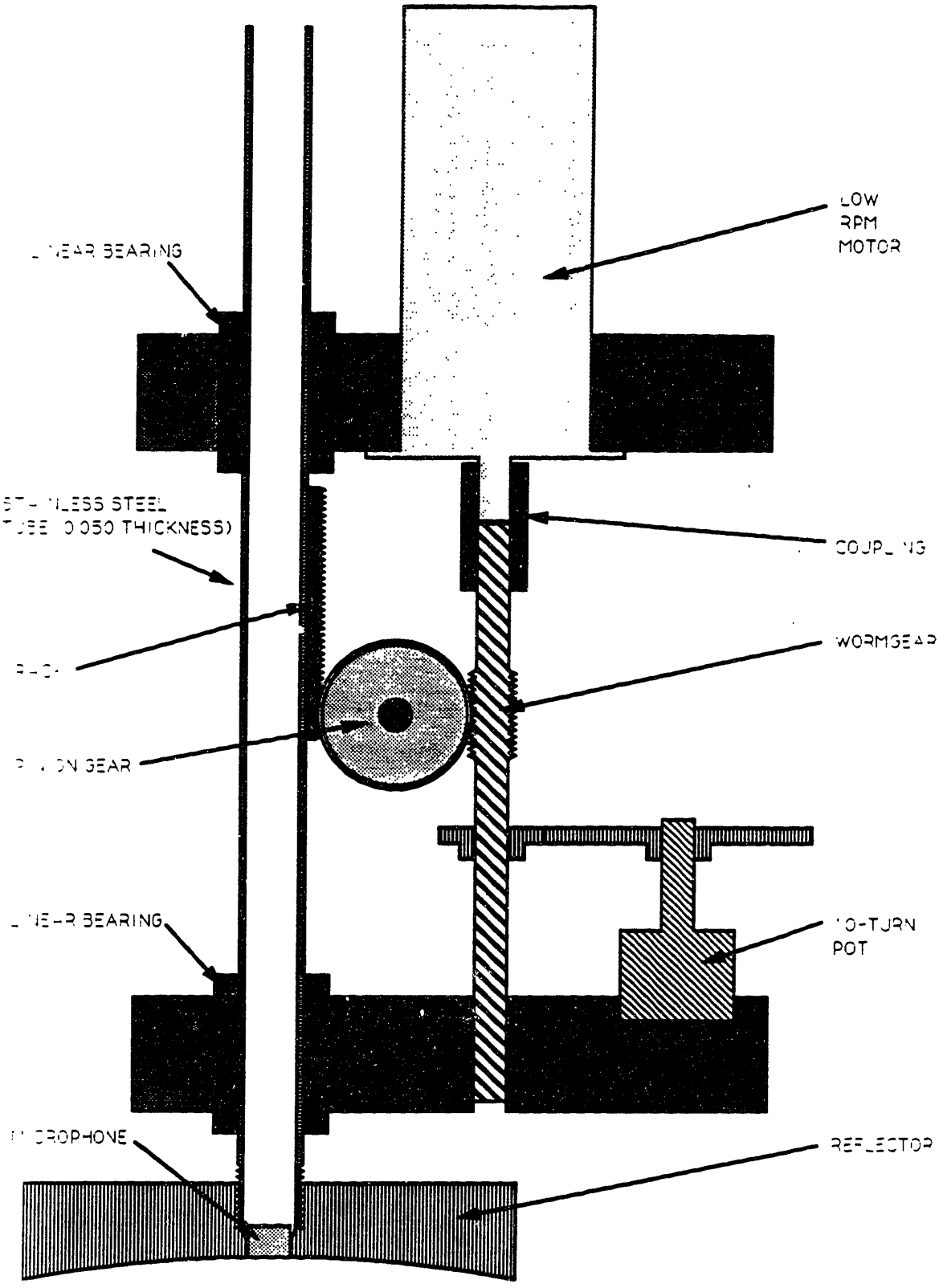

Figure A-4: Detail of the reflector assembly.

Appendix B
Details of Resonance Tracking System

Resonance tracking of the driver is achieved by use of a phase locked loop (PLL) circuit. The PLL compensates for oscillator drift and thermal gradients within the driver simultaneously. This is possible because changes in the excitation frequency with respect to the driver resonance frequency (due to oscillator drift) have the same effect as deviations in the resonance frequency itself (due to thermal effects). The phase locked loop operates by comparing the phase offset between the sinusoidal voltage applied to the driver and the current that flows through it. The two signals are more or less in phase at resonance, and the phase offset can therefore be utilized as the error feedback signal for the controller. The oscillator adjusts its operating frequency based on this signal. The PLL system is shown in Fig B-1.

The signal corresponding to the current through the driver is generated by inserting a small resistor in series with the driver. The voltage across this resistor is then proportional to the current through the driver. In order to avoid excessive power dissipation in the resistor, its value is small (10 ohms) compared to the impedance of the driver at resonance (about 150 ohms).

The phase detector generates a voltage proportional to the phase offset between the sinusoidal driver voltage and current signals, as shown in in Fig. B-2. Phase detection is achieved by first converting the sinusoids into square waves with zero-crossing detection (ZCD) circuitry. The two square waves are then passed through an exclusive-or gate, whose output is a sequence of pulses of equal amplitude. The width of these pulses corresponds to the phase offset of the system. This pulse train is then passed through a low-pass filter, which rejects all but the DC component of the signal (i.e., the average value of the signal over one period). The filter output is then proportional to the system phase offset. The relationship between phase offset and detector output is shown in Fig. B-3. The slope of this relationship represents the sensitivity of the detector. It is important to note that, in the region of zero phase

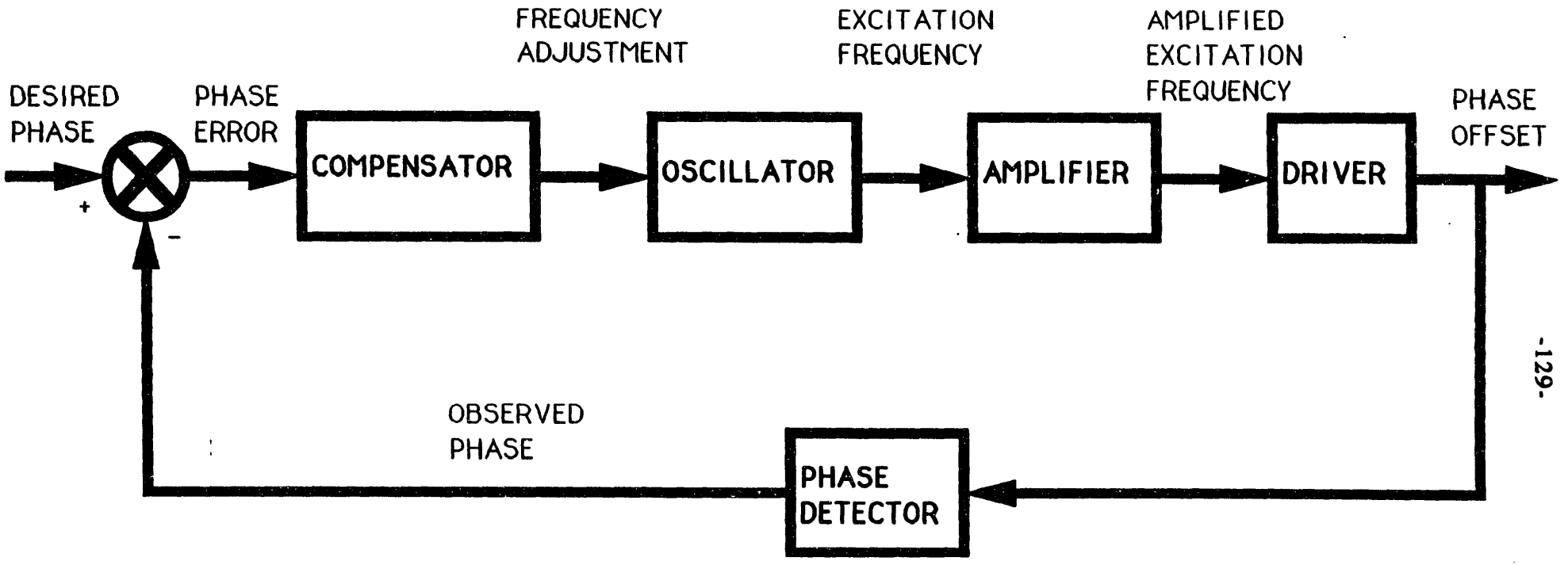

Figure B-1: Block diagram of the driver resonance tracking circuit.

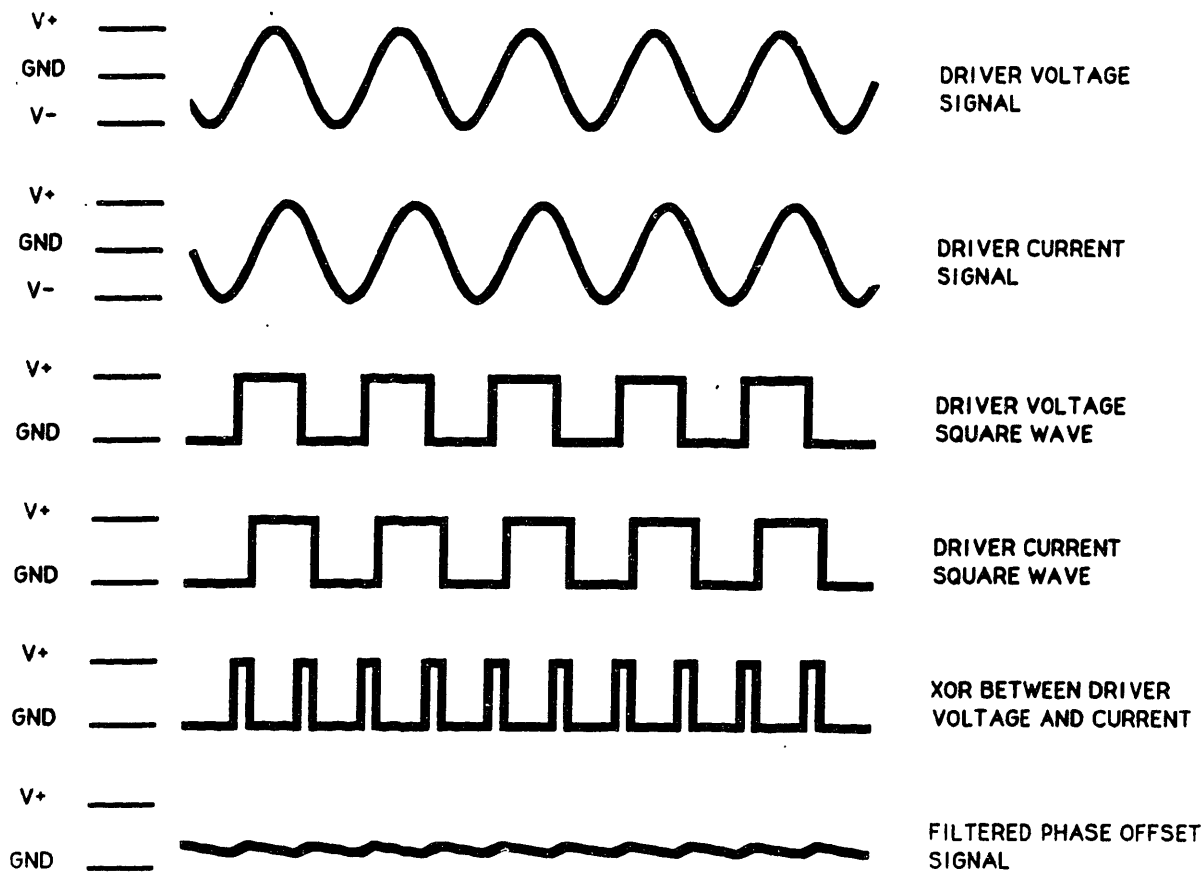

Figure B-2: Relevant signals for the resonance tracking circuit.

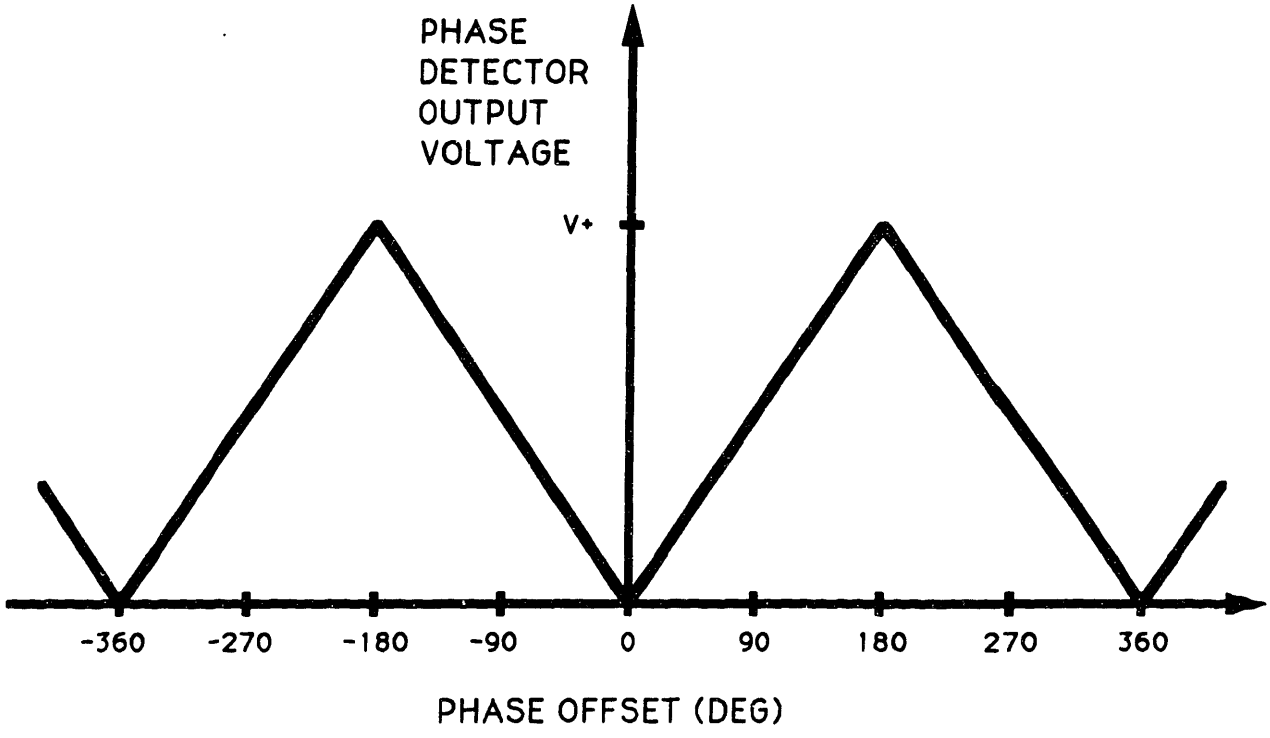

Figure B-3: Response of the phase detector.

offset, the phase detector sensitivity changes sign. This undesirable effect can be avoided by shifting one of the signals from the driver 90 degrees before passing it through the phase detector. With this modification, the operating point of the phase detector shifts to 90 degrees lead or lag (depending on which signal is shifted), far away from the sensitivity reversal.

The compensated system must achieve zero steady state error in order to perform the resonance tracking function. Consequently, the compensator consists of a pure integrator with variable gain.

Appendix C
Details of Refrigeration System

The essential elements of the refrigeration system are shown in Fig. C-1. The system is based on a standard Freon-12 liquid-vapor compression cycle. At the heart of the refrigeration system is a commercial compressor/condenser unit (Tecumsek model #AH2435AC). This unit is equipped with a Freon reservoir and access valves for introducing and discharging refrigerant from the system. The removal of heat from the airstream in the tunnel is achieved by placing two evaporators in the plenum. Each evaporator is connected to a separate expansion valve and solenoid. In this way, either or both of the heat exchangers can be in operation, depending on the cooling rate required for any particular experiment. The thermostatic expansion values have internal mechanical feedback via a temperature bulb mounted to the exits of the heat exchangers. They are calibrated such that the Freon exiting the plenum is slightly superheated. This ensures that the refrigeration system performs at maximum efficiency and prevents liquid Freon from entering the compressor.

The location of the heat exchangers is such that the airstream passing through has low velocity. This increases the rate of heat removal from the flow. The fins of the heat exchangers also play a role in straightening the flow in the plenum. In order to prevent an appreciable temperature gradient between the evaporators and the test section, the region of the tunnel downstream of these elements is heavily insulated.

The status of the refrigeration system is monitored by two pressure gages. The liquid line gage measures the pressure of the Freon fluid before expansion, while the suction line gage measures the pressure of the gas returning to the compressor. Assuming that this gas is a saturated vapor, this suction line pressure corresponds directly to the temperature of the Freon in the heat exchangers. If the gas is slightly superheated at this gage, then the temperature at the exchangers is actually slightly lower. Therefore, the pressure gage provides a conservative estimate of the cooling capability of the refrigeration system.

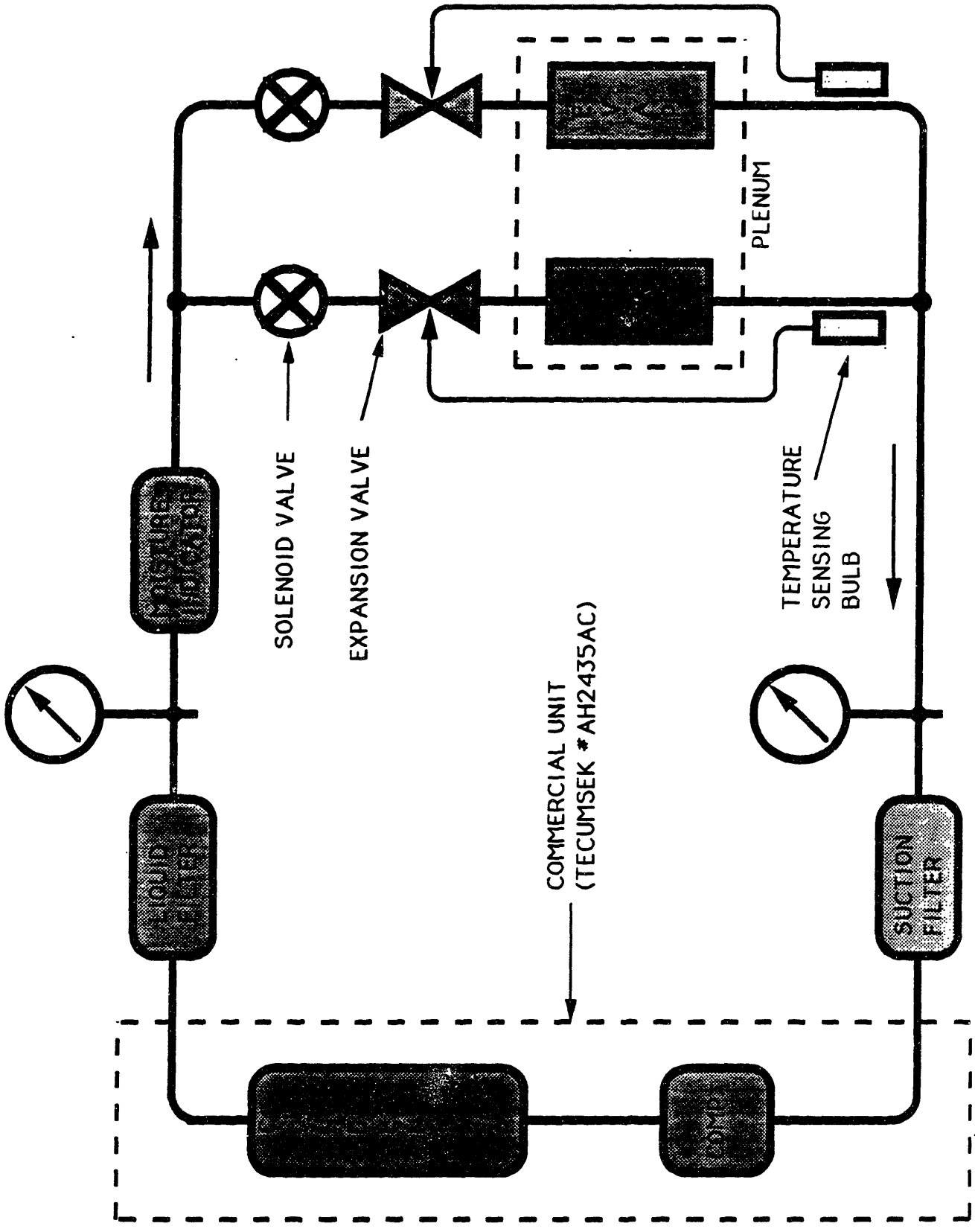

Figure C-1: Diagram of the refrigerator system.

References

[1] King, L.V.
On the Acoustic Radiation Pressure on Spheres
Proc. Roy. Soc., **A147**, 212-240, (1934).

[2] Trinh, E.
Compact Acoustic Levitation Device for Studies in Fluid Mechanics and Materials Science in the Laboratory and Microgravity
Rev. Sci. Instrum., **56**, pp. 2059-2065, (1985).

[3] Wang, T.G., Saffren, M.M., and Elleman, D.D.
Acoustic Chamber for Weightless Positioning
AIAA Paper #74-155, (1974).

[4] Hueter, T.F., and Bolt, R.H.
Sonics: Techniques for the Use of Sound and Ultrasound in Engineering and Science
John Wiley & Sons, Inc., (1955).

[5] Lamb, H.
Hydrodynamics
Cambridge University Press, (1932).

[6] Pruppacher, H.R., and Pitter, R.L.
A Semi-Empirical Determination of the Shape of Cloud and Rain Drops
Journal of the Atmospheric Sciences, **28**, pp. 86-94, 1971.

[7] Imai, I.
On the Velocity of Falling Raindrops
Geophys. Mag. Tokyo, Vol. 21, pp 244-249, (1950).

[8] Landau, L.D., and Lifshitz, E.M.
Fluid Mechanics
Permagon Press, (1959).

[9] Savic, P.
Circulation and Distortion of Liquid Drops Falling Through a Viscous Medium
Report, Natl. Res. Council, Canada, NRC-MT-22, (1953).

[10] Pruppacher, H.R., and Klett, J.D.
Microphysics of Clouds and Precipitation
D. Reidel Publishing Co., (1978).

[11] Seaver, M., Galloway, A., and Manuccia, T.J.
Acoustic Levitation in a Free-Jet Wind Tunnel
Rev. Sci. Instrum., **60**, pp. 3452-3459, (1989).

[12] Ensminger, D.
Ultrasonics: The Low- and High-Intensity Applications
Marcel Dekker, Inc., (1973).

[13] Blevins, R.D.
Formulas for the Natural Frequency and Mode Shape
Van Nostrand Reinhold Co., (1979).

[14] Pruppacher, H.R., and Neiburger, M.
Design and Performance of the UCLA Cloud Tunnel
Proc. Intern. Conf. on Cloud Physics, Toronto, pp. 389-392, (1968).

[15] Abbott, C.E., and Cannon, T.W.
A Droplet Generator with Electronic Control of Size, Production Rate, and Charge
Rev. Sci. Instrum., **43**, pp. 1313-1317, (1972).

[16] Adam, J.R., Cataneo, R., and Semonin, R.G.
The Production of Equal and Unequal Size Droplet Pairs
Rev. Sci. Instrum., **42**, pp. 1847-1849, (1971).

[17] Calliger, R.J., Turnbull, R.J., and Hendricks, C.D.
Hollow Drop Production by Injection of Gas Bubbles into a Liquid Jet
Rev. Sci. Instrum., **48**, pp. 846-851, (1977).

[18] Chung, L., and Cross, W.G.
Production of Single Liquid Drops of Controlled Size and Velocity
Rev. Sci. Instrum., **46**, pp. 263-265, (1975).

[19] Jonsson, H., and Vonnegut, B.
Technique for Producing Uniform Small Droplets by Capillary Waves Excited in a Small Meniscus
Rev. Sci. Instrum., **53**, pp. 1915-1919, (1982).

[20] Raghupathy, B., and Sample, S.B.
A New Apparatus for the Production of Uniform Liquid Drops
Rev. Sci. Instrum., **41**, pp. 645-647, (1970).

[21] Mason, B.J.
The Physics of Clouds
Oxford University Press, (1971).

[22] Green, A.W.
An Approximation for the Shape of Large Raindrops
J. Appl. Meteor., **14**, p. 1578, (1975).

[23] Beard, K.V., and Pruppacher, H.R.
A Determination of the Terminal Velocity and Drag of Small Water Drops by Means of a Wind Tunnel
Journal of the Atmospheric Sciences, **26**, pp. 1066-1072 (1969).